SAPIENZA
UNIVERSITÀ DI ROMA

Faculty of Information Engineering, Statistics and Informatics
Department of Information Engineering, Electronics and Telecommunications

Doctoral program in
Information and Communications Technologies - Applied Electromagnetics
(XXIX Cycle)

Characterization of the physical and structural changes undergone by a biological tissue during microwave thermal ablation procedures

PhD candidate: Dr. Ing. Laura Farina

Supervisor: Prof. Marta Cavagnaro

Motivation

The aim of the present doctoral project was to investigate the physical and structural changes occurring in biological tissue treated with microwave thermal ablation procedures, focusing the study on the evaluation and characterization of the shrinkage of the tissue, in correlation with the influence of the thermal changes.

When the project started in 2013, few studies were conducted to comprehend the shrinking phenomenon (Diaz *et al.,* 2008, Brace *et al.,* 2009, Ganguli *et al.,* 2008, Planché *et al.,* 2013, Brace *et al.,* 2010]. Nevertheless, the subject was of high interest for physicians and scientists involved in this field. The results reported from preliminary studies underlined that the volume occupied by the ablated tissue as measured at the end of the thermal ablation procedure is smaller than the volume occupied by the equivalent untreated tissue. Therefore, it resulted important to be able to adequately characterize the shrinkage of the tissue during a microwave thermal ablation procedure in order to correctly predict the true treatment volume; otherwise, the treatment safety as well as the efficacy can be compromised exposing peripheral structures to unwanted heating and affecting the assessment of the treatment's technical success.

The analysis and study of the thermally ablated tissue led mainly to perform extensive experimental investigations. Accordingly, *ex vivo* studies were conducted at four different laboratories:

- the Laboratory of the Division of Health Protection Technologies, ENEA Casaccia Research Centre, Rome (Italy);

- the Radiology Dept. of Regina Elena National Cancer Institute, Rome (Italy);
- the R&D laboratory of HS Hospital Service SpA, Aprilia (Italy);
- the Applied Radiology Laboratory of Hadassah Hebrew University Medical Center, Jerusalem (Israel), where I stayed for 6 months as visiting scholar.

Moreover, thanks to the COST support, the laboratory of the Institute of Microbiology of the Academy of Sciences, Prague (Czech Republic), hosted me during a Short Term Scientific Mission (STSM) to conduct *in vivo* experiments of dielectric spectroscopy in the framework of a newborn joint scientific collaboration.

In the following chapters, the conducted work is illustrated following the speculative project development. Specifically, this chapter introduces the microwave ablation therapy, its operating principles, clinical and experimental applications and gaps; the second chapter concerns the used devices and the setups developed to conduct the experimental trials; and the third chapter illustrates the conducted experiments and their results. Finally, the outcomes are discussed in the conclusive chapter.

1 Introduction

Microwave thermal ablation is a minimally-invasive thermal ablation therapy used to treat a variety of tumors in different organs (Habash *et al.,* 2007).

Thermal ablation therapies use the interaction between a physical energy (e.g. radiofrequency and microwaves) and the tissue to heat the target cells up to irreversible injury. Irreversible cellular damage is obtained increasing the tissue temperature to 46 °C for 60 min; or to 50–52 °C for 4–6 min. Thermal ablation is achieved when the temperature of the tissue reaches at least 55–60 °C: at these temperatures, an almost instantaneous coagulation occurs (Ryan *et al*., 2010, Ahmed *et al*., 2011), whereas above 100 °C the tissue carbonizes (Lopresto *et al*., 2014). Ablative technologies are widely tested and used in interventional radiology, in particular in the treatment of tumorous diseases where they are already used with success. Previously published clinical data demonstrated their safety and early efficacy in the treatment of solid tumors (Yu *et al*., 2012, Liang *et al.,* 2005, Vogl *et al*., 2011, Swan *et al*., 2013). Thermal ablation therapies are proposed as alternatives to traditional surgery, radiotherapy and chemotherapy, allowing the treatment of non-surgical patients with satisfactory results. They have the potential to improve upon current therapies.

Several imaging techniques, including computed tomography (CT), ultrasound (US), magnetic resonance (MR) imaging and, more recently, positron emission tomography (PET)-CT are adopted to support the thermal ablation procedures (Ahmed *et al*., 2014), with a propensity for CT. Image guidance is currently used for planning, targeting, real time monitoring of ablation therapy, as well as for assessing treatment response. Planning involves tumor location and delineation in terms of number, size and shape, together with visualization of the surrounding anatomy (Goldberg *et al*., 2005). Then, the imaging devices play an important role during the targeting, guiding the operator in the proper placement of the antenna applicator into the tumor tissue. Some of the abovementioned technique can also help monitoring the procedure and the therapy effects. Finally, an important imaging application concerns the follow-up monitoring: immediate assessment at the end of the MTA procedure, that should demonstrate that the target end point has been reached, and the patient supervision in the months, or years, following the treatment (Goldberg *et al*., 2005).

Among the imaging devices, CT seems to be the most suitable one for the guidance and the supervision of a tumor-ablation procedure: indeed, if carefully analyzed, it allows to discriminate the rim of the treated lesion and detect complications (Mitsuzaki *et al*., 1998, Goldberg *et al.,* 1998, Raman *et al*., 2000).

Thus, when thermal ablation systems are used with appropriate imaging modalities, it is possible to accurately plan and control the tumor ablation operation; nevertheless, the ultimate treatment planning is still left to the experience of the physician and to his knowledge of the apparatus in use (Hinshaw *et al*., 2014). Indeed, microwave ablation techniques require further study and investigation to improve the control of the clinical procedures. There is still need to improve the understanding of the relationship between the treatment outcome and the physical and biological variables present in clinical applications in order to achieve reproducible and predictable results (Cavagnaro *et al*., 2015a). The electromagnetic, thermal, and mechanical properties of tissues need to be characterized at the temperatures achieved during microwave ablation, which often exceed 100 °C (Yang *et al*., 2007, Brace *et al.,* 2009, Lopresto *et al*., 2012, Lopresto *et al.,* 2014, Ji & Brace 2011, Farina *et al* 2014d). Well-understanding the behavior of the biological tissue during a heat treatment is an important factor to reach an accurate ablation prediction and control the ablated volume. In particular, the tissue shrinkage represents a challenging issue, affecting the ability to predict the size and shape of the induced thermal lesion, and still need to be fully addressed.

Accordingly, the present work not only propose to give a qualitatively and quantitatively characterization of the shrinkage phenomenon, but also to build an analytical model usable from the physician to correctly estimate the amount of tissue contraction occurred in the target tissue and thus enhance the treatment assessment.

1.1 Microwave Thermal Ablation

Microwave thermal ablation (MTA) exploits the absorption of an electromagnetic field radiated by a microwave (MiW) antenna to induce a very high and localized temperature increase in the target lesion and destroy pathologic tissues, such as tumors (Brace *et al.,* 2009, Lin *et al*., 2014, Liang *et al*., 2015, Smith *et al*., 2015). MTA devices are typically operated at either 915

MHz or 2.45 GHz. The heating is the result of the relaxation mechanisms, i.e. the rotation of the molecules with an intrinsic dipole moment forced to realign with the applied field: the vibration of the molecules causes an increase in kinetic energy and an increase of the local tissue temperature. Thus, it is a dielectric heating: the electromagnetic field propagates independently of the tissue electrical conductivity, through all the biological materials also in the dehydrated ones (Ahmed *et al*., 2011), and allows treating lesions up to a diameter of 50 mm (Hines-Peralta *et al*., 2006, Hoffmann *et al*., 2013).

Great accuracy in the delivery of the microwave field is required to control the ablated volume. The heat deposition is greatest close to the antenna and decreases farer from it. Accordingly, in the MiW ablated volume, at least two different regions can be identified (Ahmed *et al*., 2014). A "carbonized" region is definable close to the antenna axis, where the temperature rises above 100 °C and the tissue appears charred, highly desiccated, and black. A more peripheral region of complete thermal denaturation of proteins known as "white coagulation", in which the temperature rises above approximately 60°C but without exceeding 100°C, surrounds the previous one (Lopresto *et al*., 2014). The shape of the thermally ablated volume is most often a rotational ellipsoid, with the longest axis along the applicator shaft, and a transverse diameter depending on the exposure power and duration (Hines-Peralta *et al*., 2006, Hoffmann *et al*., 2013).

MTA clinical setups usually include a MiW power generator, an interstitial antenna applicator, and a cooling system. The clinical practice consists in positioning the antenna applicator in the center of the tumor to be treated, usually through image-guided procedures, and in supplying it with a certain MiW power for the time of choice. Over the last decade, there has been increasing diffusion of MTA devices into clinical practice, designed for image-guided percutaneous insertion into the target. Such systems make use of a needle-shaped microwave applicator featuring a coaxial antenna at its distal end. All the commercial devices provide tables and literatures references, recommending the most suitable power-time protocol to obtain the desired dimension of the thermally ablated zone in the different organs, based on *ex vivo* and/or *in vivo* evaluations.

1.2 Tissue shrinkage

Studies describing tissue shrinkage during thermal ablation have been recently published (Ganguli *et al*., 2008, Planché *et al.,* 2013, Rossmann *et al*., 2014, Brace *et al*., 2010, Brace *et al*., 2011, Liu & Brace 2014, Sommer *et al*., 2013). The shrinkage of the tissue means that the dimensions of the ablated tissue evaluated immediately after the procedure, e.g. by way of CT images, underestimate the actual treated tissue. Such an underestimation, not taken into account in the abovementioned tables provided by the companies, could lead to inaccurate conclusions about the achievement of the goal of the procedure, and in a worst-case scenario could motivate an unnecessary second-treatment. For this reason, it is very important to evaluate tissue shrinkage correctly and quantitatively in the different clinical conditions.

At the beginning of this study, three-years ago, some experiments investigating the amount of tissue contraction during radiofrequency (RF) and microwave ablation with the help of imaging systems were available in literature. Ganguli et al. (2008) reported an average shrinkage of *in vivo* renal tumors treated through RF ablation of 21%, and Planché et al (2013) a 17.7 ± 3.4% reduction of *in vivo* swine lung tumor mimics during MTA. Besides these *in vivo* observations, the first study devoted to the shrinkage was conducted in *ex vivo* bovine liver and lung, considering both radiofrequency and microwave ablations (Brace *et al*., 2010). Markers were placed into the pieces of tissue were placed markers at three different distances from the applicator. The markers were 1.5 mm diameter polytetrafluoroethylene tubes oriented parallel to the applicator along a plane bisecting the ablation applicator. After the thermal procedure, the lesion was cut and the post-ablation position of the markers was examined, and absolute and relative contraction were calculated, pointing out a positive correlation between shrinkage and water loss. A shrinkage in the range of 30-50 % of the initial volume was observed grater in liver treated with microwaves than with radiofrequency. In particular, the contraction along the direction orthogonal to the active device was about 30% for MiW ablation, and about 15% for RF: it is worth noting here that MiW provokes higher temperatures in the tissue with respect to RF. Subsequently, the CT scan was used to monitor the tissue contraction over time during a microwave ablation procedure conducted at 2.45 GHz on an *ex vivo* bovine liver. The markers involved in this experiment were high-density wires placed parallel to the antenna. The distances were measured automatically before, during

and after the ablation to evaluate the contraction. A most significant contraction was observed in the first minutes of heating and near the antenna. In some samples, expansion was also noted between some adjacent markers (Brace *et al*., 2009). Liu & Brace (2013) observed an irreversible process of shrinkage depending on time and on the distance from the center of the ablated zone. Experiments were conducted under CT control on *ex vivo* bovine liver to analyze spatial and temporal tissue contraction during a microwave ablation, using a grid of fiducial markers. An irreversible shrinkage process was confirmed observing a greatest relative contraction at the center of ablation zone and the total contraction decay over time. The greatest effect was noted in the first 4-5 minutes of heating.

In the last three years, tissue shrinkage has been addressed by different research groups, through multiple systematic *ex vivo* studies with the aim to better characterize it. In particular, correlations between the shrinkage and the deployed energy (Sommer *et al*., 2013), and between the shrinkage and the temperature increase (Rossmann *et al*., 2014) were found. Rossmann et al. (2014) measured the shrinkage of *ex vivo* liver kept at a constant temperature in the range between 60 °C and 95 °C for up to 15 min. The relative shrinkage increased with increasing temperature and/or time of exposure, and it was modeled through a linear regression analysis as a function of the exposure time (Rossmann *et al*., 2014). The highest relative shrinkage found was about 22%, measured at 95 °C after 15 minutes of exposure, while it was close to 12% for temperatures close to 60 °C, in accordance with Ganguli et al. (2008). Compatible results were obtained from Sommer et al. (2013) in the kidney: moreover, it was confirmed that the higher the deployed energy, the higher the measured contraction; with the most significant contraction occurring in the first 2 minutes of heating. In agreement with the previous results, it has been demonstrated that the relative shrinkage induced by RF or MiW percutaneous applicators is higher for tissues close to the energy source and is higher for MTA with respect to RF ablation (Rossmann *et al*., 2014).

1.3 Tissue dielectric properties

The advances in theranostic technologies based on the interaction of electromagnetic fields with biological tissues led to the development of dielectric spectroscopy, with particular attention to the living biological tissue (Vannucci *et al.,* 2016). Up to now, some gaps of knowledge are

present in the characterization of dielectric behavior of tissues and tumors (Cho *et al*., 2006, O'Rourke *et al*., 2007, Halter *et al*., 2009, Lopresto *et al*., 2012, Peyman *et al.,* 2015), especially regarding *in vivo* measurements. As an example, while in Peymann et al. (2015) no significant differences were found between *ex vivo* and *in vivo* data, as could be expected in the MiW range (Foster *et al*., 1981), in O'Rourke et al. (2007) higher values were measured *in vivo* with respect to the *ex vivo* condition. These gaps of knowledge need to be investigated further in order to clarify if the great body of *ex vivo* measurements can be considered representative of the *in vivo* case or not.

It is important to underline that the knowledge of tissue's dielectric and thermal properties is fundamental for the development of realistic models of organ- or tissue-specific pathologies; models that could be used in treatment planning simulations of MTA procedures to allow improvement of MiW applications. Indeed, while *in vivo* measurements in human patients, to preliminarily set systems and technical approaches, find ethical limitations, especially if directed to measure pathologic tissue in sick individuals, the same measurements performed in experimental animals may be considered acceptable for pre-clinical research purposes, if conducted under duly justified circumstances. In experimental animals, a bulk of tissue useful for measurements can be obtained by producing controlled tumours, generated by a subcutaneous inoculation of cancer cells in immunodeficient animals able to not reject them (e.g. athymic mice, athymic rats and various knock-out animals). However, aside these consolidated techniques, new approaches can produce transpositions of one or more tissues inside a subcutaneous pocket, to obtain the necessary volume of biological structures useful for correct measurements and, more important, with general characteristics as close as possible to the organ/tissue to be studied.

2 Materials and Methods

2.1 Introduction

To investigate the shrinkage phenomenon occurring in the biological tissue treated with a MTA procedure, several experimental studies were carried out developing dedicated setups. Numerical elaborations were performed to analyze the experimental data and to electromagnetically test the proposed setups.

In numerical studies, the knowledge of the dielectric properties of tissue is fundamental. Accordingly, some experiments were conducted to develop and test a portable measurement setup for broadband dielectric characterization of biological tissue samples. The setup was then used to perform measurements on an *in vivo* breast model.

All setups, which will be presented in the following paragraphs, are the result of an optimization process done with the aim of conducting measurements as simple, reliable and repeatable as possible.

In this chapter, an overview of the different devices and tools is given as well as a description of the different experimental setups and numerical analysis carried on.

2.2 Devices, sensors and softwares used

The MTA devices used in the different setups, the sensors adopted to measure different electromagnetic and thermal quantities, as well as the numerical tools exploited to simulate, manage and elaborate the data are presented below.

2.2.1 Thermal Ablation Systems

MTA systems usually include a MiW power generator, interstitial antenna applicators and a cooling system. The three commercial apparatuses for microwave ablation operating at 2.45 GHz reported in Figure 2.2.1 were used: Acculis^{TM} MTA System AngioDynamics, Amica^{TM} system HS Hospital Service SpA, and Emprint^{TM} Covidien, indicated as MS, HS and CV in the following for sake of brevity.

Figure 2.2.1 Commercial systems for Microwave Thermal Ablation: Acculis™ MTA System AngioDynamics, Amica™ system HS Hospital Service SpA, and Emprint™ Covidien (from left to right).

Acculis™ MTA 2.45 GHz system (MS) uses a generator able to supply up to 140 W at one or two applicators. Un-cooled antennas are proposed for open or laparoscopic insertion, and water-cooled antennas for percutaneous insertion; an internal temperature monitoring system is provided. Moreover, the system monitors the net power supplied by the generator, but the power that effectively reaches the input port of the antenna is about 50% lower, due to the losses of the coaxial cable connecting the generator to the antenna (http://www.angiodynamics.com/products/Acculis).

Amica™ is a hybrid system (HS) consisting of a programmable RF and MiW generator (HS Amica GEN H 1.0): as RF system, it is able to supply up to 200 W at 450 kHz, and as MiW system, up to 140 W at 2.45 GHz. RF applicators are 17- and 18-gauge probes with an exposed tip varying between 5 and 35 mm depending on the purpose of use (interstitial or laparoscopic procedures); whereas MiW applicators are 11-, 14- and 16- gauge antennas with an active tip of 30 mm, water-cooled via a fully automated peristaltic pump. The temperature at the antenna handle as well as the energy supplied are constantly monitored; both forward and reflected powers are continuously measured and displayed; the losses of the connecting cable are taken into account so that in this system the set power is the power effectively delivered to the antenna (http://www.hshospitalservice.com).

Emprint™ 2.45 GHz system (CV) comprises a generator able to supply up to 100 W, and 13-gauge antennas made of a flexible fiberglass body water-cooled till the active tip of the applicator. As for the Acculis system, the coaxial cable connecting the generator to the antenna lowers the power effectively radiated into the tissue of about 40 – 50%. Electromagnetic field, tissue temperature, and wavelength are continuously monitored and adapted to optimize the energy distribution into the tissue, provide a more spherical shape of the ablated region, and reduce tissue charring (http://www.medtronic.com/covidien/products/ablation-systems/emprint-ablation-system, Ierardi *et al.,* 2015).

The MTA systems used adopt different antenna designs as shown in Figure 2.2.2. The main technological difference is in the cooling system: it arrives up to the choke section in the Amica and Acculis applicators (about 20 mm behind the antenna tip); while in the Emprint applicator, it is allowed to cool the entire antenna up to its tip. For the experiments conducted with the Acculis™ MTA System, internally cooled MiW antennas for percutaneous applications with a diameter of 1.8 mm (approximately 15-gauge) were used (Accu2i pMTA Applicator); internally cooled 14-gauge MiW ablation antennas (HS Amica probe 14 G) and straight internally cooled RF applicator with 30 mm exposed tip length (RF Amica probe 17 G) were adopted for the ablations performed with the Amica™ system; and 13-gauge water-cooled MiW antenna were chosen for the Emprint™ system.

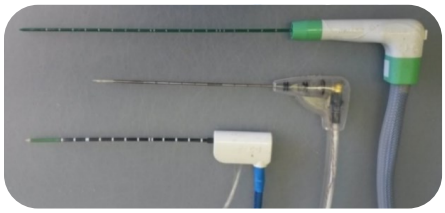

Figure 2.2.2 Commercial antennas for Microwave Thermal Ablation: 14 G HS Amica probe, 15 G Accu2i pMTA Applicator, and 13 G Emprint percutaneous antenna (from top to bottom).

2.2.2 Computed Tomography (CT)

The computed tomography scanner Brilliance iCT System, Philips Medical System technologies (www.nice.org.uk/dg3), was used as sensor to detect the modifications occurring in the thermally ablated tissue (Figure 2.2.3).

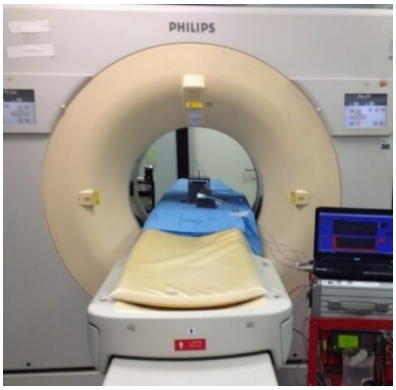

Figure 2.2.3 Computed tomography scanner: Brilliance iCT System, Philips Medical System technologies.

The CT system produces tomographic images of sections of the human body, using computer-processed X-ray, from which it is possible to generate a three-dimensional image used for diagnostic purposes. The CT system is composed of a gantry, a bed, a X-ray source (conventionally, the X-ray tube), X-ray sensors (detectors), services such as transformers, cable and connection, data transmission system, slip rings, data processors. The CT output is expressed by the Hounsfield Unit (HU) number, which is function of the absorption coefficient of the tissue and represents the relation between the intensity of the incident radiation and the intensity of the radiation reaching the sensors once attenuated by the tissue, normalized to the water absorption coefficient. A computer calculates tissue absorption, produces a representation of the tissues and creates the image, showing the densities of the various structures: tumor masses, bones, accumulations of fluid, etc. The CT images are recorded as DICOM (Digital Imaging and Communications in Medicine) format. DICOM is the international standard for medical images and related information (ISO 12052), and it is implemented in almost every radiology, cardiology imaging, and radiotherapy device (X-ray, CT, MRI, ultrasound, etc.) (http://dicom.nema.org/).

2.2.3 Temperature measurements

To monitor the tissue temperature, a four-channel fiber-optic thermometer (Fotemp FTC-0038, Optocon AG, Dresden, Germany), with a measuring range from -200°C to +300°C and a measurement accuracy ± 0.5 °C, was adopted. Fiber optic sensors measure the decay time of their emitted light that is a persistent property of the sensor and varies precisely with temperature. The sensors are completely non-conductive, made out of Teflon with a gallium arsenide tip, resistant to chemical agents and corrosion; therefore they results suitable to be placed close to a radiating source (e.g. the MiW antenna) in the biological tissue.

To perform temperature checks on liquids or samples under test, a hand-held thermocouple (RS Pro RS52, K-Type probes, RS Components Ltd., Corby, UK) was also used. Thermocouples are electrical devices exploiting the Seebeck effect to supply temperature measurements: they consist of two conductors (chromel-alumel in the K-type) in which an electric current flows, forming an electrical junction. Since the temperature differently influences the conductors' resistivity, the voltage generated at the junction is a function of the temperature experienced by the junction. Therefore, in presence of an electromagnetic field, thermocouple sensor

measurements can be influenced from induced currents or voltages in the thermometric circuit and the temperature readings can result unreliable (Smalcerz A. *et al*., 2013).

2.2.4 Power measurements

To monitor the forward and reflected power values, the MiW generator was connected through a directional coupler (Narda 3022) to a dual channel power meter (Agilent E4419B, Agilent Technologies Inc.) equipped with two power-sensing probes (Agilent 8481H, Agilent Technologies Inc.). The Narda 3022 directional coupler has a frequency range of 1.0 GHz – 4.0 GHz. The adopted power meter allows two simultaneous power readings (User's guide, Agilent E4418B), and has an operating frequency range of 100 kHz – 110 GHz and a power range between -70 dBm and +44 dBm (100 pW – 25 W); while the probes have a frequency range of 10 MHz – 18 GHz and a power range between -10 dBm and +35 dBm (100 μW – 3 W). The power meter displays absolute or relative values depending on the set option.

Both the power meter and the power sensor probes were calibrated before their use: for the power meter, calibration is done applying a stable reference signal at 50 MHz with an amplitude of 1 mW and comparing the obtained signal to the reference one, thus correcting errors in case of mismatch. The power sensor probes need to be calibrated at the desired working frequency (e.g. 2.45 GHz) through the power meter.

2.2.5 Dielectric properties measurements

To conduct broadband measurement of dielectric properties of tissues a well-known commercial vector network analyzer (E5071C ENA VNA, Keysight Technologies), and a hand-held spectrum analyzer (FSH8, Rhode & Schwarz, Munich, Germany, operating frequency band 300 kHz – 8 GHz) were used. The VNA equipped with a proprietary measurement software and displaying a measurement uncertainty of 5%, was used as "golden standard". The spectrum analyzer equipped with a tracking generator to operate as a vector network analyzer (VNA) was proposed to be adopted in a portable setup suitable for *in vivo* measurements of tissue dielectric properties. Both devices were connected to an open-ended coaxial probe (85070E slim-form Dielectric Probe Kit, Keysight Technologies, Santa Clara, CA), through a low-phase variation coaxial cable. Inserting the probe tip into the material under test that can be liquid or semi-solid,

it was possible to measure the probe reflection coefficient (S11) by the VNA in the frequency band of interest.

2.2.6 Software

Three different software were used: LabVIEW, and more extensively MATLAB and CST Microwave Studio. The LabVIEW software was used to manage both the spectroscopy measurements and the MTA sessions, remotely controlling and synchronizing the data acquisition in the first case and the MiW generator and the temperature sensors in the second case, and automatically storing data.

Dedicated programs were developed with the commercial programming software MATLAB to collect, organize and elaborate data (e.g. DICOM images). MATLAB is a numerical computing environment using a dedicated programming language that allows performing computational tasks in various fields. MATLAB implements a dedicated tool for DICOM images reading and elaborations. Thanks to this tool, a routine was purposely developed to analyze the CT scans outcomes and elaborate the data of interest, approaching the images as matrixes of pixels. MATLAB was also used to develop a program for the evaluation of the dielectric properties from the collected S11 data.

The CST Microwave Studio commercial software for 3D simulation of the electromagnetic fields in the microwave range of frequencies was used to model and test antennas and their performances in different environments (e.g. biological tissue). CST Microwave Studio provides a design environment with a material library and different options to define boundary and background conditions; different solvers are available. In this work, the transient domain solver was used to numerically evaluate the electromagnetic field radiated by an antenna placed into a biological tissue simulating different sizes and shapes of the samples. The transient domain solver uses the Finite Integration Technique (FIT), a spatial discretization method solving the Maxwell's equations in their integral form. Thanks to the use of independent volumetric cells (voxels) it is possible to analyze structures with arbitrary shapes and made of different materials: the dielectric material properties (together with other properties, such as thermal, physical, and mechanical) are definable for each voxel.

2.3 Setups developed for *ex vivo* experimental studies

Several experimental setups have been optimized and used in order to analyze the behavior of *ex vivo* tissue during a microwave ablation procedure (Farina & Cavagnaro 2016). The setups presented below involve organic non-homogeneous tissues: *ex vivo* bovine and/or porcine liver tissue and *ex vivo* turkey muscle. The *ex vivo* tissue was obtained in large blocks of tissue (up to 10 kg for bovine liver) from a local slaughterhouse and stored in freezer at – 20÷40 °C. The day prior the experiments, the *ex vivo* tissue was taken off the freezer and allowed to defrost. The day of the experiments, samples were cut from the larger blocks in different sizes, from small cubes of 10 mm side to bigger specimens, as required for the specific trial. Before each experiment, the instrumentation was set and calibrated, and the initial temperature of the tissue measured: the range of acceptable values was settled from 18 °C to 24 °C. After the heating procedure, specimens were sectioned along the antenna axis to evaluate the extension of the induced carbonized and coagulated area. In restricted samples, tissue dimensions were measured before and after the ablation procedure with a ruler with an accuracy of 1 mm; then, linear and volumetric shrinkage were calculated comparing the pre- and post-treatment measurements.

In the following paragraphs, the different setups are depicted.

In section *2.3.1*, an experimental setup for the direct and precise determination of the pre- and post-ablation dimensions of small specimens is presented. The proposed setup allows the MiW ablation of tissue samples smaller or comparable with the induced thermally ablated volume, thus allowing the direct investigation of the evolution of the thermally ablated area and of the tissue shrinkage at increasing distances from the antenna axis.

In section *2.3.2*, an experimental setup for MiW ablation trials on unrestricted (bulk) tissue samples is depicted. The setup allowed to validate the experiments conducted on the restricted tissue samples and asses their limits, comparing the dimensions obtained for the carbonized areas and for the coagulated areas.

In section *2.3.3*, an experimental setup for the exclusive analysis of the shrinkage occurring in the carbonized tissue using a commercial MiW oven is proposed. The setup allowed inducing tissue samples to complete carbonization and evaluating the effect of increasing thermal doses.

In section *2.3.4*, an experimental setup for the exclusive analysis of the shrinkage occurring in the coagulated tissue using a commercial RF ablation system is proposed. The setup allowed inducing tissue samples to complete coagulation avoiding carbonization and evaluating the average shrinkage in the only coagulate area.

In section *2.3.5*, an experimental setup for real-time analysis based on the use of a CT scan is reported. The setup allowed locally analyzing the tissue shrinkage over the time of ablation by fiducial markers' tracking, and evaluating the temperature increase in the treated tissue thanks to fiber-optic sensors.

In section *2.3.6*, an experimental setup for MiW ablation trials on thin samples of tissue is illustrated. The setup allowed evaluating the influence of the samples dimensions on the spatial evolution of the induced thermally ablated area, in terms of size and shape.

2.3.1 MiW ablation on restricted samples of tissue

Ex vivo bovine liver was cut in cubic samples of 10, 15, 20, 30 and 40 mm ±2 mm side. The MTA applicator was inserted into the center of the cuboid sample in order to have the radiating part of the antenna surrounded by the tissue. Then, the cube of tissue was inserted into an agar phantom (9%) to maintain electromagnetic and thermal continuity at the tissue boundaries (Figure 2.3.1). The dielectric phantom was prepared on a combined hot-plate magnetic stirrer device, mixing distilled water (400 mL), agar powder (36 g, i.e. 9% of the water weight), sucrose (1.5 g), and sodium chloride (1.5 g). The chosen agar concentration gave the most suitable density to maintain the position of the cube of tissue during the whole ablation procedure. Sodium chloride was added to ensure an electrical conductivity (σ = 2.2 S/m @ 2.45 GHz) approximating that of liver tissue (σ = 1.8 S/m @ 2.45 GHz), with the sucrose aiding solidification. A glass beaker (500 mL, inner diameter 10 cm) was used to contain the phantom and a hole was precisely cut centrally in the simulator to insert the sample of tissue; then the sample was covered with additional agar diluted in saline solution (Farina *et al*., 2014).

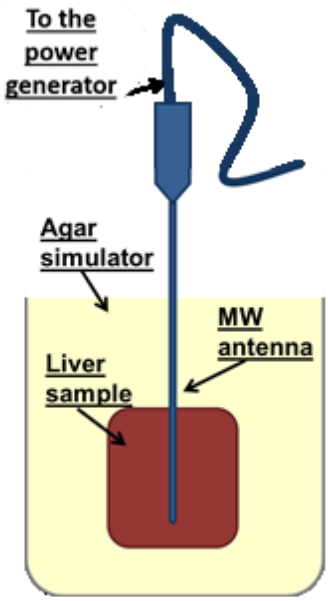

Figure 2.3.1 Schematic of the experimental setup for MTA on restricted samples of biological tissue.

Experiments (N = 220) were performed in order to evaluate the tissue shrinkage as function of the increasing distance from the antenna axis, and as function of the increasing time of ablation, with three different commercially available devices. Cube shaped tissue samples of 10, 20, 30 and 40 mm side were ablated with the Amica device (N = 118); then, 15, 20, 30, and 40 mm side cubes were treated with the Acculis system (N = 60), and on 20, 30 and 40 mm side cubes with the Emprint system (N = 42). In the experiments conducted with the Acculis device, the 15 mm side cubes replaced the 10 mm side cubes for easiness of cutting and positioning once verified the compliance of the results in the two cases. Whereas, due to the bigger diameter of the Emprint antenna and to its scarce adhesion to the tissue it was not possible perform reliably experiments cubes smaller than 20 mm side. In all the experiments, the MiW power was set at the generator in order to have an average power of 50-60 W supplied to the antenna. In particular, the Amica system was set to operate at 60 W, the Acculis system at about 120 W, and the Emprint system at 100 W (maximum output power available). The MTA procedure was performed for 1, 2.5, 5, 7.5, and 10 min. Distilled water at 10–16 °C was used to cool the applicators.

Further experiments were performed to evaluate the tissue shrinkage at the precise edge of the thermally ablated area, using the Amica system and cuboid specimens (N = 6) of a square base of

56 ± 4 mm side and a height of 65 ± 2 mm, at a fixed power of 60 W with an ablation duration of 10 minutes. In fact, preliminary experiments showed that, with the chosen power and time settings, the ablated zone extends about 53 mm along the applicator axis and 43 mm in the direction orthogonal to the applicator axis, and thus the chosen samples' size fit for including the whole achievable ablated zone. Table 2.3.1 shows the different experiments conducted reporting the set combinations of MiW power and time of irradiation, samples sizes and numbers of repetitions performed for each case.

2.3.2 MiW ablation on unrestricted samples of tissue

Unrestricted specimens of *ex vivo* liver tissue (bulk) were treated with the Amica system (N = 18), applying 60 W for the above proposed time intervals 1 min, 2.5 min, 5 min, 7.5 min and 10 min, i.e. under the same operating conditions of the experiments conducted on the restricted samples (*2.3.1 MiW ablation on restricted samples of tissue*). As cited above, the "bulk" experiments were conducted to identify the limits due to the shape and the dimension of the samples used in the "small-samples" experimental setup.

Table 2.3.1 List of the MTA cube experiments conducted.

Device	***Set Power [W]***	***Time [min]***	***Sample size [mm]***	***Number of Trials***	***Scope***
Amica (HS)	60	1	10, 20, 30, 40	4, 6, 9, 5	Shrinkage analysis
		2.5	10, 20, 30, 40	4, 6, 8, 5	
		5	10, 20, 30, 40	4, 6, 9, 6	
		7.5	10, 20, 30, 40	3, 6, 9, 5	
		10	10, 20, 30, 40	4, 6, 8, 5	
Amica (HS)	60	10	56 ± 4 square base 61 ± 2 height	6	Model validation
Acculis (MS)	120	1	15, 20, 30, 40	3, 3, 3, 3	Shrinkage analysis
		2.5	15, 20, 30, 40	3, 3, 3, 3	
		5	15, 20, 30, 40	3, 3, 3, 3	
		7.5	15, 20, 30, 40	3, 3, 3, 3	
		10	15, 20, 30, 40	3, 3, 3, 3	
Emprint (CV)	100	1	20, 30, 40	3, 3, 3	Shrinkage analysis
		2.5	20, 30, 40	3, 3, 3	
		5	20, 30, 40	3, 3, 3	
		7.5	20, 30, 40	3, 2, 1	
		10	20, 30, 40	3, 3, 3	

As illustrated in Figure 2.3.2, blocks of *ex vivo* bovine liver of at least 80 mm side were placed in a plastic box, substantially transparent to MiW radiation, with an ad hoc hole for the antenna insertion in the tissue. The generator was directly connected to a computer equipped with a LabVIEW software for the monitoring of the supplied power: the incident and reflected powers were balanced to keep the net power constant at the desired level (i.e. 60 W). At least three trials were conducted for each power-time combination (Table 2.3.2), and after the microwave ablation procedure the liver was cut along the antenna axis and the extent of the carbonized area was photographed and recorded.

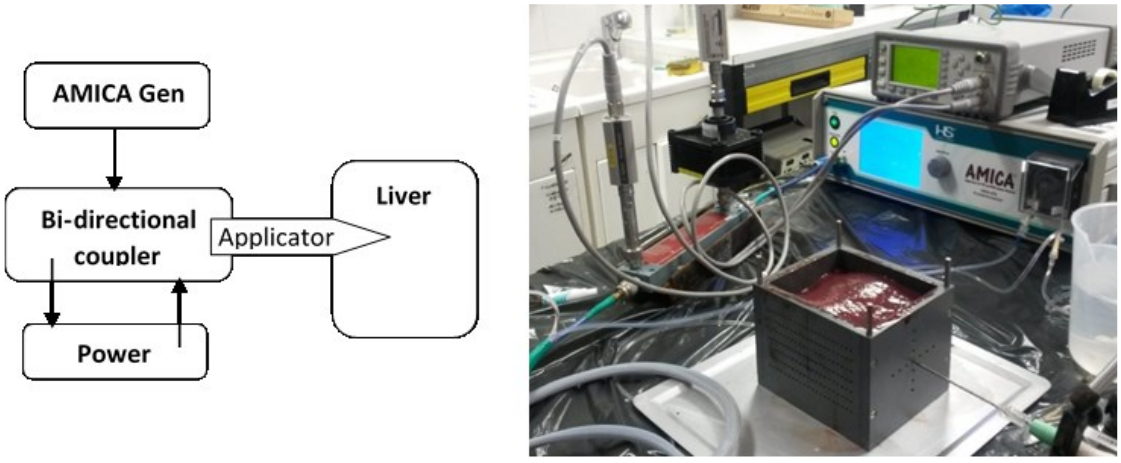

Figure 2.3.2 Schematic (left) and picture (right) of the experimental setup for MTA on un-restricted (i.e. bulk) samples of biological tissue.

Table 2.3.2 List of the MTA bulk experiments conducted.

Device	***Set Power [W]***	***Time [min]***	***Number of Trials***
Amica (HS)	60	1	4
		2.5	3
		5	3
		7.5	4
		10	4

2.3.3 MiW oven on restricted samples of tissue

Restricted samples (20 and 40 mm side cubes) of *ex vivo* liver tissue were heated using a commercial microwave oven working at 2.45 GHz (N = 18): the power value and the time of exposure were set in order to achieve a complete carbonization of the whole sample of tissue (Amabile *et al*., 2016). The experimental setup was developed to investigate the shrinkage exclusively in the carbonized tissue, independently from the energy source.

The samples were placed at the center of the cavity to obtain a homogeneous heating of the tissue as illustrated in Figure 2.3.3, and different amount of deposited energy (252 kJ to 504 kJ) were tested. The minimum energy required to achieve complete carbonization of the 20 mm side specimens was obtained supplying 420 W for 10 min (252 kJ). Then, the power-time combinations were varied increasing the deposited energy: 20 mm side cubes were heated at 420 W for 20 min (504 kJ), at 500W for 15 min (450 kJ), and at 700 W for 10 min (420 kJ). Samples of 40 mm side were completely carbonized by applying 700 W for 8 minutes (336 kJ). The cubes dimensions and weight were measured before and after the procedure, as well as the temperature at the end of the heating process. Table 2.3.3 sums up all the experiments performed detailing the specimens' size, the set combinations of MiW power and time of irradiation, and numbers of repetitions performed.

Figure 2.3.3 Experimental setup for carbonization of restricted samples of biological tissue.

Table 2.3.3 List of the MiW oven cube experiments conducted.

Sample size [mm]	***Set Power [W]***	***Time [min]***	***Number of Trials***
20	420	10	3
	420	20	3
	500	15	6
	700	10	3
40	700	8	3

2.3.4 RF ablation on restricted samples of tissue

Restricted samples of *ex vivo* biological tissue embedded in a conductive gel were led to coagulation with a purposely developed RF ablation setup working at 450 kHz (N = 6). The experimental setup was developed to investigate the shrinkage exclusively in the coagulated tissue, independently from the energy source, but in correlation with the temperature profile induced in the microwave thermal ablation heated tissue.

A straight internally cooled RF applicator with 30 mm exposed tip length, working at 450 kHz, was used (RF Amica probe, HS Hospital Service SpA, Rome, Italy) to heat cuboid specimens until an impedance increase was detected (Amabile *et al*., 2016). A monopolar RF applicator allows obtaining, in the radial direction with respect to the applicator axis, a thermal profile approximating that occurring in the only coagulated zone of MTA avoiding carbonization. The RF device was accordingly set: the energy deposition was terminated as soon as the tissues abutting the shaft were about to carbonize, i.e. as soon as an impedance rise was detected. Since most clinical applications of MTA have 5 - 10 min duration (Hoffman *et al*., 2013), the target exposure time for this experiment was chosen to be about 7 minutes and a fixed operating power (70 W) was selected to achieve an impedance rise within the required time. The maximum dimensions of the coagulated zone achievable with this power-time combination were evaluated, finding a length of about 40 mm along the applicator axis and a diameter of about 30 mm in the direction perpendicular to the applicator axis. The 30 mm diameter is also well representative of the radial extension of the only coagulated area in MTA: in the experiments conducted on unrestricted liver tissue under CT (presented later in par. 2.3.5), a radial extension of 14.5 ± 1.8 mm is measured. Thus, *ex vivo* liver tissue was cut to obtain cuboid specimens 40 mm high with a square 30 mm base, in order to reach complete coagulation of the entire tissue sample during the experiment (Table 2.3.4). The applicator was inserted along the specimens' height, at the center of the square base, and the specimens were then placed in the center of a 30 cm side plastic box filled with a conductive gel to minimize the influence of the boundary conditions. The samples were positioned to have the applicator axis parallel to the work bench, and the ground electrode of the RF system was placed on the basement of the plastic box to define a favored conductive track orthogonally to the applicator axis. The shrinkage of the tissue was measured in the direction orthogonal to the

applicator axis, where the temperature profile is indicative of that obtained in the white coagulation zone occurring in MTA procedures.

Table 2.3.4 List of the RF ablation experiments conducted.

Device	***Set Power [W]***	***Time [min]***	***Number of Trials***
Amica RF	70	10	6

2.3.5 CT monitored MiW ablation on unrestricted samples of tissue

Unrestricted samples of *ex vivo* biological tissue were dynamically investigated in real-time during a MTA treatment (N = 12), with a purposely developed setup involving a CT scan, lead markers and temperature sensors (Farina *et al*., 2015b).

The setup is illustrated in Figure 2.3.4: a plastic box, transparent to the electromagnetic field, was designed to host a block of ex vivo bovine liver and to allow accurate positioning of the MTA antenna, markers and temperature sensors. Spherical lead markers of 1.4 mm in diameter were chosen for their high visibility under CT scan, and thus to be used as fiducial following the tissue displacements due to the shrinkage without interfering with it. Experiments were performed to verify that the markers did not interfere with the electromagnetic field and with the formation of the thermally ablated area. Ad hoc holes were made on the box walls and top to allow the insertion of a grid of up to 27 spherical lead markers and up to 4 fiber-optic sensors in as much as possible predefined and reproducible positions in the tissue. Markers and temperature sensors were placed at different radial distances from the antenna axis around the antenna tip, feed and choke sections, as depicted in Figure 2.3.5. The markers' insertion and distribution were optimized to place into the tissue enough fiducials to accurately characterize the shrinkage in the three-dimensional space, i.e. at difference distances from the radiating part of the antenna, although guaranteeing a separation that would allow clearly distinguishing them.

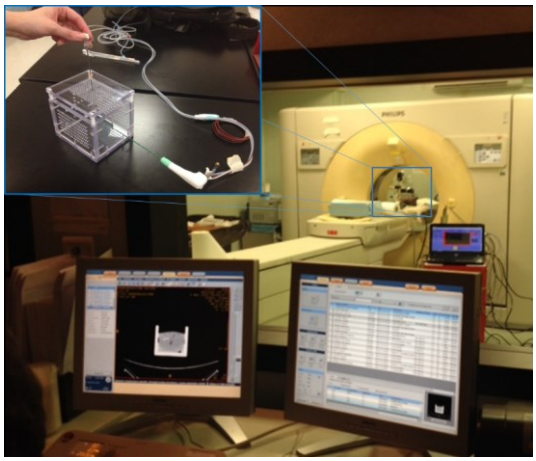

Figure 2.3.4 Experimental setup for MTA study conducted under CT control. Top-left: detail of the purposely developed box.

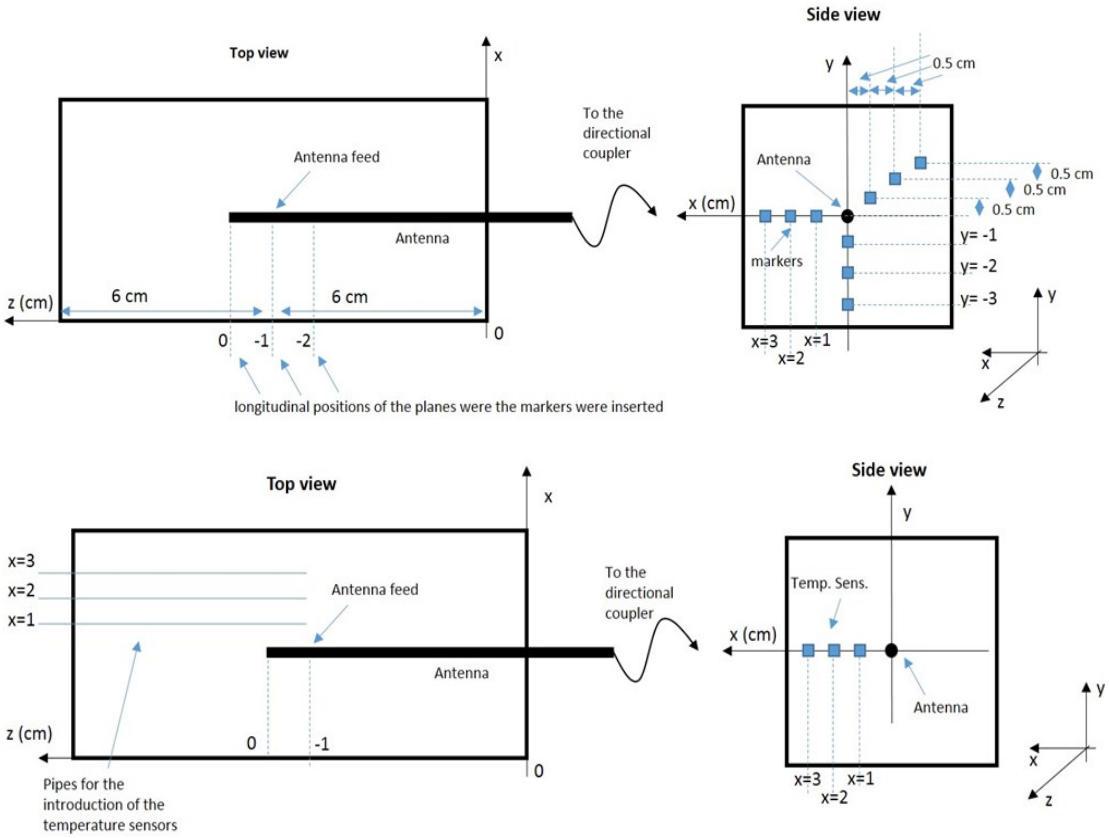

Figure 2.3.5 Schematic of the markers (top row) and temperature sensors (bottom row) positioning into the biological tissue with respect to the radiating antenna Experimental setup for MTA study conducted under CT control. Top-left: detail of the purposely developed box.

The Amica system was used to perform the ablation procedures supplying 60 W for 10 minutes at 2.45 GHz through an internally cooled 14G antenna. The box was placed in the CT gantry and the ablation procedure was performed under CT monitoring as illustrated in Figure 2.3.4. Helical CT scans were acquired setting a tube voltage of 120 kV and a tube current of 150 mAs, with a spatial resolution of 1.25 mm over a total thickness of 40 mm; a scan every 29 s was performed during the 10 min of the ablation procedure and for the subsequent 5 min. The CT system allowed detecting and tracking the markers movements, while a LabVIEW program remotely controlled and monitored the MTA system, the direct and reflected powers (measured by a power meter connected to the generator by way of a directional coupler) and the temperature sensors, automatically storing the power and temperature data (Figure 2.3.6).

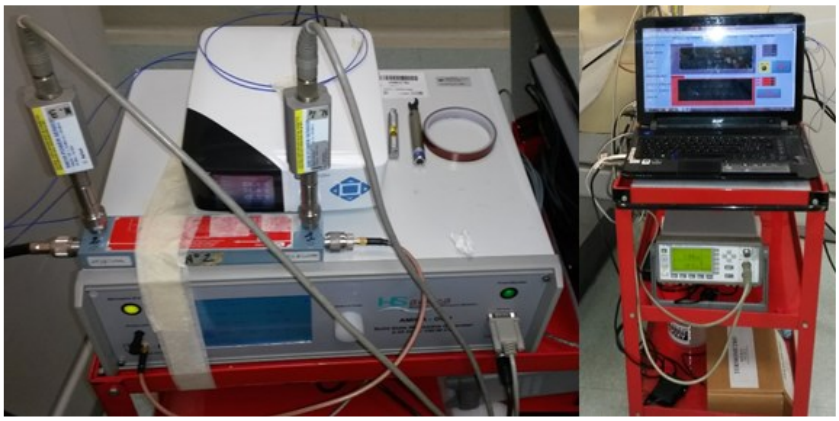

Figure 2.3.6 Experimental setup for MTA under CT control: MiW generator, directional coupler, and fiber optic thermometer (left); power meter and laptop with a dedicated LabVIEW program for procedure control and data storage.

At the end of the experiment, the tissue specimen was sectioned along a horizontal plane containing the antenna axis to evaluate and measure the dimensions of the final necrosis, with the extension of carbonized and coagulated areas. The collected data were then processed with a dedicated MATLAB program developed to analyze the CT images acquired over time before, during and after the ablation procedure. Table 2.3.5 reports details of the experiments performed: average power supplied, number of markers and/or temperature sensors, and other possible notes.

Table 2.3.5 List of the MTA bulk experiments conducted under CT control.

Date	*Trial*	*Power [W]*	*MTA Time [min]*	*CT Time [min]*	*Number of Markers*	*Number of Fiber Optics*
17.02.2014	***1***	59.08 ± 0.75	10	10	4	4
	2	59.98 ± 0.69	10	10	4	3
	3	59.50 ± 0.56	10	10	4	3
18.02.2015	***2***	58.00 ± 1.00	10	15	-	3
	4	59.20 ± 0.63	10	15	-	3
	6	58.78 ± 0.52	10	15	-	3
25.02.2015	***1***	58.35 ± 0.64	10	15	27	-
	2	59.27 ± 1.03	10	15	27	-
	3	58.78 ± 0.52	10	15	-	3
04.03.2015	***1***	59.03 ± 0.56	10	15	27	-
	2	58.94 ± 0.65	10	15	-	3
	3	59.17 ± 0.62	10	15	-	3
	4	56.47 ± 1.88	7	15	27	-

2.3.6 MiW ablation on thin samples of tissue

Ex vivo porcine liver was used to conduct experiments on thin samples of tissue, since it is naturally less thick than the bovine liver, and closer to the human liver dimensions. The experimental setup allowed evaluating the influence of sample thickness and of the presence of the capsule, a layer of connective tissue which surrounds the liver, on the size and shape of the thermally ablated area.

Tissue samples (N=12) of 20 ± 5 mm height, with and without capsule were selected to conduct the experiments. The MTA applicator was inserted at about half of the sample height, i.e. parallel to the workbench, at 10 ± 5 mm into tissue. The sample was positioned on a perforated plastic support in order to minimize the surface of contact (Figure 2.3.7). The generator was connected to the applicator through the directional coupler; this was connected to the power meter also to measure the incident and reflected powers and thus calculate the net power. Experiments were conducted with the Amica device radiating 60 W for 10 minutes. Distilled water at 10 °C was used to cool the applicator. Table 2.3.6 shows the different experiments conducted reporting the sample height and the presence or absence of the capsule.

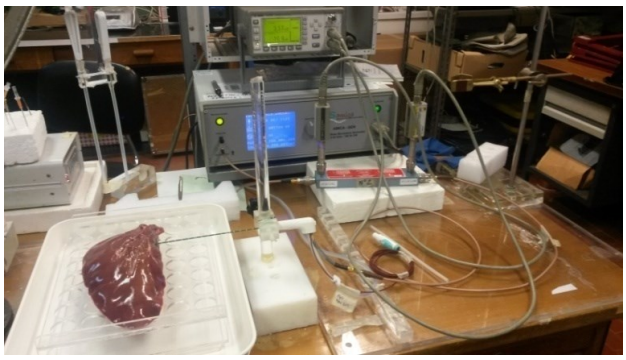

Figure 2.3.7 The experimental setup for MTA on thin samples of biological tissue.

Table 2.3.6 List of the MTA on thin samples experiments conducted.

Device	***Power [W]***	***Time [min]***	***Sample height t_i [mm]***	***Capsule***
Amica	60	10	26, 25, 28,16, 17, 16	yes
Amica	60	10	19, 19, 21,14, 24, 15	no

2.4 Setups developed for *in vivo* experimental studies

In the present section, an experimental setup for the measurements of the dielectric properties of an *in vivo* breast model realized in rat and simulating the actual condition of a human breast is depicted. The setup was optimized conducting measurements in liquids and *ex vivo* bovine liver.

2.4.1 Dielectric spectroscopy

Four liquids and *ex vivo* samples of bovine liver were used to optimize the setup for the measurements of complex dielectric permittivity. The chosen liquids were distilled water and methanol, required for the calibration and propanol and acetone, adopted as test-materials to perform the measurements because their dielectric properties are well-known at the frequencies of interest. Further tests were conducted on *ex vivo* bovine liver, whose dielectric properties are available in the literature (Gabriel *et al*., 1996a, 1996b, 1996c), to investigate the properties' variability due to tissue morphology against erroneous measured values due to the presence of air-gaps (Lopresto *et al*., 2012).

In Figure 2.4.1 , the proposed setup for broadband measurement of dielectric properties of tissues is shown: it is made of a hand-held spectrum analyzer (FSH8, Rhode & Schwarz), equipped with a tracking generator to operate as a VNA, an open-ended coaxial slim probe, and a low-phase variation coaxial cable used to connect the probe to the VNA. The probe tip inserted for a few mm depth into the sample under test allows measuring the reflection coefficient (S11) in the frequency band of interest. A custom-developed LabVIEW program running on a laptop personal computer remotely controls measurements, and a custom-developed Matlab program processes the measured S11 to derive the dielectric properties of interest.

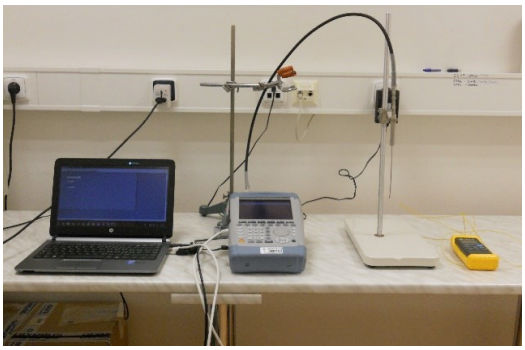

Figure 2.4.1 Portable setup for dielectric properties measurement.

The measurement procedure consists in the following steps:

1) setting of the operating frequency bandwidth;
2) calibration of the VNA to minimize the effects of phase changes at the connecting port;
3) measurement of the temperature of the reference liquids;
4) measurement of complex S11 from the four reference loads used for calibration (open circuit, short circuit, distilled water and methanol) (Marsland & Evans 1987);
5) measurement of complex S11 from the liquids or the biological samples under test;
6) post-processing of the acquired complex S11 data for calculation of broadband complex permittivity of the tested materials.

The proposed setup was optimized carrying out a large number of tests in standard liquids, using both the calibration (i.e. distilled water and methanol) and test-liquids (i.e. acetone, propanol), and in *ex vivo* bovine liver samples. The results obtained with the experimental setup were compared with data measured by a “golden standard”. The temperature of each measured material was

recorded with a thermocouple to make sure that samples had the same temperature within the same measurement session; and after each measurement, the dielectric probe was cleaned by immersion into an isopropyl-alcohol solution. The chosen bandwidth of interest was between 500 MHz and 3 GHz, i.e. the frequency range of the biomedical applications that can benefit from *in vivo* tissue characterization. In particular, the two main operating frequencies for microwave ablation (i.e. 915 MHz and 2.45 GHz) and a frequency band of interest for microwave breast cancer imaging (i.e. 500 MHz – 3 GHz) are covered ((Lopresto *et al*., 2016, Ruvio *et al*., 2014). Tests were performed setting a single bandwidth between 500 MHz and 3 GHz or two adjacent sub-bands (i.e. 500 MHz – 1 GHz and 1 – 3 GHz).

Figure 2.4.2 Example of Prague pseudo-breast model exposed by removal of skin flap.

Once optimized, the portable setup was used to perform measurements of the *in vivo* dielectric properties of a healthy breast model developed in rats from Prof. Luca Vannucci of the Academy of Sciences of the Czech Republic. Thanks to a transposition and accumulation of subcutaneous fat with a fibrous-lymphatic component, he obtains a vital and easily accessible bulk of tissues that mimic the breast in its prevalent components (Prague pseudo-breast model). In order to perform the measurements, the rats were sedated and the Prague pseudo-breast model (PB) was made available for testing by removal of skin flap (Figure 2.4.2). To better avoid interferences by neighboring structures (muscle), a space was made free below the PB positioning a histological glass, respecting the structures and the vascularization. This solution allowed modifying the position of the animal on the operating table with better exposition and stability of the PB during the measurements. It is worth noting that the fat tissue of PB is contained inside a light connectival capsule with microvascular net. The capsule was maintained for the first measurements and then it was locally

removed giving direct access to the tissue for superficial and deeper measurements. All surfaces were naturally wet due to serum and lymphatic circulation. Although bleeding was not present during the experiments, serum accumulation and active blood circulation (visible vessels) was noted. Before each measurement, temperature and size of PB were recorded. After performing *in vivo* measurements, the rat was sacrificed and further measurements were performed on PB in situ, about one hour after the sacrifice. Then, the PB was harvested and put in a Petri dish to be analyzed at about 24 hours from sacrifice. Similarly, *in vivo* and *ex vivo* measurements were performed on abdominal fat (either from the pelvis or retroperitoneal), to be used as a reference due to its homogeneity. Six different rats were examined, and five different measurements for each point were performed (average and standard deviation were then evaluated); whenever possible, different measurement points were considered, according to PB size, for a total of N = 85 measures performed *in vivo* and N = 63 *ex vivo*.

2.5 Tools for numerical studies

2.5.1 Data elaboration programs

2.5.1.1 *DICOM images*

Dedicated MATLAB programs were developed to process the data obtained through the CT scans, analyzing the acquired tomographic images and integrating the related information with those obtained from the measurements of the temperature sensors and from the post-ablation inspection of the thermally ablated area.

A first MATLAB script was dedicated to read and classify the DICOM files (Figure 2.5.1), and acquire the information of interest. The images were sorted by slice location, i.e. position along the sagittal axis (z-axis), and instant of acquisition. As second step, the position of the antenna in the 3D space was defined uniquely, thanks to the high HU value correlated to its metallic composition (pixel value = 4000); identifying the coordinates (x, y) of the antenna axis on the axial plane and the sagittal coordinate (z) for the antenna tip, as the antenna is placed parallel to the sagittal axis. Then, three different programs followed: one dedicated to the markers movement analysis (markers' script), one to the fiber optic sensors analysis, and a third for the evaluation of the pixel values corresponding to the ablated tissue.

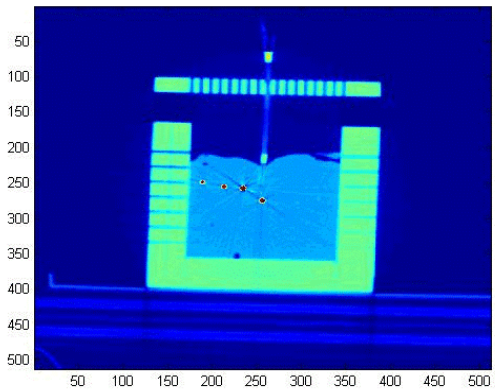

Figure 2.5.1 Example of a DICOM image obtained from the CT scan: the plastic elements (light green), i.e. the box and the fiber optic introducer, the biological tissue (light blue), and the metallic elements (red dots), i.e. the antenna (at the center of the image) and the markers (the three dots in line on the left side of the image) are clearly visible.

The markers' script allowed the markers identification and the evaluation of their absolute coordinates (axial, coronal and sagittal) and relative positions with respect to the antenna. In particular, choosing the antenna tip as origin of the coordinates, the radial distance from the antenna axis (r) and the longitudinal, i.e. along the antenna axis, distance from the antenna tip (z) were recorded for each marker. Dynamic tracking of the markers movement during the treatment was then possible: for each marker, a vector indicating its different position (x, y, z, and r) in time (approximately every 29 s) was obtained. Knowing the markers positions at the different time during the ablation procedure allowed to evaluate the displacement of each single marker, considering its distance from the antenna axis with respect to its initial position.

The script dedicated to the temperature sensors analysis allowed the identification of the fiber optic sensing tips and the evaluation of their absolute (axial, coronal and sagittal coordinates) and relative position. As for the markers case, choosing the antenna tip as origin of the coordinates, the radial distance from the antenna axis (r) and longitudinal, i.e. along the antenna axis, distance from the antenna tip were recorded for each temperature sensor. Tracking the sensors tip positions, variation of their position of a maximum of ± 2 mm were observed; being these variations comparable with the accuracy of the tool used for the identification, the initial position was chosen as stable over time. The value of the pixels adjacent to the sensor tip was then evaluated and correlated with the temperature measured dynamically during the ablation procedure. For each sensor, a vector indicating the pixels' value variation with time was obtained.

Since after the end of the procedure each specimen under treatment was cut along the antenna axis to evaluate the thermally ablated area, it was also possible to identify and classify markers, and temperature sensors by their position with respect to the carbonized, coagulated, or untreated tissue regions. Moreover, it was possible to analyze the value of the pixels during the whole ablation procedure, investigating possible changes in the tissue density due to the heating process and possible correlation with the different tissue statuses (third script). In fact, as stated before, the pixel values of a DICOM image obtained with a CT scanner are representative of the HU, i.e. of the attenuation caused by the tissue on the incident radiation, and thus of the tissue density.

2.5.1.2 *S11 data*

A dedicated MATLAB procedure was developed to process the reflection coefficient obtained through the VNA on the base of the procedure proposed in (Marsland & Evans 1987) and calculate the dielectric properties of the tested material. In accordance with (Marsland & Evans 1987), four reference load conditions were used for calibration: open circuit, short circuit, and two reference liquids, such as distilled water and methanol, whose dielectric properties are known in the operating frequency band. The complex dielectric permittivities of the standard liquids used in the calibration (i.e. distilled water and methanol) are defined by a Cole-Cole model with parameters in Table 2.5.1 to take into account their frequency dispersion:

$$\varepsilon_c(f) = \varepsilon_\infty + \frac{\varepsilon_s - \varepsilon_\infty}{1 + (j\omega\tau)^{1-\alpha}} \tag{2.1}$$

where ε_c represents the complex dielectric permittivity, ε_∞ its value at very high frequencies (in the THz region of the spectrum), ε_s is the value at low frequencies, $\omega = 2\pi f$ the angular frequency, τ the relaxation time and α a shape factor.

Table 2.5.1 Cole-Cole model of standard liquids used for calibration.

	ε_∞	ε_s	τ [ps]	α
Distilled water	5.16	78.36	8.27	0
Methanol	4.45	33.7	49.5	0.036

2.5.2 CST EM simulations

Several simulations were developed and run, by using a commercial full wave electromagnetic software (CST Microwave Studio). Aim of the simulations was to numerically evaluate the effect of the restricted dimensions of the tissue samples on the performances of MTA.

The CST Microwave Studio tool for 3D electromagnetic simulations of high frequencies components such as antennas was used to model the 14-gauge Amica antenna produced from the HS Hospital Service company, widely used in the experimental part of this work. Starting from the structure of a coaxial cable, an asymmetrical dipole with an arrowed capacitive cap and a miniaturized choke, limiting the back heating effects along the feeding coaxial line, was outlined (Figure 2.5.2) (Cavagnaro *et al*., 2011). A cylindrical camera for the internal cooling of the applicator up to the choke and a Teflon cover was added. A waveguide port was used to excite the antenna at 2.45 GHz and to supply power. Normal background and open boundary conditions were set, and an accurate mesh was defined trying to minimize the computational time. The antenna was placed in a block of biological tissue (liver) and the time domain solver was used to calculate the distribution of the electromagnetic field into the tissue and the consequent power loss. The study was performed setting a frequency interval up to 4 GHz and ensuring uniform mesh in the tissue surrounding the antenna. The results, in terms of antenna return loss (s11) and energy deployed in the biological tissue were compared with those obtained with a 2D in-house developed numerical code (supplying the same power amount), whose antenna model had been previously validated against experimental data (Cavagnaro *et al*., 2015). The Specific Absorption Rate (SAR) was punctually derived from the electric field *E*, knowing the properties of the tissue, i.e. tissue conductivity σ and tissue density ρ:

$$SAR\ [\frac{W}{kg}] = \sigma \frac{E^2}{2\rho} \quad , \tag{2.2}$$

and evaluated at different radial distances from the antenna axis for different heights along the antenna.

Once validated the reliability of the results, other simulations were conducted reducing the dimension of the tissue surrounding the antenna. The cube experimental setup of section *2.3.1* was proposed inserting the antenna in cubes of liver of 10, 20, 30, and 40 mm side, surrounded from a material with the same dielectric, thermal and mechanical characteristics of the agar phantom (9%).

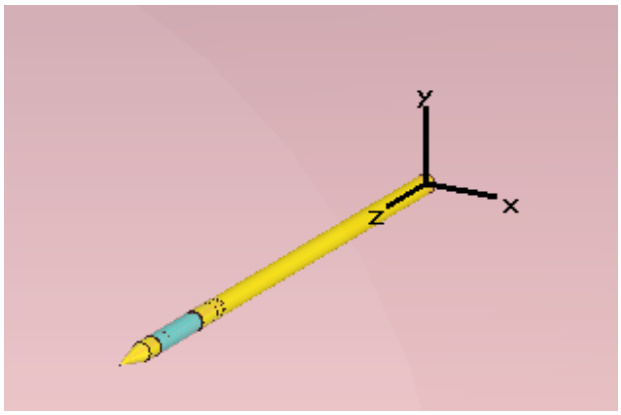

Figure 2.5.2 Antenna design, with Cartesian coordinates (CST software).

3 Results

In this chapter, all the outcomes of the performed studies are reported and discussed: the setups illustrated in the previous chapter were used to conduct several experiments; data analysis and numerical evaluations were conducted with the presented programs. Extensive experimental studies were conducted in order to characterize and model the shrinkage phenomena occurring in the thermally ablated tissue: derived from the experimental results, an analytical model for the shrinkage was proposed and validated.

Section *3.1* reports the results of the experiments performed using restricted samples of tissue, i.e. cuboids of maximum 50 mm side: this solution allowed direct and precise determination of the pre- and post-ablation specimens' dimensions to characterize the tissue contraction occurring during a MTA procedure. The Amica commercial MTA system (HS Hospital Service SpA) was firstly used and the developed setup was validated comparing the ablated area shape and dimensions obtained in restricted samples with those obtained in unrestricted tissue samples under the same operating conditions, i.e. setting the same power-time combinations. Once tested the reliability of the experimental results for restricted samples, further experiments were performed with the Amica device as well as with other two commercial systems (Acculis MTA System AngioDynamics, and Emprint^{TM} Covidien). The analysis of the obtained results led to the development of further setups for the investigation of the contraction in correlation with the two different tissue statuses present in the thermally ablated area, i.e. carbonization and coagulation. Accordingly, shrinkage was investigated in restricted samples of tissue applying different energy sources other than MTA, i.e. a MiW oven and a RF ablation system.

Section *3.2* reports the analyses conducted on the base of the results obtained on restricted tissue samples (presented in Section *3.1*). In particular, two contraction factors corresponding to the two tissue statuses were identified and implemented in an analytical model characterizing the tissue shrinkage. A predictive model for the estimation of the truly ablated area accounting for the shrinkage contribution is there proposed, and validated on restricted *ex vivo* tissue samples able to contain the induced thermal ablated volume minimizing the untreated tissue. The model was also

tested on different MTA commercial devices. Further considerations on dynamics of the tissue shrinkage in presence or absence of carbonization, i.e. in correlation with the tissue status and temperature, are reported and discussed.

Section *3.3* reports the results of the MTA experiments conducted under CT control: the data concerning the markers movements, the temperature sensors positioning and the pixel values are obtained elaborating the CT acquired DICOM images through dedicated MATLAB routines. These data are combined with those collected from the thermometer sensors and from the direct evaluation of the necrosis induced in the treated tissue. Markers' displacements are analyzed in order to better comprehend the complex shrinkage phenomenon occurring into the ablated tissue. Moreover, staring from the markers' positions at the end of the ablation and considering the dimension of the thermally ablated area, the initial position of the markers are successfully evaluated applying the predictive model (proposed in Section *3.2*). Additional analyses are conducted elaborating the temperature variations, collected through the fiber-optic sensors, and the tissue density variations, resulting from the pixels' values evaluation, occurring in real-time during the ablation procedure in the treated tissue.

Section *3.4* reports the results of the analyses conducted on the influence of the specimen's dimensions on the size and shape of the thermally ablated area. Such influence was experimentally investigated, reporting the results of the experiments conducted on thin samples of tissue, as well as numerically studied, evaluating the possible modifications in the SAR pattern introduced by the restricted dimension of the samples and their shape. The experimental setups used to ablate restricted samples of tissue (cubic and thin) are modeled and electromagnetically investigated with the CST full wave software for electromagnetic simulations described in Section *2.5.2*.

Finally, Section *3.5* reports the results of the setup optimization analysis as well as the results of the preliminary experiments conducted *in vivo* to characterize the dielectric properties of healthy breast models developed in rats.

3.1 Experiments on restricted samples of tissue

3.1.1 Experiments with the Amica MTA system

MTA ablations were conducted with the Amica device (HS Hospital Service SpA) on different-sized cubes of *ex vivo* liver tissue (10, 20, 30, and 40 ± 2 mm) radiating 60 W for different time intervals from 1 min to 10 min (for a total of N = 68 experiments). The experimental study was proposed to quantitatively characterize the tissue contraction through direct measurements of the cubes' dimensions before and after the MiW ablation procedure (Farina *et al.*, 2014a). The experiments conducted allowed distinction between longitudinal, i.e. along the antenna axis, and radial, i.e. orthogonal to the antenna axis, shrinkage.

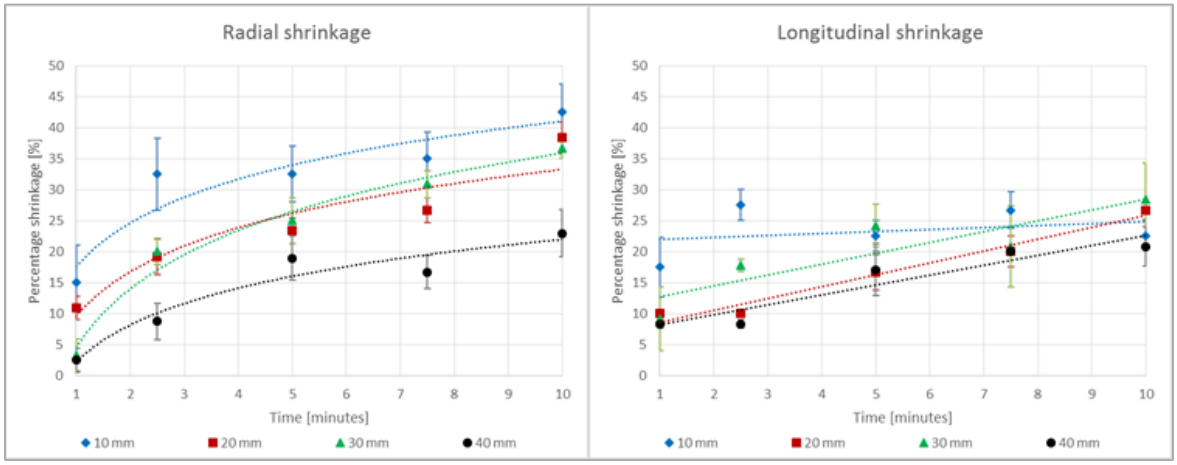

Figure 3.1.1 Percent tissue shrinkage obtained as a function of time for different cubes' size from microwave ablation performed with Amica™ system HS Hospital Service SpA; left: radial; right: longitudinal.

Figure 3.1.1reports the shrinkage measured radially to the antenna axis and longitudinally: the average values obtained are represented with their standard deviation as a function of the increasing time of ablation; trend lines are reported. Outcomes of the experiments point out two different shrinkage trends radially and longitudinally: tissue shrinks over time following a logarithmic relationship in the radial direction (R^2 = 0.87–0.98), whereas a linear relationship is observed in the longitudinal direction (R^2 = 0.77–0.97) for samples greater than 10 mm side. In the 10 mm side samples instead, a constant shrinkage of about 23 % is observed along the antenna

axis for all the considered times of ablation. For all cube sizes and times of irradiation, a more substantial shrinkage is observed in the radial direction than in the longitudinal one: e.g., at 10 min, for the 10 mm cube, the radial shrinkage is 43% and the longitudinal one 23%, and for the 30-mm cube, they are 34% and 28%, respectively. It should be noted here that in the longitudinal direction the antenna defines a mechanical boundary condition for the tissue, which is not present in the radial direction. The radial shrinkage results also greater in the smallest cubes for all times of irradiation: e.g., at 5 min the radial shrinkage is 33% for the 10 mm cube and 20% for the 40 mm cube.

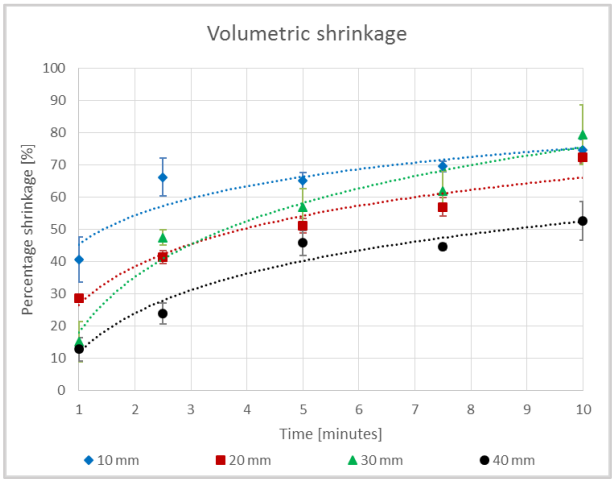

Figure 3.1.2 Percent volumetric tissue shrinkage obtained as a function of time for different cubes' size from microwave ablation performed with Amica™ system HS Hospital Service SpA.

In Figure 3.1.2, the volumetric contraction determined exploiting the samples' geometry is shown. A volume reduction in the range of 52–74% of the initial volume after 10 min is observed, with a greater shrinkage for the smallest cubes: 74% for the 10 mm side cubes and 52% for the 40 mm side cubes, after 10 min of irradiation at 60 W. For all the studied ablation times, the 10 mm cubes show a percentage volume reduction greater than the other cube sizes. The volume is already less than 50% of baseline after 2.5 min in the 10 mm side cubes, whereas larger cubes reach a similar extent of contraction after about 5 min.

Figure 3.1.3 reports the extension of the carbonized region as a function of time of ablation; the charred tissue's dimensions are directly measured after the ablation procedure sectioning the

treated samples along the antenna axis. It is possible to observe that in the 10 mm side cubes carbonization extends to 4 – 5 mm in the radial direction after 1 min of ablation, and then increases slowly with time reaching 6 mm already at 5 min. Whereas, in the larger cubes, the carbonized region increases radially more consistently with time, e.g. in the 40 mm side cubes, at 1 min extends for 4 mm and for 15.5 mm at 10 min of ablation. By contrast, the length of the carbonized region along the antenna axis does not appreciably change with time in the 10 mm side cubes, remaining approximately constant, i.e. equal to 7 mm, from the first minute of ablation. For larger cubes, carbonization reaches a maximum at a time, which depends on the cube dimensions: 2.5 min for the 20 mm side cubes, 5 min for the 30 mm cubes, whereas for the 40 mm cubes it is still increasing after 10 min. The carbonized region shows a variable extension in the different-sized cubes, including the fact that the 10 mm cubes does not extend enough to include all the carbonization achievable in solid tissue under most conditions. Yet, since in the 10 mm cubes the carbonization covers almost the whole tissue even for the shortest time of irradiation, the quantification of the shrinkage obtained in these cubes may account for the shrinkage obtainable in carbonized tissue.

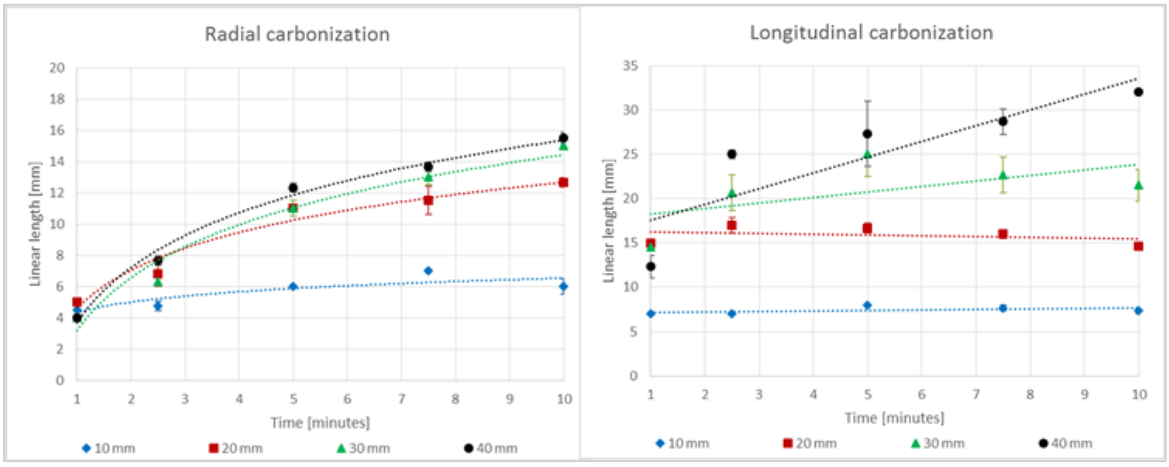

Figure 3.1.3 Absolute dimensions of carbonized tissue at the end of the ablation procedure performed with Amica™ system, HS Hospital Service SpA (HS), as a function of time for different cubes' size; left: radial; right: longitudinal.

Comparing the rate of carbonization with that of contraction, the radial dimension shows a similar behavior: e.g. a logarithmic time dependence in the 40 mm cubes, $y = 8.6 \ln(x) + 2.2$, $R^2 =$

0.93 for the shrinkage curve and $y = 5.1 \ln(x) + 3.7$, $R^2 = 0.99$ for the carbonization one (Farina *et al*., 2015a). On the other hand, during the first minutes of heating, in the longitudinal direction, the length of the carbonized region grows faster than contraction, with the only exception being the 10 mm side cubes where both carbonization and contraction slightly increase with time. More than 50% of the shrinkage occurs during the first 5 min of the treatment. Moreover, the experiments conducted on tissue cubes confirm substantial tissue shrinkage (Brace *et al*., 2010), greater for the smallest cubes. As the smaller the cube dimension, the greater the percentage of volume occupied by the carbonized tissue, the obtained results suggest that contraction occurs mainly in the tissue region where temperature reaches the highest values. Results are in agreement with the finding that contraction increases with the temperature (Rossmann *et al*., 2014), justifying the more pronounced contraction found in MiW procedures with respect to RF (Brace *et al*., 2010): indeed, in MiW ablation very high temperatures can be reached near the applicator device (i.e. up to 134 °C) (Lopresto *et al*., 2014) with respect to RF ablation (maximum 100 °C). In particular, in Lopresto et al. (2014), using similar MiW ablation equipment and performing ablations at 40 W for 10 min, temperatures higher than 98 °C up to about 6 mm radially from the antenna axis, where tissue charring occurred, were found; while temperatures between 62 °C and 98 °C were found between 6 mm and 15 mm from the antenna axis, corresponding to the surrounding necrotic zone. It follows that in the smallest cubes (i.e. at maximum 5 mm from the antenna axis), almost the whole tissue undergoes the highest temperature values, whereas the larger the cube the higher the amount of tissue undergoing lower temperature values. Accordingly, the observed shrinkage is non-uniform in time, being more consistent during the first minutes of heating and then reaching a plateau; and for the different cube dimensions, with the smallest cubes, accounting higher percent amount of carbonized tissue, showing more substantial and faster contraction.

3.1.1.1 Setup validation

To define the validity of the results obtained in restricted samples of tissue, the potential limits of the experimental setup should be investigated: the cubic shape and the sizes chosen (< 50 mm), although allows mimicking the spatial evolution of the thermally ablated area and thus investigating the shrinkage dynamics, could limit the natural evolution of the thermally ablated region. Accordingly, experiments were conducted with the MTA system Amica (HS HS Hospital Service SpA) equipped with a 14G interstitial applicator radiating in unrestricted tissue with the

power and time of irradiation equal to those used in the experiments in restricted samples: the generator was operated at 60 W for five different time intervals (1, 2.5, 5, 7.5, and 10 min), conducting three trials for each power-time combination (N = 18). After the microwave ablation procedure, the liver was cut along the antenna axis and the extent of the coagulated and of the carbonized area were measured with a ruler.

Figure 3.1.4 shows the extent of the carbonization, in the radial and in the longitudinal direction, obtained in experiments conducted in unrestricted specimens of tissue (indicated as "solid" in the figure legend); and compares these values with those obtained in the experiments conducted in cubes of tissue. The post-ablation dimensions of the treated cubes are reported as average plus min/max values (colored lines) to allow the comparison between the carbonization obtained in the cube experiments and their related post-ablation dimension, and to evaluate the influence of the cube dimension on the carbonized volume. From Figure 3.1.4, it can be noted that in the radial direction (left panel) the carbonization in the smallest cubes (i.e. 10 mm side) is considerably influenced by the cube dimension yet after the first minute of ablation; whereas for the biggest cubes this limitation does not occur. Moreover, the values measured in the cubes are reasonably comparable with those obtained in unrestricted tissue, even if a slight overestimation of the carbonization in the radial direction is showed. The right panel of Figure 3.1.4 shows that, along the antenna axis, the carbonization extension is significantly influenced by the cube dimension for all cubes, with the exception of the biggest ones (i.e. 40 mm side). In the biggest cubes, in fact, the carbonization extent is limited in the longitudinal direction only after about 10 minutes of ablation.

Figure 3.1.5 shows the dimensions of the coagulated area, in the radial and in the longitudinal direction, obtained in experiments conducted in unrestricted specimens of tissue (indicated as "solid" in the figure legend); and compare these values with those obtained in the experiments conducted on cubes of tissue. From the figure, it is evident that in the cubes the coagulated area is limited by the sample's dimensions from the first minute of ablation both radially and longitudinally, the only exception being the 40 mm cubes up to 5 minutes of ablation in the radial direction.

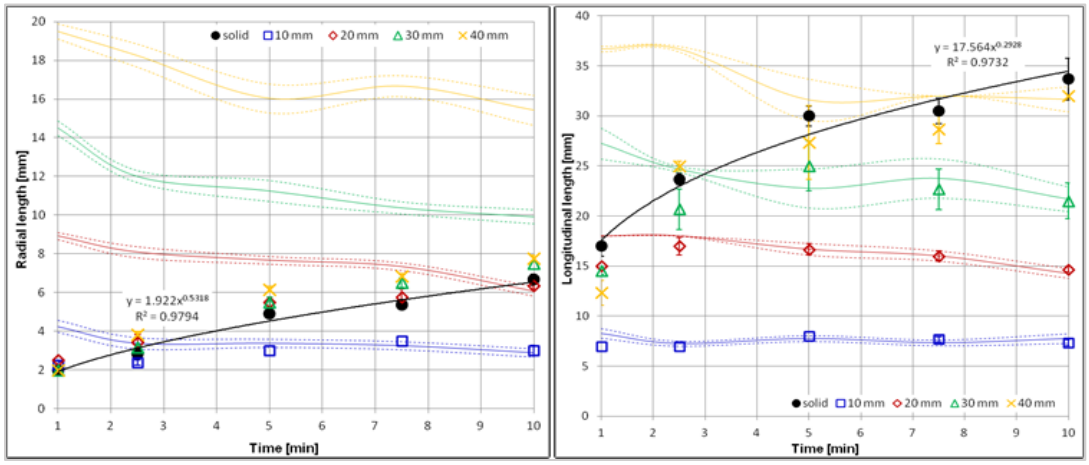

Figure 3.1.4 Comparison between the extension of the carbonized area and the post-ablation cubes' dimension; dots: carbonized area, lines: cubes' post-ablation dimension. Black line: interpolation of the unrestricted tissue data. Left: radial; right: longitudinal.

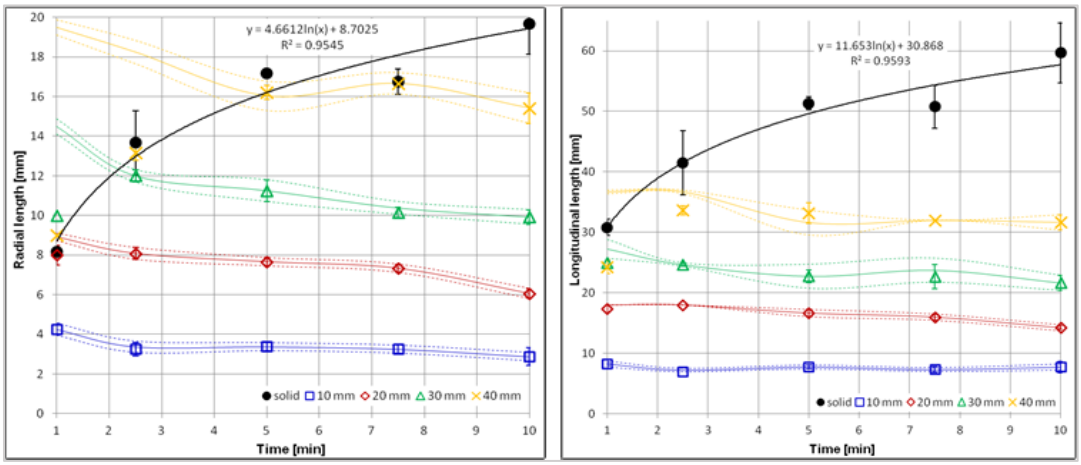

Figure 3.1.5 Comparison between the extension of the coagulated area and the post-ablation cubes' dimension; dots: carbonized area, lines: cubes' post-ablation dimension. Black line: interpolation of the unrestricted tissue data. Left: radial; right: longitudinal.

This comparison points out that the totally carbonized cubes (10 mm side) are suitable to investigate and quantify the shrinkage that occurs in the carbonized region, evidencing eventual dependence from power and time of irradiation. The 20, 30 and 40 mm cubes results suitable to investigate the carbonization and shrinkage growth occurring at increasing distances from the antenna axis, i.e. radially: the results obtained in carbonization are not affected from the cube size, and the results obtained in shrinkage allows accounting progressively increasing amounts of

coagulated tissue for the different cube dimensions. Nonetheless, only the 40 mm cubes are compatible to the analysis of the shrinkage in the whole ablated area, independently from the ablation duration, in the radial direction. On the other hand, longitudinally, the ablation evolution appears limited in all cases with the exception of the 40 mm cubes for carbonization, thus the cubes' model results less suitable for further investigation of the tissue behavior along the antenna axis.

3.1.1.2 Effect of the power variation

Experiments were conducted feeding the Amica device (N = 22) with different wattages (20, 40, 60, and 80 W) for 5 min to evaluate the effect of the increasing radiated power on the tissue shrinkage keeping constant the time of ablation (Farina *et al*., 2014a). Cubes of *ex vivo* liver tissue of 20 ± 2 mm side were used in these experiments.

In Figure 3.1.6, the results obtained in terms of percent contraction are illustrated: shrinkage linearly increases ($R^2 = 0.97$) as a function of the radiated power, reporting a contraction of 46% at 20 W, and of 56% at 80 W. The radial dimension decreases linearly with the power showing shrinkage of about 20% at 20 W and 30% at 80 W, whereas the longitudinal dimension results almost constant and equal to about 16%. At 80 W, the longitudinal contraction is substantially lower than in the other cases. However, in these experiments a liquefying of the phantom surrounding the sample of tissue was observed also, pointing to a probable breakdown of the used setup. Thus, the restricted samples of 20 mm side adopted in these experiments seem not suitable for ablation treatments above an operating power of 60 W.

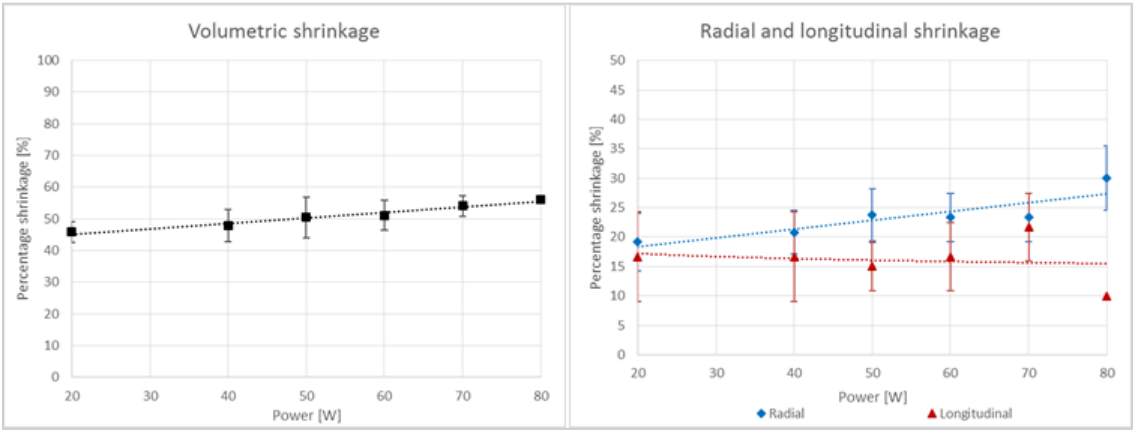

Figure 3.1.6 Percent tissue shrinkage obtained as a function of power ablating 20 mm side cubes with the MiW Amica™ system, HS Hospital Service SpA (HS), for 5 min; left: volumetric shrinkage; right: radial and longitudinal shrinkage.

3.1.1.3 Effect of different biological tissue

Further experiments were conducted to investigate different biological tissues, comparing bovine liver with turkey breast muscle (Farina *et al.*, 2014). The Amica system was used to radiate 60 W for different times (1, 2.5, 5, 7.5, and 10 min) into cubes (20 ± 2 mm side) of *ex vivo* bovine liver and *ex vivo* turkey muscle (N = 32).

Figure 3.1.7 compares the results obtained in the two different tissues as a function of time of ablation in terms of volumetric, radial and longitudinal shrinkage. A logarithmic increase of the volumetric contraction (liver: $y = 17.1 \ln(x) + 26.5$, $R^2 = 0.93$; muscle: $y = 16.0 \ln(x) + 35.6$, $R^2 = 0.99$) and of the radial shrinkage (liver: $y = 10.3 \ln(x) + 9.6$, $R^2 = 0.88$; muscle: $y = 9.3 \ln(x) + 8.5$, $R^2 = 0.98$) are observed in both tissues as a function of time. A linearly increasing trend of the longitudinal contraction with time is observed in both cases ($R^2_{liver} = 0.97$ and $R^2_{muscle} = 0.94$), but with more substantial shrinkage (16%) in the muscle cubes with respect to the liver cubes. The comparison demonstrates that the contraction induced is dependent on the type of tissue ablated, with the turkey muscle displaying a preferential direction for shrinkage, the longitudinal one; whereas the volumetric and radial contractions are not appreciably affected from the type of tissue. The observed behavior could be due to the different tissue structure and morphology (i.e. the directionality of the muscle fibers) and to the different dielectric properties of the two tissues, which likely correspond to a different absorption of the electromagnetic field. As an example, the relative permittivity and conductivity of healthy human liver at 2.45 GHz are 43.03 and 1.68 S/m, respectively; whereas those of healthy human muscle are 52.73 and 1.74 S/m, respectively (Gabriel *et al.,* 1996, http://niremf.ifac.cnr.it/tissprop/).

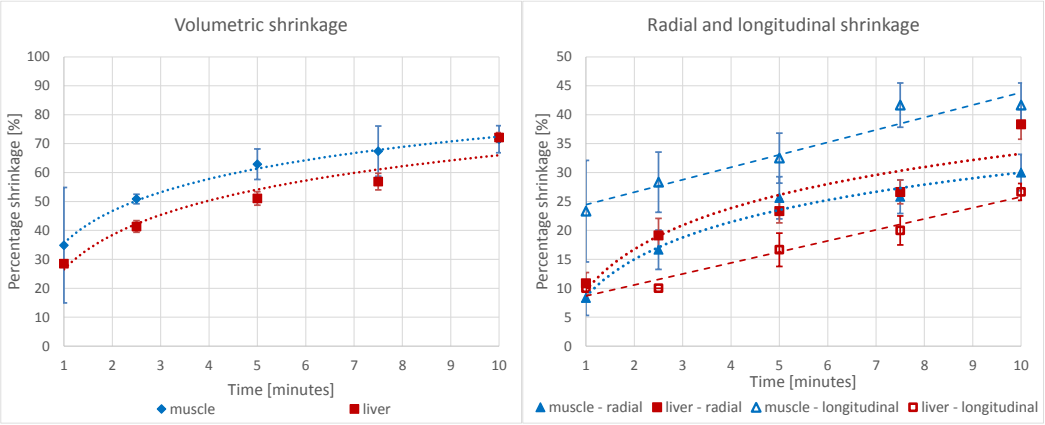

Figure 3.1.7 Percent tissue shrinkage obtained as a function of time ablating 20 mm side cubes of liver (red) and muscle (blu) with the MiW Amica™ system, HS Hospital Service SpA (HS); left: volumetric; right: radial and longitudinal..

3.1.2 Experiments with different MTA systems

Once the reliability and the limits of the setup proposed to ablate cubic samples of tissue were characterized, further experiments were conducted with the Amica system (HS) as well as with other two commercially available MTA systems, i.e. the Acculis (MS) and the Emprint (CV) systems (Farina *et al*., 2016c). Experiments were conducted ablating different-sized cubes of *ex vivo* liver tissue (side: 10, 15, 20, 30, and 40 ± 2 mm) radiating 60 W for different time intervals from 1 min to 10 min (N = 152): the 15 mm side cubes replaced the 10 mm side cubes for the MS trials, whereas with the CV system only cubes bigger than 20 mm side were adopted, due to the bigger diameter of the antenna and its limited adhesion to the tissue. The shrinkage and the carbonization evolution were thus evaluated on a device-by-device basis. As in section *3.1.1*, the tissue shrinkage was determined comparing the dimensions of the treated cubes of tissues before and after the ablation procedure. In this set of experiments, the analysis was focused on the linear dimensions of the treated samples to minimize the propagation of uncertainties of the data, linked to the volume estimation. The ANOVA test was adopted to estimate the eventual independence of the data.

In Figure 3.1.8 and Table 3.1.1, the data related to the measured shrinkage as a function of the time of ablation are reported. In Figure 3.1.8, different panels are used to analyze the phenomenon on a device basis, i.e. comparing the shrinkage obtained in the different cubes for each device. The percentage shrinkage obtained at the end of the ablation procedure for different cubes' size is graphed as a function of time of ablation: all the experimental data are reported together with the corresponding trend lines. In Table 3.1.1, the correlations observed are detailed, specifying their statistical significance. In the radial direction, i.e. orthogonal to the antenna axis, tissue shrinkage displays a logarithmic trend as a function of time of ablation for all devices and cube sizes, with values of 41 ± 7 %, 37 ± 4 %, 32 ± 5 %, and 25 ± 4 % for 10/15 (only MS and HS results), 20, 30, and 40 mm cubes respectively, after 10 minutes of ablation. For all devices, the overall contraction results greater for smaller cubes, as observed in the first set of experiments conducted with the HS system: e.g. at 10 min, the 20 mm side cubes shrink about 37 ± 4 %, whereas the 40 mm side cubes shrink about 25 ± 4 % ($p < 0.0001$). In the longitudinal direction, i.e. along the antenna axis, the

amount of shrinkage is independent of the increasing time for tissue samples treated with the MS and HS devices ($p > 0.05$). By contrast, the CV system produces a logarithmic correlation of shrinkage as a function of increasing time also in the longitudinal direction, with a maximum shrinkage of about 30 % after 10 min that does not change upon the size of the initial tissue sample.

In Figure 3.1.9 and Table 3.1.2, the data related to the dimension of the carbonized area are reported. In Figure 3.1.9, the radial and longitudinal dimensions of carbonized tissue obtained at the end of the ablation procedure as a function of time of ablation for different cubes' size are illustrated, using different panels for each device, reporting the corresponding trend lines; the observed correlations are detailed in Table 3.1.2, underlying their statistical significance. In the radial direction, the analysis of the carbonization shows a logarithmic trend as a function of ablation duration for all the considered systems (MS: $y = 3.8 \ln x + 3.6$, $R2 = 0.95$; HS: $y = 4.2 \ln x + 3.4$, $R2 = 0.97$; CV: $y = 5.6 \ln x - 1.4$, $R2 = 0.92$). In the longitudinal direction, for cubes > 20 mm side ablated with the MS and HS devices, a linear increasing trend is observed, while the smaller cubes are completely carbonized by the first minute. By contrast, for the fully internally-cooled CV device, there is a substantial 5 min delay in carbonization formation, and thus a delayed logarithmic trend is observed in both the radial and longitudinal directions. In Table 3.1.3, a detailed comparison of shrinkage as well as extension of the carbonization and of the ablated area (including carbonization) obtained for the different samples ablated for 5 and 10 minutes with the three different devices is reported.

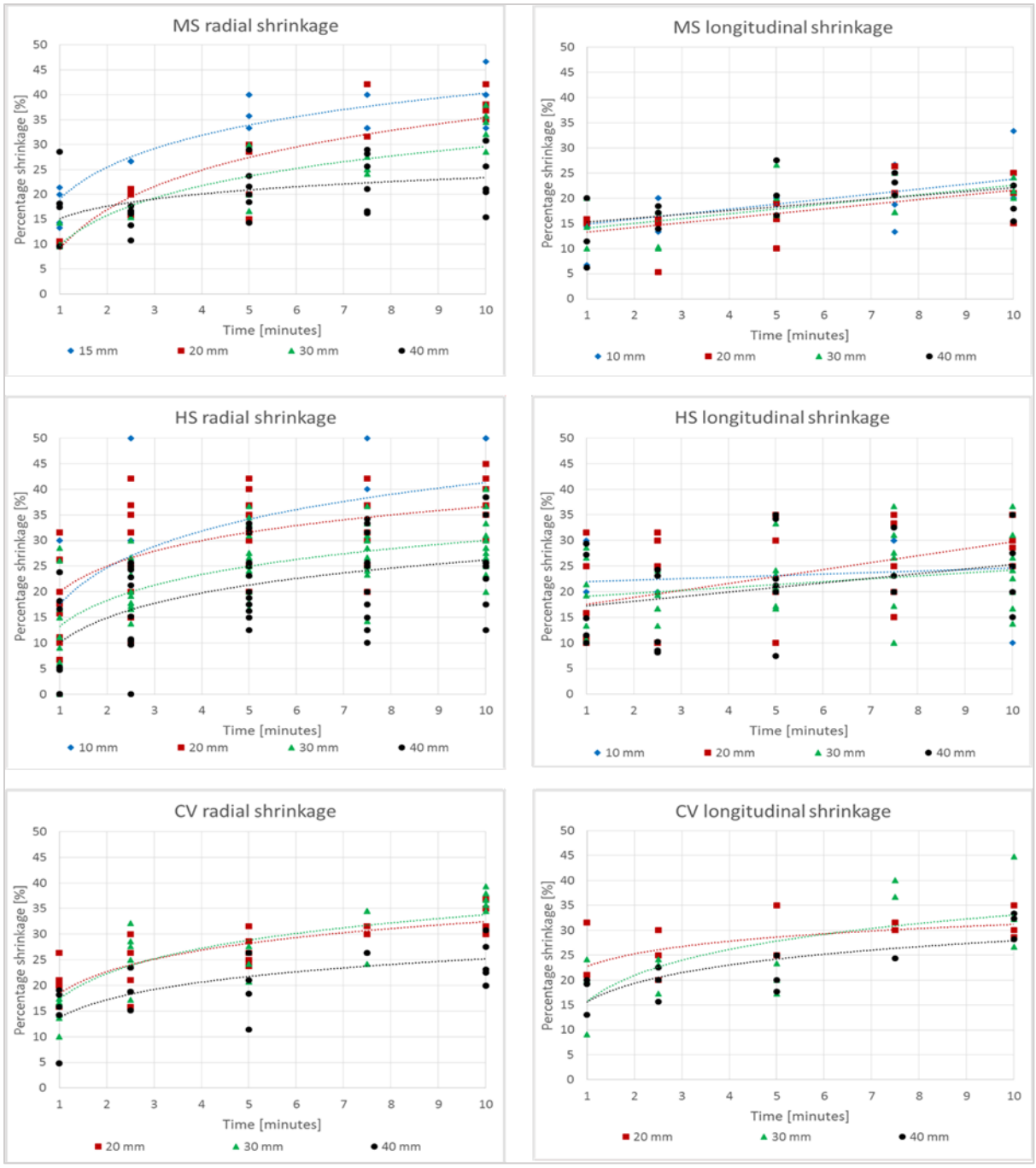

Figure 3.1.8 Percent tissue shrinkage obtained from microwave ablation as a function of time for different cubes' size and devices. From top: Acculis™ MTA System AngioDynamics (MS), Amica™ system HS Hospital Service SpA (HS), and Emprint™ Covidien (CV). Left: radial; right: longitudinal.

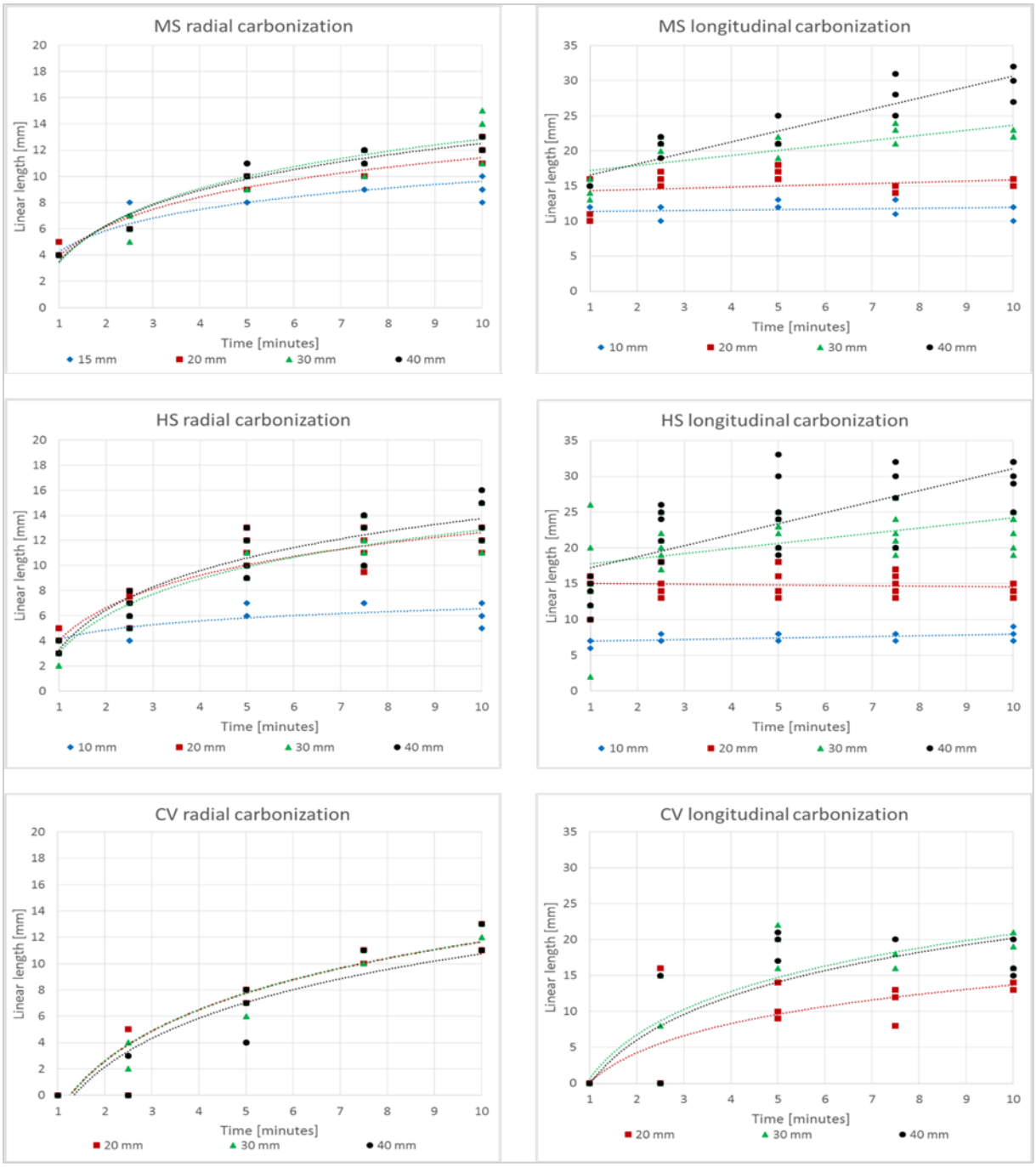

Figure 3.1.9 Absolute dimensions of carbonized tissue at the end of the ablation procedure as a function of time for different cubes' size and device. From top: Acculis™ MTA System AngioDynamics (MS), Amica™ system HS Hospital Service SpA (HS), and Emprint™ Covidien (CV). Left: radial; right: longitudinal.

Table 3.1.1 Correlation of tissue shrinkage as a function of time for the different cubes and devices. Correlations are presented as average values with standard deviation and statistical significance reported.

		Shrinkage					
		Radial			***Longitudinal***		
Device	***Cube size [mm]***	***trend***	***R^2***	***p****	***trend***	***R^2***	***p****
MS	*15*	*Logarithm*	*0.94*	< 0.05	-	-	*0.31*
	20	*Logarithm*	*0.94*	< 0.05	-	-	*0.06*
	30	*Logarithm*	*0.84*	< 0.05	-	-	*0.08*
	40	*Logarithm*	*0.76*	< 0.05	-	-	*0.11*
HS	*10*	*Logarithm*	*0.87*	< 0.05	-	-	*0.39*
	20	*Logarithm*	*0.93*	< 0.05	-	-	*0.08*
	30	*Logarithm*	*> 0.99*	< 0.05	-	-	*0.53*
	40	*Logarithm*	*0.97*	< 0.05	-	-	*0.34*
CV	*20*	*Logarithm*	*0.93*	< 0.05	*Logarithm*	*0.94*	< 0.05
	30	*Logarithm*	*0.89*	< 0.05	*Logarithm*	*0.78*	< 0.05
	40	*Logarithm*	*0.94*	< 0.05	*Logarithm*	*0.92*	< 0.05

**differences statistically not significant if p > 0.05 (ANOVA test)*

Table 3.1.2 Correlation of central tissue carbonization extension as a function of time for the different cubes and devices. Correlations are presented as average values with standard deviation and statistical significance reported.

		Carbonization					
		Radial			***Longitudinal***		
Device	***Cube size [mm]***	***trend***	***R^2***	***p****	***trend***	***R^2***	***p****
MS	*15*	*Logarithm*	*0.96*	< 0.05	-	-	*0.31*
	20	*Logarithm*	*0.96*	< 0.05	-	-	*0.06*
	30	*Logarithm*	*0.96*	< 0.05	*Linear*	*0.60*	< 0.05
	40	*Logarithm*	*0.97*	< 0.05	*Linear*	*0.94*	< 0.05
HS	*10*	*Logarithm*	*0.73*	< 0.05	-	-	*0.22*
	20	*Logarithm*	*0.97*	< 0.05	-	-	*0.58*
	30	*Logarithm*	*0.98*	< 0.05	*Linear*	*0.57*	< 0.05
	40	*Logarithm*	*0.99*	< 0.05	*Linear*	*0.80*	< 0.05
CV	*20*	*Logarithm*	*0.94*	< 0.05	*Logarithm*	*0.98*	< 0.05
	30	*Logarithm*	*0.94*	< 0.05	*Logarithm*	*0.90*	< 0.05
	40	*Logarithm*	*0.90*	< 0.05	*Logarithm*	*0.85*	< 0.05

**differences statistically not significant if p > 0.05 (ANOVA test)*

Table 3.1.3 Quantitative data of tissue shrinkage, carbonization, and extension of the ablated area. These are reported as absolute and as percentage of the ablated area for samples treated for 5 and 10 minutes.

5 minutes		***Shrinkage***				***Ablated area***		***Carbonization***			
Device	***Cube size [mm]***	***Radial***		***Longitudinal***		***Radial [mm]***	***Longitudinal [mm]***	***Radial***		***Longitudinal***	
		[mm]	***[%]***	***[mm]***	***[%]***			***[mm]***	***[%]***	***[mm]***	***[%]***
MS	*15*	6	37%	3	20%	10	12	8	88%	12	100%
	20	5	23%	3	15%	15	17	10	63%	17	100%
	30	6	19%	7	22%	24	23	10	40%	19	81%
	40	8	20%	8	21%	32	32	10	32%	22	71%
HS	*10*	3	33%	2	23%	7	8	6	93%	8	100%
	20	6	30%	5	24%	14	15	11	79%	15	100%
	30	7	25%	6	21%	23	24	10	44%	23	97%
	40	9	22%	9	23%	31	31	11	35%	25	82%
CV	*20*	5	27%	6	28%	15	14	8	52%	11	77%
	30	7	23%	6	20%	23	24	7	30%	19	81%
	40	8	20%	7	17%	32	33	6	20%	19	58%
10 minutes		***Shrinkage***				***Ablated area***		***Carbonization***			
Device	***Cube size [mm]***	***Radial***		***Longitudinal***		***Radial [mm]***	***Longitudinal [mm]***	***Radial***		***Longitudinal***	
		[mm]	***[%]***	***[mm]***	***[%]***			***[mm]***	***[%]***	***[mm]***	***[%]***
MS	*15*	6	40%	4	25%	19	11	9	100%	11	100%
	20	8	38%	4	20%	13	16	12	94%	15	96%
	30	10	32%	6	21%	20	24	14	67%	22	94%
	40	9	23%	7	18%	31	33	12	40%	30	91%
HS	*10*	4	43%	2	23%	6	8	6	100%	8	100%
	20	8	39%	6	30%	12	14	12	98%	14	100%
	30	9	29%	7	24%	21	23	13	61%	23	99%
	40	11	27%	10	24%	29	31	14	48%	30	98%
CV	*20*	6	32%	6	32%	14	14	12	90%	14	100%
	30	11	36%	10	34%	19	20	13	66%	19	95%
	40	10	24%	11	28%	31	29	12	38%	17	59%

To better understand the differences observed in correlation with the three different devices adopted, the results are directly compared in Figure 3.1.10 in terms of percentage shrinkage and extension of the induced carbonized area: the results observed as a function of time in the 30 mm

side cubes are reported. Tissue samples ablated with the MS and HS devices shows similar logarithmic trend as a function of time for shrinkage ($y = 8.8 \ln x + 9.1$, $R2 = 0.84$ for MS; $y = 7.2 \ln x + 13.3$, $R2 > 0.99$ for HS). For carbonization, a similar logarithmic trend ($y = 4.1 \ln x + 3.3$, $R2 = 0.96$ for MS; $y = 4.2 \ln x + 3.0$, $R2 = 0.98$ for HS) in the radial direction, and a similar linear trend ($y = 0.7 x + 16.5$, $R2 = 0.60$ for MS; $y = 0.7 x + 17.0$, $R2 = 0.57$ for HS) along the antenna axis are observed for the two systems. By contrast, the CV device produces shrinkage with a logarithmic trend in both the radial and longitudinal directions ($y = 7.1 \ln x + 17.3$, $R2 = 0.89$ radially; $y = 7.9 \ln x + 15.8$, $R2 = 0.78$ longitudinally); carbonization results in a delayed logarithmic trend in both the directions, too ($y = 5.7 \ln x – 1.3$, $R2 = 0.94$ radially; $y = 8.6 \ln x + 0.7$, $R2 = 0.90$ longitudinally).

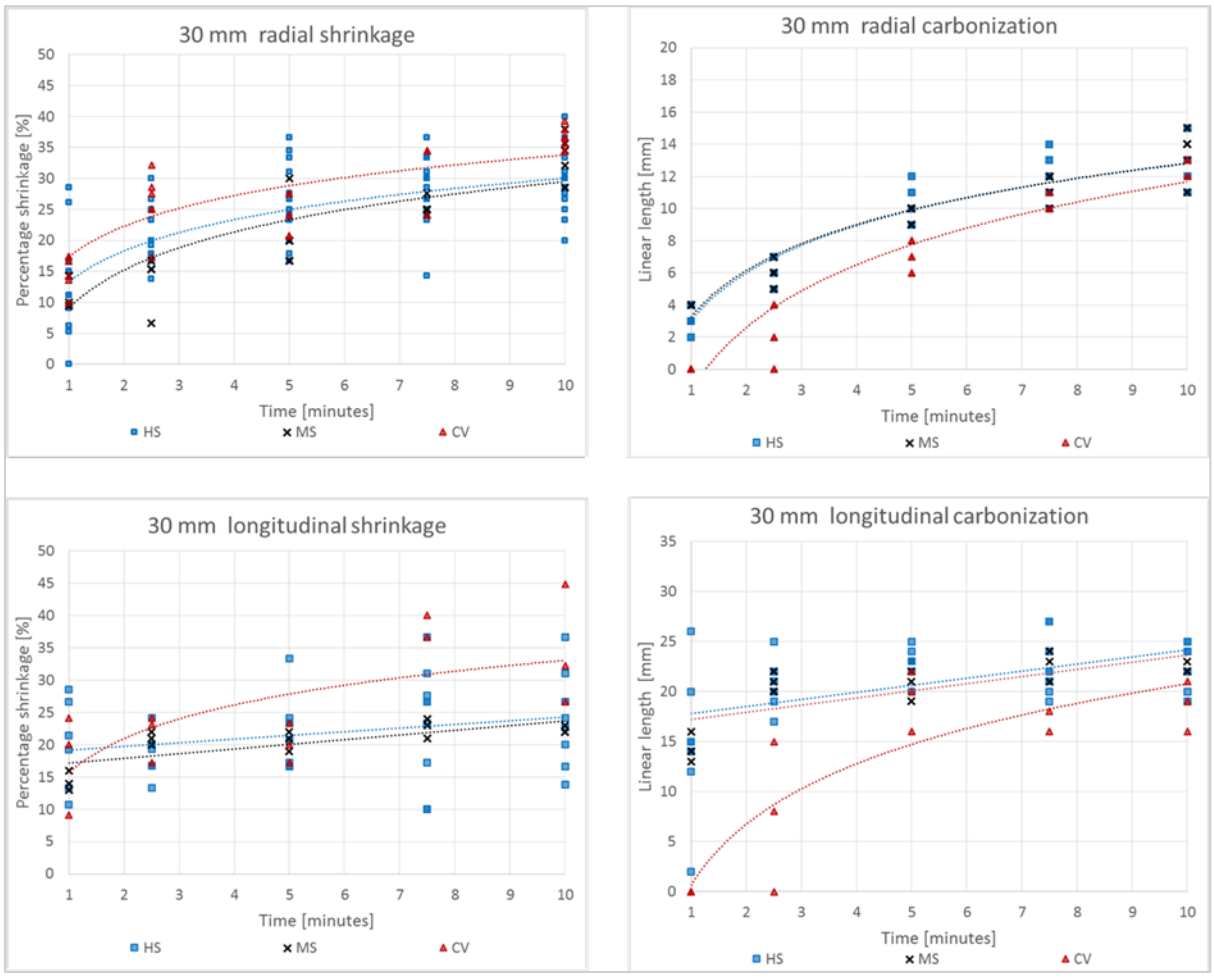

Figure 3.1.10 Percentage shrinkage (left) and absolute dimensions (right) of the carbonized area as a function of the time in the 30 mm side cubes: direct comparison of the different devices. Top: radial; bottom: longitudinal.

The experiments confirmed that once carbonization is achieved, a constant shrinkage is observed independently from the amount of energy deposited into the tissue, and independently from the ablating system adopted. Figure 3.1.11 compares the shrinkage trend and the carbonization growth as a function of time reported in the samples smaller than 20 mm side treated with the HS and MS systems, i.e. with the systems inducing carbonization from the first minute of ablation. It can be observed that from the fifth minute in the radial direction and from the first minute longitudinally, i.e. once achieved the complete carbonization of the tissue sample, the percent tissue shrinkage remains constant; although with higher values radially than longitudinally.

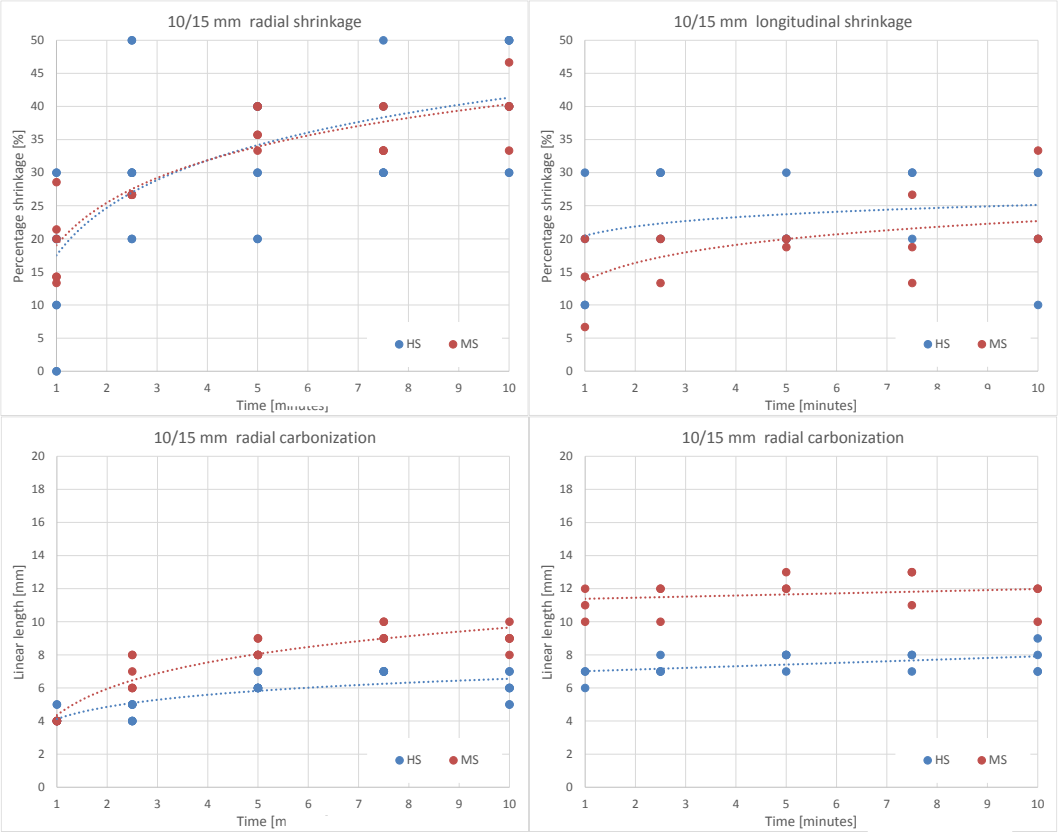

Figure 3.1.11 Percent tissue shrinkage (top) and absolute dimension of carbonization (bottom) as a function of time obtained at the end of the ablation procedure in cubes smaller than 20 mm side for two different ablating systems: Acculis™ MTA System AngioDynamics (MS), and Amica™ system HS Hospital Service SpA (HS). Left: radial; right: longitudinal.

To conclude this comparison, further similarities and differences among different MTA devices (Figures 3.1.8, 3.1.9, 3.1.10 and 3.1.11) can be noted. In the radial direction, similar trends in shrinkage are observed, whereas in the longitudinal direction, the CV device induces different

shrinkage kinetics with respect to the other two systems. Moreover, the carbonization of the tissue occurs lately during the procedure in the ablated region treated with the CV system (Figure 3.1.9). The delayed appearance of carbonization influences the longitudinal shrinkage kinetics, although it does not affect the resulting total shrinkage with respect to the other two devices (Figure 3.1.8).

3.1.3 MiW oven experiments

The results of the experiments reported in the previous paragraphs pointed out a well-defined contraction in the completely carbonized tissue samples, independent from the energy dose and from the device used (Figure 3.1.3 and Figure 3.1.11). These findings led to further investigations and to the development of a setup for the study of the tissue shrinkage of the charred tissue.

To this end, a commercial MiW oven was proposed to heat *ex vivo* bovine liver cubes up to complete carbonization of the samples (Farina *et al*., 2016a, Amabile *et al.,* 2016). Tissue samples were placed at the center of the oven cavity to obtain uniform energy deposition. The cubic shape was adopted yet again due to the easiness in performing dimensions measurements. Several preliminary experiments allowed to define the minimum energy required to achieve complete carbonization of specimens with 20 mm side: 420 W for 10 minutes. Then several power-time combinations were tested to evaluate the correlation between the shrinkage and the energy deposited into the tissue. Figure 3.1.12 compares an untreated sample of 20 mm side with one completely carbonized.

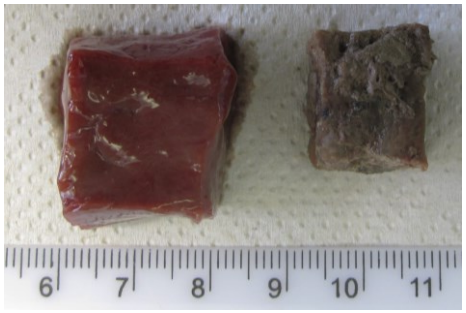

Figure 3.1.12 40 mm cube before (left), and after (right) the heating conducted in microwave oven supplying 700 W for 8 minutes. Each side of the sample decreased from 40 ± 1 mm to 27 ± 1 mm.

In Table 3.1.4 the linear dimensions of the samples before and after the heating with the MiW oven are reported, together with the estimate shrinkage; X, Y, and Z represent the three directions

in the space. From Table 3.1.4, it is readily appreciated that the range of variation (minimum – maximum values) of the calculated values are not statistically different, neither among the different directions nor among the different experiments. Thus, once a tissue completely carbonizes, shrinkage is the same whatever thermal energy is deposited into the tissue with no preferential direction. Consequently, the average value and the corresponding standard deviation can be evaluated as reported in the last two rows of Table 3.1.4 obtaining an average shrinkage of 31 ± 6 %. This data is close to the mean value of the contraction of carbonized tissue resulted in the MTA experiments, i.e. 33 ± 8 %, evaluated as the average between the radial contraction, and the longitudinal contraction. Accordingly, it can be confirmed that the shrinkage of carbonized tissue is independent from the heating modality; even if it is to be noted that the asymmetry of the shrinkage found in the MTA experiments is not found in the MiW oven experiments.

Table 3.1.4 Dimensions of the specimens before and after the heating in a microwave oven.

Trial	Heating		Before heating			After heating			Shrinkage		
	P [W]	t[min]	X [mm]	Y [mm]	Z [mm]	x [mm]	y [mm]	z[mm]	X [%]	Y [%]	Z [%]
1	420	10	22	20	18	16	13	13	27	35	28
2	420	10	18	18	14	15	13	12	17	28	14
3	420	10	20	22	15	13	13	12	35	41	20
1	420	20	18	19	20	14	13	14	22	32	30
2	420	20	22	21	20	13	13	14	41	38	30
3	420	20	21	20	17	15	14	13	29	30	24
1	500	15	20	20	20	14	14	13	30	30	35
2	500	15	21	21	20	15	15	13	29	29	35
3	500	15	20	21	20	15	14	14	25	33	30
4	500	15	20	19	20	13	14	14	35	26	30
5	500	15	20	20	19	16	13	12	20	35	37
6	500	15	20	20	20	14	14	11	30	30	45
1	700	10	20	18	19	12	12	12	40	33	37
2	700	10	19	19	19	13	11	13	32	42	32
3	700	10	22	22	21	15	14	14	32	36	33
1	700	8	40	41	40	27	26	27	32	37	32
2	700	8	40	40	39	30	28	27	25	30	31
3	700	8	41	40	40	28	25	28	32	37	30
4	700	8	39	40	39	28	27	25	28	32	36
5	700	8	40	40	40	27	28	27	32	30	32
6	700	8	40	39	40	29	27	27	27	31	32
Average shrinkage [%]										31	
Standard deviation [%]										6	

3.1.4 RF ablation experiments

A setup adopting a RF ablating system was proposed to investigate the average shrinkage occurring in the coagulated tissue, independently from the carbonized one [Farina et al 2016a, Amabile et al 2016]. RF ablations at 450 kHz were performed to heat tissue samples without causing carbonization, but inducing a thermal profile in the tissue similar to that obtained in the coagulated tissue surrounding carbonization in a MTA procedure. This equivalence is true along the radial direction where it is possible to observe a decreasing temperature profile from 100 °C to 60 °C at the edge of the ablated region (Lopresto *et al*., 2014, Rossmann *et al*., 2014). Preliminary experiments were conducted to define the optimum power-time combination to achieve white coagulation without inducing any carbonization. To avoid the occurrence of charring, the device was set to work until an impedance increase was detected, so that the energy deposition was terminated before the tissues nearby the applicator could start to carbonize. The ablation time was set to expose the sample for a time compliant with most clinical MTA treatments; accordingly, the power was set to achieve an impedance rise within the required time. After several trials, the optimum power-time combination to achieve the above-mentioned goals was obtained as 70 W for 7 minutes. The maximum dimensions of the coagulated zone achievable with this operating setup were evaluated, and cuboid specimens 40 mm high with a square base of 30 mm side were chosen as best-suitable samples to host the whole thermally ablated area minimizing the untreated tissue. Post-experiment analysis verified that at the end of the ablation protocol, the white region extended through the entire sample, as shown in Figure 3.1.13.

Figure 3.1.13 Appearance of a tissue specimen after the RF heating procedure conducted.

In Table 3.1.5, the performed trials (N=6) are detailed giving the time required to achieve the impedance rise, and the diameter of the white region before and after the heating and consequent shrinkage From the Table, an average shrinkage of 12 ± 5 % is measured for the coagulated tissue. This result is compliant with the data published by Rossmann et al. (2014) (e.g. figure 6 of that paper), that for an average exposure time of 420 s (i.e. 7 min) indicate an average shrinkage, encompassing all the temperatures between 60 °C and 95 °C, roughly around 12%.

Table 3.1.5 Initial (D_A) and final (d_A) dimensions of the specimens heated through RF ablation.

Trial	*t [min]*	*D_A [mm]*	*d_A [mm]*	*Shrinkage [%]*
1	7.5	29	24	17
2	7.0	30	26	13
3	7.0	30	27	10
4	7.0	30	28	7
5	6.0	34	28	18
6	7.0	32	30	6
Avg.	6.9	30.8	27.2	12
St. Dev.	0.5	1.83	2.04	5

3.2 Development of an analytical model of the shrinkage

In order to predict the shrinkage of the thermally ablated tissue, it is necessary to relate the coagulated zone dimension measured after the ablation to its pre-ablation value; to this end, an analytical model is hereinafter proposed and illustrated detailing its validation (Amabile *et al.*, 2016). The model is based on the results of the first set of experiments conducted with the Amica system (par. *3.1.1*), and is validated considering the results of the experiments conducted with the three commercially available devices (par. *3.1.2*). In the following paragraphs the model is illustrated first and then its validation is reported. Moreover, in the last paragraph of this section, further considerations on the dynamics of the tissue shrinkage are reported.

3.2.1 Notation

As abovementioned, thermally ablated tissues show marked differences at visual inspection. In particular, as shown in Figure 3.2.1 (left), the tissue in the peripheral zone of ablation shows a red color and results untreated, whereas more central areas show a white color, and the zone in close

proximity of the antenna appears as black (Ahmed *et al*., 2014, Yang *et al*., 2007, Lopresto *et al*., 2012). The last two zones represent the thermally ablated region, i.e. the area of successfully ablated tissue, which shows an elliptic shape with the long axis parallel to the antenna axis (Ahmed *et al*., 2014). In MTA, the white zone encompasses coagulated tissues which reached temperatures between approximately 60 °C and 100 °C, while the black region is constituted of carbonized tissues, where temperatures of 100 °C and above are reached, yielding to vaporization of the water present in the tissues (Goldberg *et al*., 2000, Yang *et al*., 2007, Lopresto *et al*., 2012).

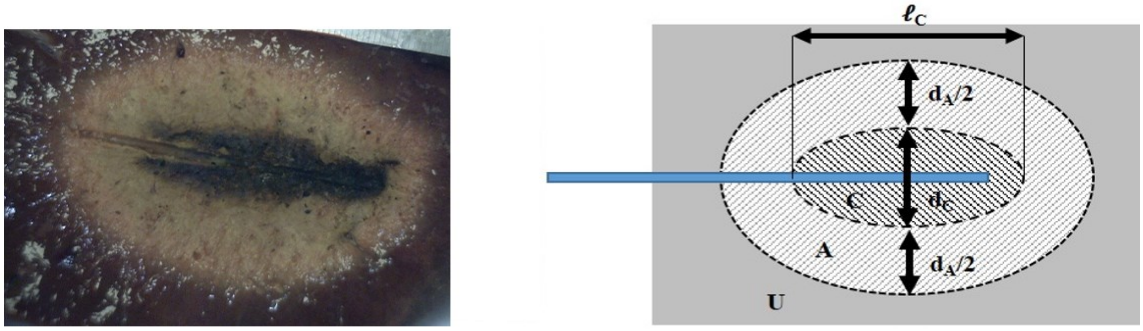

Figure 3.2.1: Image of coagulated tissue obtained after ex vivo MTA (left) and schematic representation of the appearance of the thermally ablated area (right).

In order to establish uniform co-ordinate geometry, the following notations (illustrated in Figure 3.2.1 right) are proposed to identify the quantities of interest:

1. Since generally the coagulated zone shows an elliptical cross-section in the longitudinal plane (i.e. along the antenna axis) and a cylindrical symmetry with respect to the applicator shaft, the maximum dimensions of any tissue region within the coagulated zone are characterized by two parameters along two orthogonal directions: the length "L" (along the applicator axis, i.e. longitudinal direction) and the diameter "D" (along the direction orthogonal to the applicator shaft, i.e. radial direction – see Figure 3.2.1).

2. The subscripts "U" (un-ablated), "A" (ablated, but not carbonized), and "C" (carbonized) indicate that the quantity refers respectively to the red un-ablated region, to the white coagulated region, and to the black carbonized region, respectively (Figure 3.2.1). The subscript "N" identify quantities referred to the whole thermally ablated area made of the union of the white coagulated

region (A) with the carbonized (C) one, while the subscript "T" refers to the whole specimen dimensions.

3. To distinguish between the dimensions of the different regions of the samples before and after MTA, the dimensions measured before the thermal procedure are reported as capital letters, while the same dimensions after the MTA are in lowercase: e.g. D_C gives the diameter of the carbonized region before the procedure, whereas d_C gives the diameter of the carbonized region after it. This choice is based on the intuitive picture of a smaller piece of tissue obtained after ablation treatment with respect its dimensions before the procedure, according to the shrinkage phenomena (as previously shown in Table 3.1.4).

4. The ratio between the final dimensions of a tissue region after the heating and the same quantities measured before the heating procedure are named contraction ratio and represented with the letter α. As an example, $\alpha_{C,D}$ represents the contraction ratio of the carbonized tissue along the radial direction with respect to the antenna axis ($\alpha_{C,D} = d_C/D_C$).

The p-values reported in the following to assess statistical significances were calculated through two-tails heteroscedastic t-tests.

3.2.2 Proposed analytical model

From the experiments in microwave oven, an average contraction ratio of the carbonized tissue $\alpha_C = 0.69 \pm 0.06$ is obtained, considering the average shrinkage of 31 ± 6 % observed in Table 3.1.4. However, the outcomes of the preliminary experiments conducted with the Amica system illustrated in Figure 3.1.1 and Figure 3.1.3 and detailed below in Table 3.2.1, for easiness of comprehension, indicate that the presence of the MiW applicator influences the shrinkage distribution among the spatial directions. Thus, the contraction ratio of carbonized tissue in MTA results 10% smaller in the radial direction ($\alpha_{C,D} = 0.63 \pm 0.06$ – indicating a higher contraction) and 10% larger in the longitudinal direction ($\alpha_{C,L} = 0.76 \pm 0.07$ – indicating a smaller contraction). This is probably due to a mechanical constraint introduced by the applicator, which contrasts the longitudinal shrinkage along the shaft of the antenna by inducing a friction between the tissue and the applicator external surface. Accordingly, in the MTA treated carbonized tissue a mean value of contraction of 33 ± 8 %, compliant with the carbonization contraction ration, is evaluated independently from the considered direction.

From the RF experiments, it is possible to determine an average contraction ratio of the white coagulated zone $\alpha_{A,D} = 0.88 \pm 0.05$ (Table 3.1.5). Unlike the carbonized zone, which is in direct contact with the applicator, there is no contact surface between the white region and the applicator. Accordingly, the presence of the applicator should not yield to a significant asymmetry of the contraction ratio. Consequently, the value derived in the orthogonal direction with respect to the applicator axis can be assumed valid also in the longitudinal direction, i.e. in the direction parallel to the applicator axis.

Table 3.2.1 Contraction ratios of completely carbonized specimens ableted with the Amica™ system (section 3.1.1).

Power/Time setting	Trial	cube side [mm]	$\alpha_{C,D} = d_C / D_C$	$\alpha_{C,L} = \ell_C / L_C$
60 W 5 min	1	10	0.60	0.80
	2		0.60	0.80
	3		0.60	0.80
	4		0.70	0.70
60 W 7.5 min	1	10	0.70	0.70
	2		0.70	0.80
	3		0.70	0.80
60 W 10 min	1	10	0.70	0.70
	2		0.50	0.80
	3		0.60	0.70
	4		0.60	0.90
60 W 10 min	1	20	0.65	0.75
	2		0.60	0.70
	3		0.65	0.75
	4		0.55	0.65
		Avg.	0.63	0.76
		St. Dev.	0.06	0.07

To summarize in formulae:

$$\alpha_{C,D} = \frac{d_C}{D_C} = 0.63 \pm 0.06 \tag{3.1a}$$

$$\alpha_{C,L} = \frac{\ell_C}{L_C} = 0.76 \pm 0.07 \tag{3.1b}$$

$$\alpha_A = \frac{d_A}{D_A} = \frac{\ell_A}{L_A} = 0.88 \pm 0.05 \tag{3.2}$$

From the above reported data, the dimension of the tissue involved in the ablation procedure, i.e. coagulated at the end of the MTA, can be derived according to the formula:

$$D_N = D_C + D_A = \frac{d_C}{\alpha_{C,D}} + \frac{d_A}{\alpha_A} \tag{3.3}$$

$$L_N = L_C + L_A = \frac{\ell_C}{\alpha_{C,L}} + \frac{\ell_A}{\alpha_A} \tag{3.4}$$

for the radial (eq. (3.3)) and longitudinal (eq. (3.4)) directions with respect to the antenna axis. Both in laboratory and clinical field, d_C and d_A (and ℓ_C and ℓ_A) can be measured at the end of the ablation and, although with less accuracy, during the same. Tissue shrinkage can be therefore known and predictable being known the coefficients $\alpha_{C,D}$, $\alpha_{C,L}$ and α_A.

It is worth noting that while the shrinkage of carbonized tissue proved to be power-time independent (par. 3.1.3) and correctly represented by a constant parameter, in the case of white coagulation this is not true, and therefore the proposed value represents an average shrinkage of the zone where temperatures between 60 °C and 100 °C are experienced by the tissue, according the temperature profile typical of MTA. Moreover, comparing the contraction ratio defined for the carbonized tissues with the one defined for the coagulated tissues, the first is significantly smaller ($p < 10^{-4}$). A smaller contraction ratio results in a higher shrinkage, i.e. in a greater reduction of the extension of the tissue after the heating procedure. The proposed model provides a simple link between the thermally ablated area, measured at the end of the MTA, and the dimension of the tissue before the procedure; accordingly, it does not take into account the expansion phenomena observed in MTA during the very first minutes of the procedure (Farina *et al.,* 2014a, Weiss *et al.,* 2015).

3.2.3 Model validation with the Amica MTA system

To validate the above reported equations, experiments were conducted ablating for 10 minutes at 60 W cuboid samples (N = 6) of *ex vivo* liver of a square base of 56 ± 4 mm side and a height of 65 ± 2 mm with the Amica MTA system (Amabile *et al*., 2016). These specimens were purposely cut to entirely host the thermal ablated volume induced with the power-time combination set minimizing the untreated tissue, as shown in Figure 3.2.2.

Figure 3.2.2 Appearance of a tissue specimen after the MTA procedure conducted supplying 60 W at 2.45 GHz for 10 min.

After the treatment, the extensions of only coagulated and carbonized zones were measured along the antenna axis (ℓ) and in the orthogonal direction (d): the initial and final linear dimensions of the specimens and the dimensions of the two zones are reported in Table 3.2.2, following the notation illustrated in the previous section. It is worth remarking that d_A refers to the coagulated zone only, thus it does not account carbonized tissue. From Table 3.2.2, it can be noted that the carbonized and coagulated regions do not extend across the whole specimens (i.e. $d_C + d_A < d_T$), and similarly along the antenna axis (i.e. $\ell_C + \ell_A < \ell_T$), i.e. some tissue remained untreated. In particular, from Table 3.2.2, the extension of the untreated tissue can be obtained as the difference between the dimension of the specimen after the heating procedure and the sum of the carbonized and white coagulated region extension.

Table 3.2.2 Dimensions of the specimens ablated with the Amica™ system before and after the heating.

	Before heating				**After heating**			
Trial	L_T [mm]	D_T [mm]	ℓ_T [mm]	d_T [mm]	ℓ_C [mm]	d_C [mm]	ℓ_A [mm]	d_A [mm]
1	65	55	58	50	35	14	19	25
2	65	60	53	46	32	13	14	23
3	60	50	52	48	32	12	18	26
4	67	59	54	51	32	13	13	26
5	66	58	51	48	32	13	15	27
6	65	55	55	47	32	11	17	28
Avg.	64.7	56.2	53.8	48.3	32.5	12.7	16.0	25.8
St. Dev.	2.42	3.66	2.48	1.86	1.22	1.03	2.37	1.72

At this point, equations (3.3) and (3.4) can be used to evaluate the extension of the coagulated tissue before the procedure. The obtained value, plus the extension of the untreated tissue, can be compared with the dimension of the specimen before the MTA procedure. Table 3.2.3 and Table

3.2.4 give the corresponding data for the radial (i.e. orthogonal to the applicator axis) and longitudinal (i.e. parallel to the applicator axis) directions, respectively, together with the difference (error) between the analytical and the experimental data. Looking at the average data, it can be noted that the extensions of the specimens obtained with the analytical model are close to the experimental values in both the radial and longitudinal directions. Given an estimated experimental accuracy of 1 mm in the measurement of the extension of the different zones (see par. 2.3); the model based on the measurement of three parameters (carbonization, coagulation, and whole sample of tissue extensions) has a total uncertainty of 3 mm. Looking at the errors evaluated in Table 3.2.3 and Table 3.2.4, it is possible to note that the average values are within the experimental uncertainty. In particular, looking at each single experiment, the data result within the experimental variability with the exception of trials 1 and 3 for both the longitudinal and radial directions.

Table 3.2.3 Dimension of the specimens before the MTA treatments, evaluated through the proposed analytical model (D_T) and measured (D_T exp). Direction orthogonal to the microwave applicator axis.

Trial	$D_U=d_T-(d_C+d_A)$ [mm]	$D_C=d_C/\alpha_{C,D}$ [mm]	$D_A=d_A/\alpha_A$ [mm]	$D_T=D_C+D_A+D_U$ [mm]	D_T exp [mm]	Error [mm]
1	11	22.2	28.4	61.6	55	6.6
2	10	20.6	26.1	56.8	60	-3.2
3	10	19.1	29.6	58.6	50	8.6
4	12	20.6	29.6	62.2	59	3.2
5	8	20.6	30.7	59.3	58	1.3
6	8	17.5	31.8	57.3	55	2.3
Avg.	9.8	20.1	29.4	59.3	56.2	3.1
St. Dev.	1.6	1.6	2.0	2.2	3.7	4.2

Table 3.2.4 Dimension of the specimens before MTA experiments, evaluated through the proposed analytical model (L_T) and measured (L_T exp). Direction parallel to the microwave applicator axis.

Trial	$L_U=\ell_T-(\ell_C+\ell_A)$ [mm]	$L_C=\ell_C/\alpha_{C,L}$ [mm]	$L_A=\ell_A/\alpha_A$ [mm]	$L_T=L_C+L_A+L_U$ [mm]	L_T exp [mm]	Error (mm)
1	4	46.1	21.6	71.6	65	6.6
2	7	42.1	15.9	65.0	65	0.0
3	2	42.1	20.5	64.6	60	4.6
4	9	42.1	14.8	65.9	67	-1.1
5	4	42.1	17.1	63.2	66	-2.9
6	6	42.1	19.3	67.4	65	2.4
Avg.	5.3	42.76	18.2	66.3	64.7	1.6
St. Dev.	2.5	1.6	2.7	3.0	2.4	3.6

Finally, Table 3.2.5 gives the absolute shrinkage of carbonized and white coagulated tissue in the radial (D_C - d_C) and longitudinal (L_C - ℓ_C) directions as evaluated through the model. From the table, it can be inferred that over an average total longitudinal shrinkage of 12.5 mm (i.e. Avg (L_C - ℓ_C) + Avg (L_A - ℓ_A) = 10.3 mm + 2.2 mm), up to 10.3 mm (i.e. about 82.5% of total longitudinal contraction) are linked to the shrinkage of carbonized tissue. Likewise, over an average total radial contraction of 10.9 mm, 7.4 mm are due to the shrinkage of carbonized tissue (i.e. about 67.9% of total radial contraction). Thus, the contribution to the total shrinkage of the white zone contraction is therefore appreciably lower than the contribution of the carbonized zone and can likely even be neglected as a first approximation for many clinically relevant scenarios. Even with such an approximation, the agreement between the model prediction of the tissue extension before the MTA and its measured values would be characterized by a maximum error of 6 mm and 5 mm in the radial and longitudinal directions, respectively, and by an average error of 0.39 mm and 0.57 mm in the radial and longitudinal directions, respectively. Given the experimental determination of the contraction ratios (equations (3.1) and (3.2)), the contribution to the total contraction of the white coagulated tissue contraction is negligible (smaller than 10%) when $d_C/d_N \geq 0.70$ and $\ell_C/\ell_N \geq 0.81$. Similarly, the contraction of the carbonized tissues is negligible when $d_C/d_N \leq 0.02$ and $\ell_C/\ell_N \leq 0.04$ (Amabile *et al*., 2016).

Table 3.2.5 Absolute shrinkage of white coagulated and carbonized region as obtained through the model.

Trial	$D_C - d_C = d_C(1-\alpha_{C,D})/\alpha_{C,D}$ [mm]	$D_A - d_A = d_A(1-\alpha_A)/\alpha_A$ [mm]	$L_C - \ell_C = \ell_C(1-\alpha_{C,L})/\alpha_{C,L}$ [mm]	$L_A - \ell_A = \ell_A(1-\alpha_A)/\alpha_A$ [mm]
1	8.2	3.4	11.1	2.6
2	7.6	3.1	10.1	1.9
3	7.1	3.6	10.1	2.5
4	7.6	3.6	10.1	1.8
5	7.6	3.7	10.1	2.1
6	6.5	3.8	10.1	2.3
Avg.	7.4	3.5	10.3	2.2
St. Dev.	0.6	0.2	0.4	0.3

3.2.4 Model validation with different MTA systems

Successively, the proposed model was tested on the data obtained by the experiments conducted on restricted cubic samples with three different commercially available systems. The shrinkage factors proposed (eq. (3.1) and (3.2)) were applied to the experimental results obtained with the Amica (HS), Acculis (MS) and Emprint (CV) MTA systems presented in par. *3.1.2*, in order to evaluate the pre-ablation dimensions of the tissue samples starting from the post-ablation measurements, i.e. carbonized and coagulated region extensions, and final specimen sizes. For the experiments conducted with the Acculis device, the mathematical model is able to predict the initial samples dimensions in 96 % of the cases (i.e. 115 over 120) in the radial direction and in 90 % of the cases (i.e. 54 over 60) in the longitudinal direction. The observed error range is [-3; 4] mm in the radial and [-3; 5] mm in the longitudinal directions, as highlighted in Table 3.2.6. For the experiments conducted with the Amica device, the mathematical model results able to predict the initial samples dimensions in 92% of the cases (i.e. 92 over 100 measures) in the radial direction and in 88% of the cases (i.e. 44 over 50) in the longitudinal direction. The observed error range is [-6; 4] mm in the radial direction, and [-7; 4] mm in the longitudinal one as highlighted in Table 3.2.7. For the experiments conducted with the Emprint device, the mathematical model results able to predict the initial samples dimensions only for the samples ablated for at least 5 min, i.e. accounting carbonized tissue, in 98% of the cases (i.e. 47 over48 measures) in the radial direction and in 83% of cases (i.e. 20 over 24 measures) in the longitudinal direction. The observed error range is [-8; 3] mm radially and [-4; 3] mm longitudinally, as highlighted in Table 3.2.8. The errors resulted acceptable considering an accuracy of 5-10 mm in the clinical practice, and from the tables it is possible to notice that the model tends to underestimate the initial samples dimensions longitudinally, i.e. along the direction more difficult to model due to the presence of the antenna. However, underestimation of the pre-ablation dimensions is preferable than overestimation willing to guarantee the complete ablation of the targeted tissue, and thus ensure the destroying of the whole tumor.

Table 3.2.6 Average (Avg) error observed in applying the model to the Acculis™ (MS) results.

MS	15 mm			20 mm			30 mm			40 mm		
	Avg [mm]	Min [mm]	Max [mm]	Avg [mm]	Min [mm]	Max [mm]	Avg [mm]	Min [mm]	Max [mm]	Avg [mm]	Min [mm]	Max [mm]
1 min	1	-1	3	2	1	3	2	1	3	1	-3	5
2.5 min	0	-1	2	2	1	4	3	1	4	2	1	3
5 min	0	-1	1	2	0	4	1	-3	3	0	-3	4
7.5 min	0	-1	2	0	-2	1	1	0	3	0	-2	4
10 min	-1	-2	1	0	-2	2	0	-3	1	1	-3	4

Table 3.2.7 Average (Avg) error observed in applying the model to the Amica™ (HS) results.

HS	20 mm			30 mm			40 mm		
	Avg [mm]	Min [mm]	Max [mm]	Avg [mm]	Min [mm]	Max [mm]	Avg [mm]	Min [mm]	Max [mm]
1 min	-1	-2	2	1	-3	4	-1	-4	3
2.5 min	-2	-3	0	1	-4	3	-2	-3	-1
5 min	-1	-3	1	0	-3	3	-3	-7	1
7.5 min	-1	-3	1	0	-3	4	-3	-6	0
10 min	-1	-3	1	1	-3	4	-3	-6	-1

Table 3.2.8 Average (Avg) error observed in applying the model to the Emprint™ (CV) results.

CV	20 mm			30 mm			40 mm		
	Avg [mm]	Min [mm]	Max [mm]	Avg [mm]	Min [mm]	Max [mm]	Avg [mm]	Min [mm]	Max [mm]
5 min	0	-3	1	0	-2	1	-1	-4	2
7.5 min	0	-3	1	-3	-7	1	-1	-2	-1
10 min	-1	-3	2	-3	-8	-1	-2	-5	1

The analytical model, as presented in par. *3.2.2*, foresees the presence of charred tissue. Therefore, some consideration should be done to apply it in absence of carbonization as occurred in the CV experiments within the first minutes of ablation (< 5 min – par. *3.2.1*). In the CV only coagulated samples, the tissue close to the antenna feed does not carbonize although its proximity to the energy source, as visible from Figure 3.2.3. Nevertheless, the shrinkage factor proposed in eq. (3.2) for the only coagulated tissue is not suitable to characterize the tissue in the CV only coagulated samples' case, due to the presence of traces of carbonization around the antenna feed

that let suppose a higher temperature profile (Figure 3.2.3). It is possible to surmise that in close proximity to the antenna feed due to the direct absorption of the electromagnetic field, the temperature increases without inducing sizable tissue charring. Presumably, the tissue of the only coagulated samples are characterized from a thermal profile similar to that depicted in Figure 3.2.4.

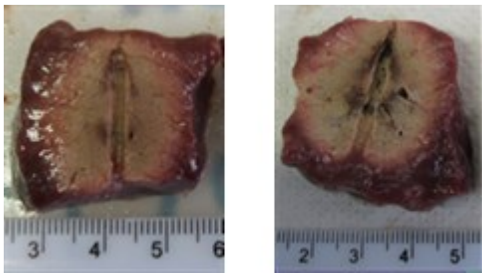

Figure 3.2.3 Appearance of cubes ablated for 1 min (left) and 2.5 min (right) with the Emprint ™ system.

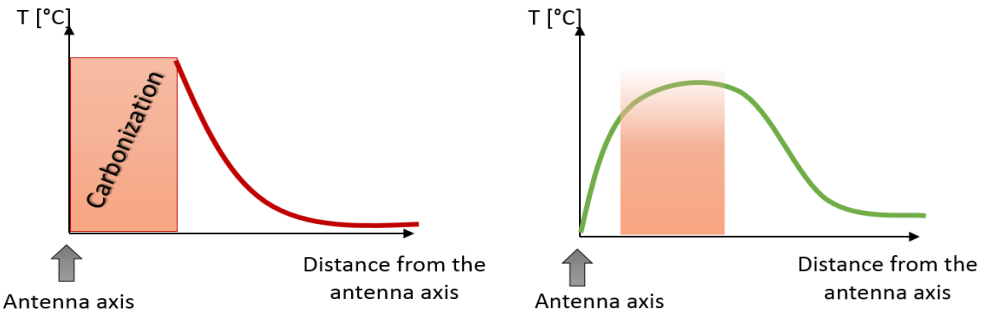

Figure 3.2.4 Sketch of the presumible thermal profile occurring in the MTA treated tissue radially to the antenna feed. Left: in presence of carbonization (HS and MS cases); right: in absence of carbonization (CV case < 5 min).

In absence of carbonization, an average linear contraction ratio of $\alpha_{A,D} = 0.83 \pm 0.03$ in the radial direction and of $\alpha_{D,L} = 0.79 \pm 0.04$ in the longitudinal direction are derived from the shrinkage measured in the cubes ablated for 1 and 2.5 min with the Emprint system. These two values are statistically dependent (p-value > 0.05), thus the asymmetry results not significant for the only coagulated samples treated with the Emprint system and an average contraction ratio, independent from the direction, can be evaluated as $\alpha_A = 0.82 \pm 0.05$. In these experiments, symmetric contraction is observed probably due to the cooling system adopted that cools the antenna till its tip preventing the tissue next to the antenna axis to reach temperatures higher than 100 °C, and thus carbonize and adhere to the antenna surface, as visible in Figure 3.2.3.

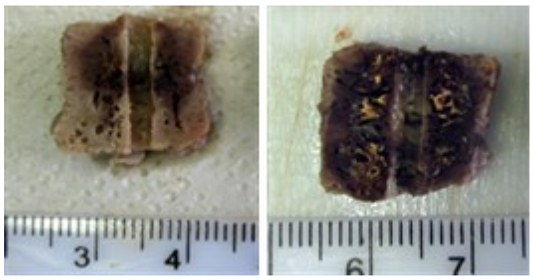

Figure 3.2.5 20 mm cubes ablated for 5 min (left) and 10 min (right) with the Emprint ^{TM} system.

A less consistent adhesion of the tissue to the CV antenna surface is pointed out also in tissue samples that account carbonization, i.e. ablated for at least 5 minutes: Figure 3.2.5 shows that a coagulated-not-carbonized part of tissue (of variable thickness, up to 1 mm) is always observable between the antenna surface and the inner border of the carbonized region. Thus, carbonization influences differently the global tissue shrinkage in CV, in particular the asymmetry among the radial and the longitudinal direction results minimized likely due to the absence of direct contact between carbonized tissue and antenna surface. Accordingly, looking at cuboid tissue samples of 20 mm side ablated with the Emprint system, at 10 minutes they show a similar amount of carbonization extension (Figure 3.2.6 left) and result almost completely carbonized in both directions ($d_T - d_C \leq 2$ mm, $\ell_T - \ell_C \leq 1$ mm), as observable in Figure 3.2.5 (right). Correspondingly, average linear shrinkage of 34 ± 3 % in the radial direction and of 32 ± 3 % in the longitudinal direction are observed (Figure 3.2.6 right). Contraction results independent from the direction (p-value > 0.05) and on average equal to 33 ± 2 %, i.e. corresponding to a contraction ratio of 0.67 ± 0.02. This value calculated from the cubes totally carbonized by the Emprint device is within the experimental variability of the contraction factor $\alpha_C = 0.69 \pm 0.06$ proposed in par. *3.2.2*, thus confirming the validity of the model, as validated previously in this paragraph (Table 3.2.8) and supporting the independence of the shrinkage in the charred tissue from the heating source and process, and amount of energy deposited.

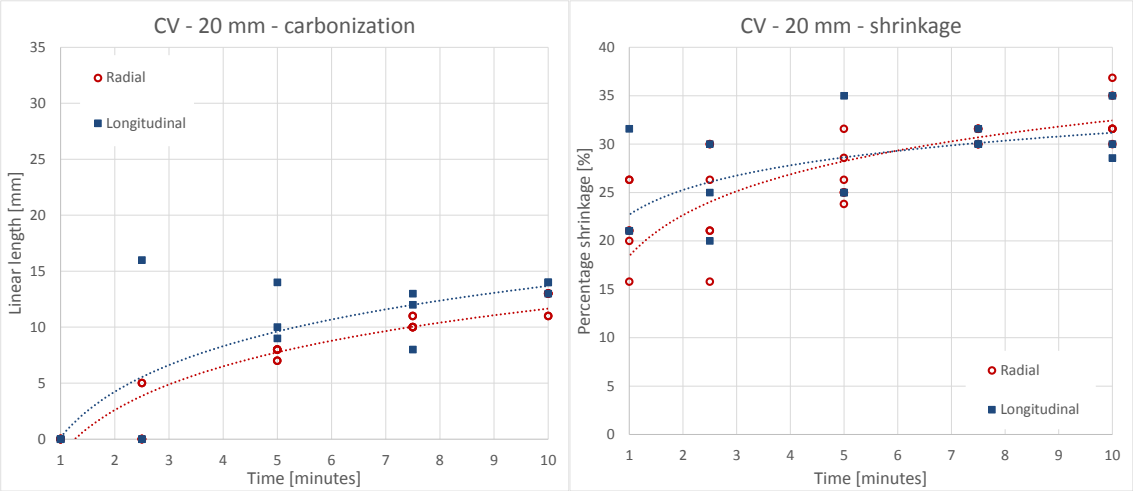

Figure 3.2.6 Shrinkage (left) and carbonization (right) trends as a function of time observed in cubes ablated with the Emprint ™ MTA system; direct comparison between radial (red) and longitudinal (blu) directions.

3.2.5 Shrinkage dynamics analysis

The analysis conducted during the model validation highlighted that the presence of carbonization, or its absence, substantially influences the shrinkage profile occurring through the tissue. The resultant shrinkage in the carbonized tissue was consistent and independent from the time of exposure. Once achieved complete carbonization of the entire tissue sample ablated with the MS and HS devices (i.e. in the cubes smaller than 20 mm side after 5 min of ablation; Figure 3.1.11), an average shrinkage in the range of 33 ± 8 % was observed without any further correlation with increasing time, as detailed in par. 3.2.2. Accordingly, shrinkage of 33 ± 2 % was observed in the cubes of tissue treated with the Emprint system that resulted completely carbonized, i.e. 20 mm side cubes after 10 min of ablation.

In the presence of carbonization, the shrinkage of the coagulated but not carbonized tissue appeared instead non-uniform with the distance from the antenna axis and correlated with the temperature increase as shown in Figure 3.2.7. The radial percentage shrinkage is reported as a function of the distance from the antenna axis, normalized to the initial sample size. Figure 3.2.7 reports the data of the experiments conducted with all the three considered devices for times of ablation longer than 5 min., i.e. in the cases where a substantial radial carbonization is obtained.

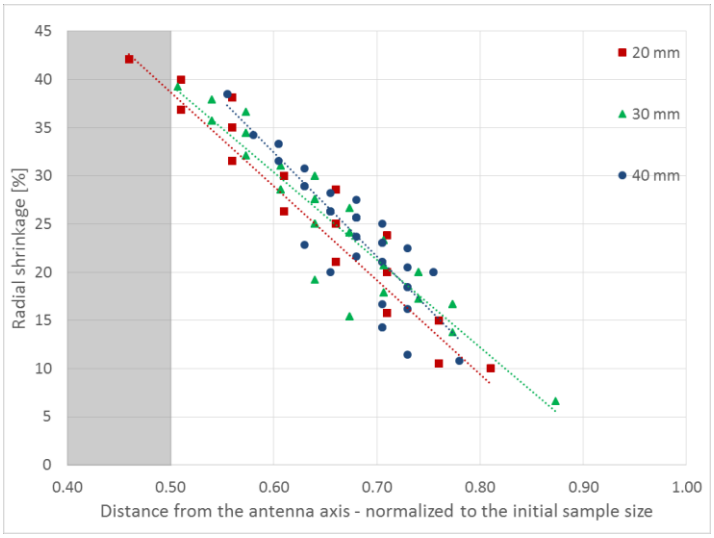

Figure 3.2.7 Percentage shrinkage, in presence of carbonization (grey area), as a function of the radial distance from the antenna axis. Data are normalized to the initial sample size for all 3 devices using samples ablated for 5, 7.5 and 10 min.

In the figure, a non-uniform linearly decreasing ($y = - 91.1 x + 84.6$, $R^2 > 0.87$) shrinkage is observed orthogonally to the antenna axis for increasing distances from the applicator. Beyond the carbonization margin, in the coagulated-but-not-carbonized tissue, the shrinkage consistently decreases with the tissue temperature to reach a minimum at the edge of the thermally ablated region where the tissue is exposed to temperature of approximately 55-60 °C (Lopresto *et al.,* 2014). A maximum shrinkage of 39 ± 3 % is observed at the margin of the carbonized region, where the heating is directly caused by the electromagnetic energy deposition and very high temperatures are reached; and a minimum shrinkage of 14 ± 3 % is evaluated at the periphery of the ablated area. Accordingly, the shrinkage occurring in the tissue strictly correlates to the physical status of the tissue and its temperature. In the carbonized tissue, i.e. above 100 °C, the shrinkage appears as a static phenomenon; whereas in the coagulated tissue, i.e. where the tissue temperature is higher than 55-60 °C but lower than 100 °C, the shrinkage manifests as a progressive process from the maximum observed in the charred tissue to the minimum observed at the edge between the coagulated region and untreated tissue.

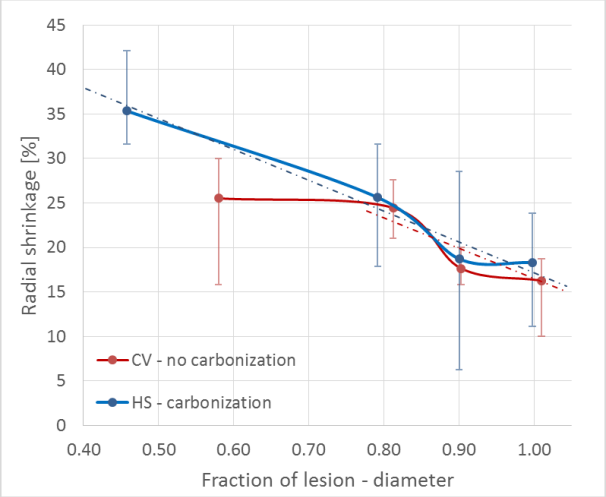

Figure 3.2.8 Percentage shrinkage as a function of the radial distance from the antenna axis normalized to the ablated area in the presence (HS) or absence (CV) of carbonization. Samples were ablated for 1 and 2.5 min.

Figure 3.2.8 depicts the radial percentage shrinkage as a function of the increasing radial distance from the radiating antenna, normalized to the radial extension of the ablated tissue. Cubes ablated for less than 5 min with the Amica (HS) and Emprint (CV) systems are analyzed to compare the shrinkage dynamics of the coagulated tissue in presence of carbonization with that observed in absence of carbonization. The Acculis data are not used in this analysis since they showed high variability in outcomes with respect to the other two systems. Emprint does not induce carbonization for time of ablation shorter than 5 min, thus these data are chosen as representative of the shrinkage in absence of carbonization; accordingly, Amica induces carbonization for time of ablation shorter than 5 min, thus these data are chosen as representative of the shrinkage in presence of carbonization. A difference in the shrinkage of the tissue close to the antenna axis is pointed out. In presence of a carbonization greater than 10% of the whole ablated area extension (i.e. the Amica case), tissues close to the carbonized region shrink of 35 ± 4 %; then contraction decreases linearly as a function of the increasing distance from the antenna axis up to a 20% shrinkage in the periphery of the ablated zone ($y = -34.7x + 51.8$, $R2 = 0.57$). On the contrary, in absence of carbonization (i.e. the Emprint case < 5 min), shrinkage of 25 ± 5 %, lower than the maximum induced by the Amica system (35 %), is measured for most (80%) of the tissue in radial direction. Nonetheless, farther from the antenna, decreasing amounts of shrinkage converging on the Amica trend are observed for the Emprint case; so that, very close values are obtained for the two devices

considering the whole thermally ablated area. The lack of carbonization during the first minutes of heating (< 5 min) is likely linked to the different cooling system implemented in the Emprint applicators that allows the cooling liquid reaching the antenna tip, thus preventing the early overheating of the tissue close to the antenna axis and its carbonization. It follows that different technologies can influence the appearance of carbonization, as in particular it can be evidenced that the performance of the cooling system plays a dominant role.

Therefore, although no device dependence is noted for the shrinkage in the coagulated-but-not-carbonized tissue in presence of carbonization (Figure 3.2.7); in absence of carbonization, a different behavior, possibly due to the different cooling technologies, is observed in the coagulated-but-not-carbonized tissue zone (Figure 3.2.8).

3.3 CT monitored experiments

MTA ablations were conducted on unrestricted specimens of *ex vivo* liver tissue (N=12) radiating 60 W for 10 min with the Amica device under CT-scanning in real-time. Spherical lead markers and fiber-optic sensors were placed in ad hoc positions into the tissue surrounding the MTA antenna. The experimental study was proposed to investigate the changes occurring in the thermally ablated tissue tracking the markers' movements and thus the tissue contraction, the temperature variations and the density estimated from the measured HU values. The experiments enabled to dynamically follow the tissue variations induced by the MTA procedure (Farina *et al*., 2013, 2014b, 2014c, Lopresto *et al*., 2015, Farina *et al*., 2015b, Minosse *et al*., 2016, Farina *et al.,* 2016b).

3.3.1 Thermally ablated area

At the end of each experiment, the ablated specimens were sectioned to directly collect data related to the thermally ablated area. The thermal lesion showed the typical ellipsoidal shape along the longitudinal section, with an arrow-shaped central carbonized area surrounded by a region of white coagulated tissue; and a cylindrical symmetry of the thermal lesion along the transverse section (Figure 3.3.1).

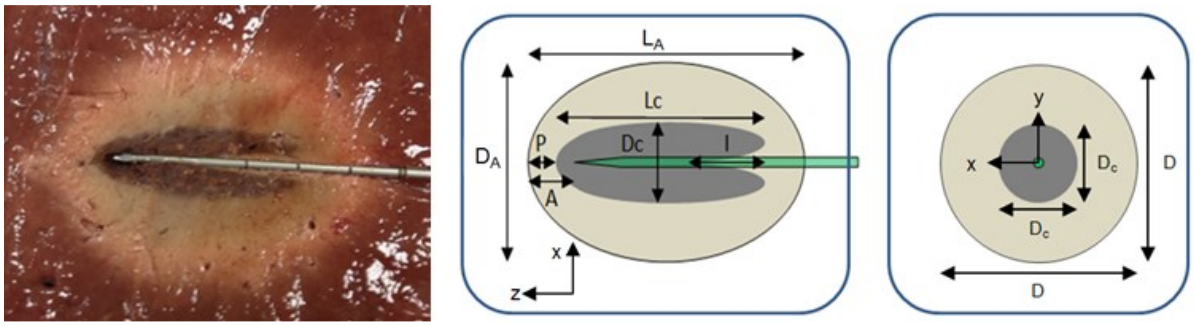

Figure 3.3.1 Appearance of the thermally ablated area induced by the MTA procedure (60 W, 10 min); and schematic representation of the zone of ablation. The origin of the coordinate system in is in correspondence of the antenna's tip. The central zone is the carbonized region (darker color) surrounded by the white coagulated area (lighter color) and externally by the untreated tissue; regions are evidenced, along with their characteristic geometrical dimensions.

The characteristic dimensions of the zone of ablation are reported in Table 3.3.1, following the notation illustrated in Figure 3.3.1, for each experimental trial. In the table, each experiment is characterized by the date in which the experiment was performed and the trial number. The experimental setup used (M = markers, T = temperature sensors) is also reported as well as the average dimensions (and standard deviations) of the obtained ablated areas. Although the variability is acceptable, in the following analyses the comparison with the estimated dimensions of the thermally ablated area will be performed on a trial-basis. It is worth noting that in the last marker-experiment (20150304_E4) the ablation treatment lasted only 7 min due to an unexpected rise of the impedance detected by the device for a possible breakdown of the antenna. Moreover, as reported in the table, ablated and carbonized area dimensions were not measured for one of the experiments conducted (20150225_E1), since an irregular structure of the main piece of tissue was found below the antenna insertion path, and any attempt to expose the ablated area resulted not successful. Accordingly, the abovementioned experiments are not considered in the following data analyses.

Table 3.3.1 Characteristic dimensions of the zone of ablation along with net power supplied to the MTA antenna; the experimental setup adopted is indicated (M = marker setup, T = temperature setup).

Date	*Trial*	*Setup*	L_A *[mm]*	D_A *[mm]*	L_C *[mm]*	D_C *[mm]*	*I [mm]*	*P [mm]*	*A [mm]*
17.12.2014	***E1***	***M & T***	60	45	40	14	17	8	10
	E2	***M & T***	57	42	38	14	14	3	4
	E3	***M & T***	61	38	37	14	13	5	8
18.02.2015	***E2***	***T***	58	42	32	10	11	7	8
	E4	***T***	56	44	40	10	18	7	8
	E6	***T***	63	37	38	10	12	10	10
25.02.2015	***E1***	***M***	-	-	-	-	-	-	-
	E2	***M***	59	38	32	10	10	6	8
	E3	***T***	55	38	32	9	9	7	7
04.03.2015	***E1***	***M***	50	36	24	11	10	5	7
	E2	***T***	55	34	34	8	10	6	7
	E3	***T***	60	38	33	11	10	12	13
	E4*	***M***	35	44	26	8	4	6	6
Average values			55 ± 8	40 ± 4	34 ± 5	11 ± 2	12 ±4	6 ± 2	8 ± 2

** 7 minutes trial – excluded from the evaluation of the average values*

3.3.2 Markers' kinetics

The movements and changes of the tissue heated with a 14G interstitial MiW antenna were analyzed exploiting the fiducials markers positioned into the target at different radial distances from the antenna axis and at three different longitudinal distances from the antenna tip, namely next to the antenna tip itself, to the antenna feed and to the antenna choke, as sketched in Figure 3.3.2. Data collected elaborating the CT images allowed identifying the position of the fiducials (N=93 through 6 different experiments) placed into the tissue every 29 seconds during the ablation procedure and during the consecutive 5 minutes. In most of the cases, the nominal positions of lead markers into the tissue specimen were not guaranteed possibly because of an elastic counter-reaction of the tissue after retrieving the catheters used to guide the beads insertions. However, thanks to the analysis of the collected CT images, during the post-processing phase, the markers' positions were univocally identified at the different times of the scans. Tissue modifications were investigated looking at the markers' movements during the procedure as well as at the final markers' displacement.

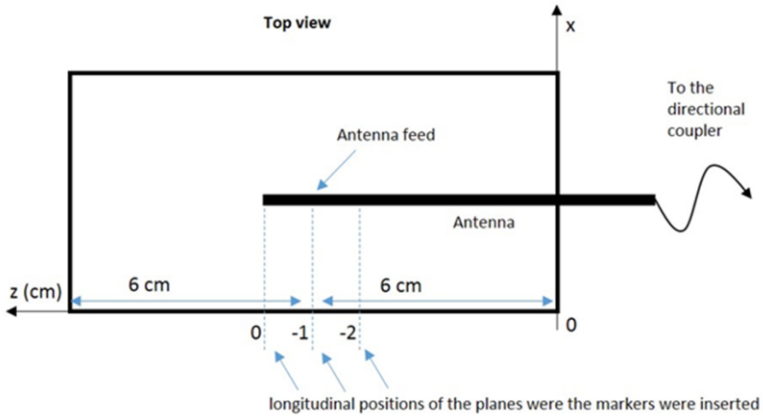

Figure 3.3.2 Schematic of the markers' longitudinal positioning into the biological tissue with respect to the radiating antenna.

In Figure 3.3.3, the different markers' positons over time are reported for one of the experiments conducted (20150225_E2) as an example. Markers are displayed on the plane orthogonal to the antenna axis independently of their longitudinal position. Each marker is numbered and represented by "x" when moving toward the antenna axis and by filled "o" when moving away from the antenna axis. Markers' movements result heterogeneous and non-uniform, pointing out a rotational trajectory as a function of the time, with neighbor markers showing similar behaviors over the time. To better analyze these complex rotational movements, markers are grouped by elements showing similar behavior over time in the three spatial directions. In Figure 3.3.4, the radial trajectories over time of markers moving away from the antenna axis are graphed: in the left panel, fiducials "m8", "m13" and "m14", showing a longitudinal displacement of 3 mm in the opposite direction to the antenna tip, are reported; whereas, fiducials "m3", "m4" and "m11", showing a longitudinal displacement of 6 mm toward the antenna tip, are reported in the right panel. Within the same group, markers belonging to different traversal planes are considered: those identified by "x" concern fiducials at the antenna feed (about 10 mm along the z axis), whereas the "o" marked relate to fiducials distant 20 mm from the antenna tip, at the beginning of the procedure. It is interesting to observe that markers reported in Figure 3.3.4 (left), positioned above the antenna in Figure 3.3.3 (i.e. x-coordinate > 0), are subject to an expansion phenomenon until the end of the ablation procedure (about 600 s), and then they collapse. It could be surmised that

these markers are pushed from the gas dissipated during the heating procedure, and then they collapse due to the gravity. A similar behavior is presumable also for markers "m7", "m9", and "m15" looking at their trajectories in Figure 3.3.3. On the other hand, in Figure 3.3.4 (right), markers "m3", "m4", and "m11" positioned below the antenna axis show an expanding trend during the heating as in the case of "m8", "m13" and "m14", although without collapsing toward the antenna axis at the end of the procedure.

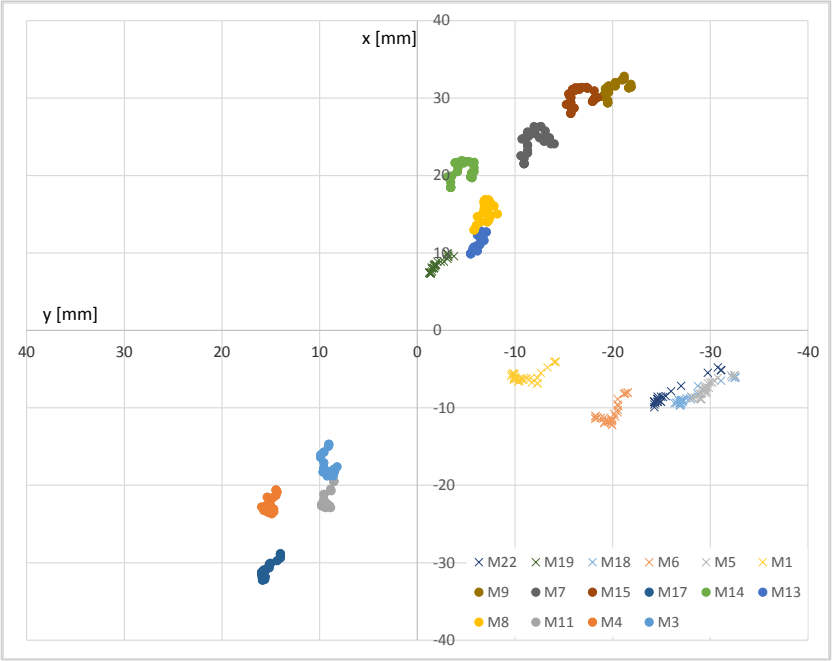

Figure 3.3.3 2D visualization of the markers' displacements in the planes orthogonal to the antenna axis: evolution as a function of time – trial M5. "x" dots indicate markers moving toward the antenna axis, while "o" filled dots indicate markers moving away from the antenna axis.

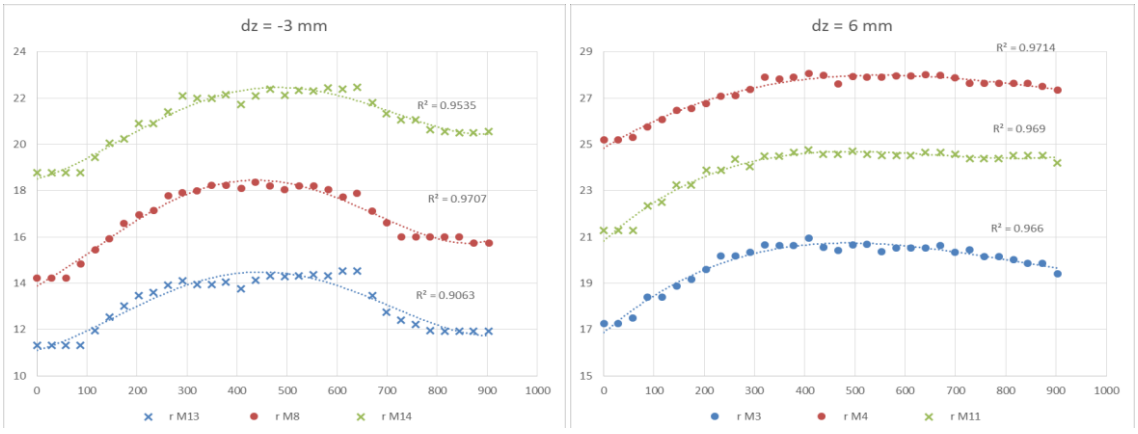

Figure 3.3.4 Radial markers' trends as a function of time: two groups of neighbor markers.

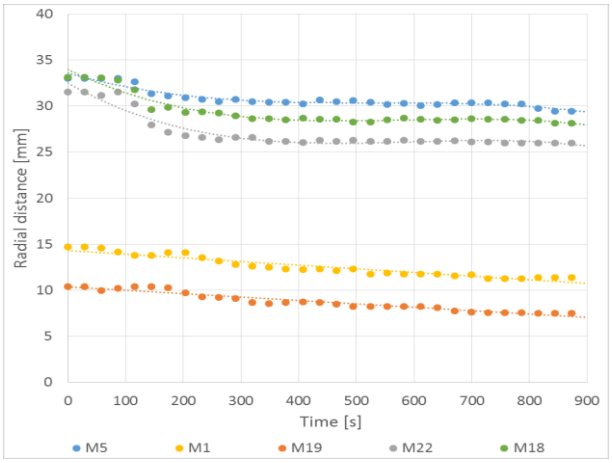

Figure 3.3.5 Radial markers' trends as a function of time: markers moving toward the antenna axis.

In Figure 3.3.5, the radial trajectories over time of markers moving toward the antenna axis thus representative of a contraction phenomenon are reported. In this case, it is possible to note that markers at the same initial radial distance from the radiating source show similar trends independently from their longitudinal position. In particular, "m5", "m18", and "m22", at about 33 mm from the antenna axis at t = 0 s, show a drop in their radial distance from the antenna axis after less than two minutes of ablation continuing decreasing afterword. Markers "m1" and "m19", closer to the antenna axis at t = 0 s, show an uniform linear decrease of their radial distance during and after the ablation ($y = -0.004\ x + q$, where q is the radial distance value at t = 0 s, $R^2 > 0.9$).

Thus, the movements of the tissue during a MTA procedure result complex and heterogeneous. To focus the analysis of the shrinkage, the total markers' displacement at the end of the ablation procedure is considered. Comparing the positions collected at the beginning (t = 0 s) and at the end of the monitoring (t = 900 s) for each marker (it is useful to recall here that the MTA procedure lasted 10 min – 600 s, while the CT scans were taken for 15 min – 900 s), vectors representative of the movement directions are obtained. The analysis is conducted looking at the radial displacement in the transverse plane, i.e. radially to the antenna axis, and at the longitudinal displacement along the axial direction, exploiting the cylindrical symmetry of the experimental setup. As an example, the displacements observed in the experiment 20150304_E1 are graphed in Figure 3.3.6 (top row). On the right side of the figure, the longitudinal displacement is reported: the three different planes on which markers were placed along the z axis are observable. Markers

showing a positive displacement, i.e. representative of a tissue shrinkage, and markers with negative or no displacement are visible. In the second row of Figure 3.3.6, the only markers (N=42) subject of the following analyses, i.e. representative of the tissue shrinkage, are reported, excluding markers showing no significant displacements and/or moving away from the antenna axis over the time. Radial displacements smaller than 1.5 mm and longitudinal displacements smaller than 2.5 mm were not accounted, considering the minimum significant displacement equal to two times the CT spatial resolution of the scan routine adopted, being $dx = dy \approx 0.5$ mm, then $dr = \sqrt{dx^2 + dy^2} \approx 0.7$, $dz = 1.25$ mm.

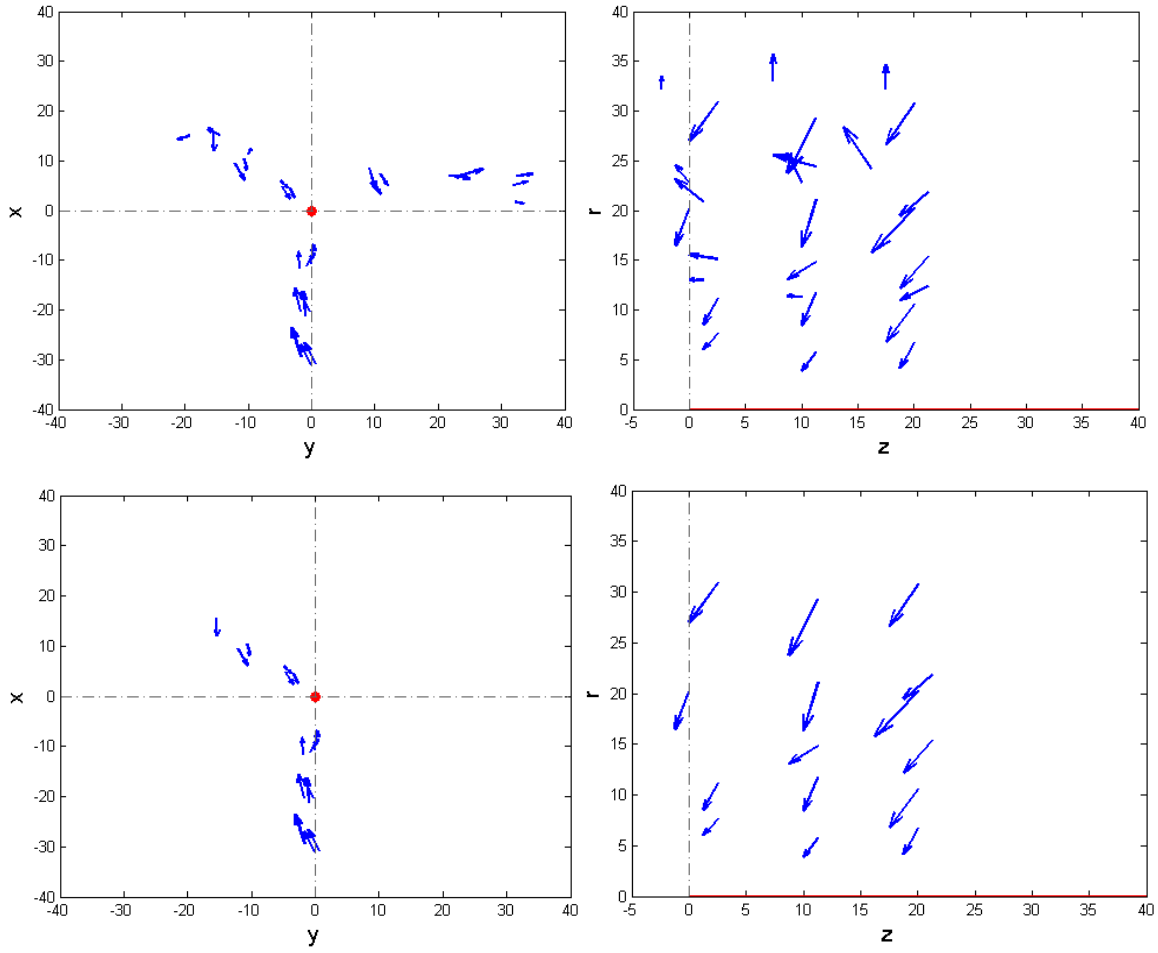

Figure 3.3.6 Representation of the markers' displacement: the arrow starting point identifies the marker's position at t = 0 s, while the arrowhead identifies the marker's position at t = 900 s. Left panels depict the transverse plane, i.e. the plane orthogonal to the antenna axis; Right panels depict the longitudinal plane, i.e. the plane containing the antenna axis. In the top row all the markers are reported, whereas in the bottom row only shrinking markers are shown.

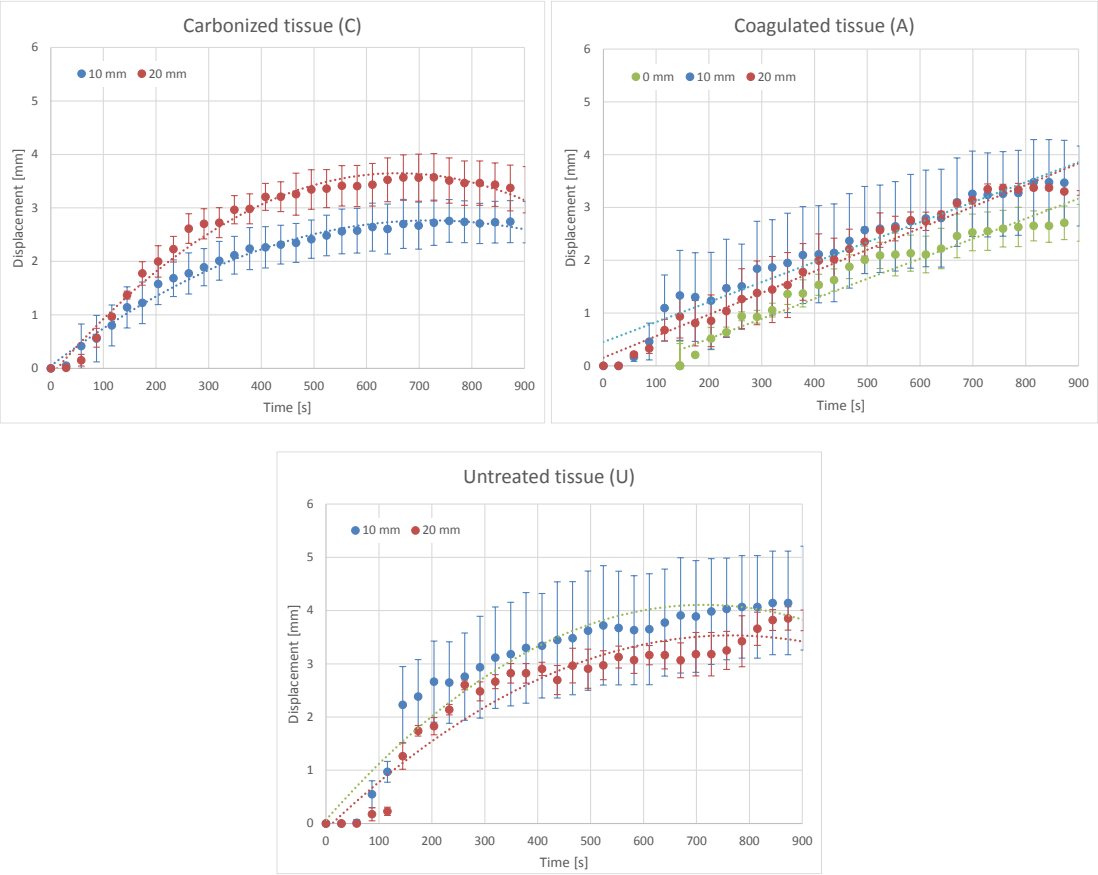

Figure 3.3.7 Radial displacement as a function of time of markers representative of tissue shrinkage: analysis based on the tissue status and the three different planes orthogonal to the antenna axis containing the fiducials markers.

In Figure 3.3.7, a cluster analysis of the markers representative of the tissue shrinkage in the different zones of the tissue surrounding the radiating antenna is reported, pooling markers in homogenous groups based on their radial and longitudinal positions at the end of the procedure. For each plane, i.e. the antenna tip plane (z = 0 mm), the antenna feed plane (z = 10 mm), and the antenna choke plane (z = 20 mm), data are grouped depending on their belonging to the different regions of the thermally ablated area (carbonized – C, coagulated – A, untreated – U). The data point out increasing trends of the markers' radial displacement as a function of time, confirming a shrinkage phenomenon. Although no statistically significant differences (t-test with $p > 0.05$) are observed between the different zones of the ablated area and among the different z-planes, the obtained trends lead to some considerations. In the carbonized tissue (C), it is possible to observe a steep increase of the fiducials' displacement until reaching a plateau of about 3 mm; such

displacement visibly decreases when the power is switched off, i.e. after about 600 s, for z = 10 mm, whereas after about 400 s of ablation, i.e. during the procedure, for z = 20 mm. In the only coagulated tissue (A) instead, a linearly increasing trend is observed, not halting at the end of the ablation procedure: the same linear trend is observed at the antenna feed and at the choke level ($y=0.004\ x + 0.122$, $R^2 = 0.97$), whereas at the tip the tissue starts shrinking with a time delay of about 2 minutes being characterized from an initial expansion phase. The untreated tissue shrinks following the trend observed in the thermally ablated area, pointing out the influence of the carbonization trend (the same slope was observed within the first minutes), but not halting when the power is switched off. The observed trends confirm that the greatest contribute to the shrinkage phenomenon is due to the charred tissue, and that out of the carbonized tissue, the heating process, and consequently the correlated tissue modification, does not end when the active heating stops.

3.3.2.1 Model punctual validation

In order to validate the predictive model proposed for the shrinkage evaluation, markers showing a reduction in their distance from the antenna axis (as in the example of second row of Figure 3.3.6) were considered and the analytical model applied. Each marker was identified based on its belonging to the different region of the thermally ablated area (carbonized, coagulated, untreated), comparing its final position with the values of Table 3.3.1. The initial position for each marker was predicted starting from the final position, adopting the shrinkage factors proposed in eqq (3.1) and (3.2), and applying the model of eqq (3.3) and (3.4). R and L represent the initial distances i.e. t = 0 s, while r and ℓ represent the final distance (t = 900 s), following the notation illustrated in par. *3.2.1*. To apply the model to the markers displacement, four scenarios were considered:

i. Marker in the carbonized region, i.e. r < rC

$$R = \frac{r}{\alpha_{C,D}} \tag{3.5a}$$

$$L = \frac{\ell}{\alpha_{C,L}} \quad \text{if } r \ll rC \tag{3.5b}$$

$$L = \frac{\ell}{\alpha_{A}} \quad \text{if } r \sim rC \tag{3.5c}$$

ii. Marker in the coagulated region, i.e. rC < r < rN

$$R = \frac{r_C}{\alpha_{C,D}} + \frac{r - r_C}{\alpha_A} \tag{3.6a}$$

$$L = \frac{\ell}{\alpha_A} \tag{3.6b}$$

iii. Marker in the untreated region, i.e. r > rN

$$R = \frac{r_C}{\alpha_{C,D}} + \frac{r_A}{\alpha_A} + (r - r_N) \tag{3.7a}$$

$$L = \frac{\ell}{\alpha_A} \tag{3.7b}$$

iv. Marker initially placed around the antenna tip, i.e. |L| < 2.5

$$R = \frac{r}{\alpha_A} \tag{3.8a}$$

$$L = \frac{\ell}{\alpha_A} \tag{3.8b}$$

It should be noted that for the carbonized area two different regions were considered: one is the proper carbonized region in which the markers' movement is modeled by eqq. (3.5a) and (3.5b); and the other one, representative of the transition zone between the charred and the coagulated tissue, in which the markers' movement is modeled by eqq. (3.5a) and (3.5c). In this zone, the tissue contraction is completely ruled by the carbonization shrinkage radially, whereas longitudinally is primarily influenced by the coagulated tissue shrinkage.

The model was applied to the markers' data collected from the CT images of the six experiments involving markers, knowing the extension of the thermally ablated area at the end of the MTA treatment. It should be notice here that the model was applied also to the data of experiment of 04.03.2015, which ran only for 7 min (about 420 s). The average errors evaluated applying the model to each marker are reported below. In the tables, the initial (R_{meas} and L_{meas}) and final marker's positions (r and ℓ) are reported, as well as the initial position estimated applying the model (R and L). The observed error is reported:

i. Markers in the carbonized region, i.e. r < rC

Table 3.3.2 Model applied to the markers in the carbonized region.

exp	r [mm]	ℓ [mm]	R [mm]	L=ℓ/$\alpha_{C,L}$ [mm]	L=ℓ/α_A [mm]	R_{meas} [mm]	L_{meas} [mm]	errR [mm]	errL [mm]
20141217_E1_m4	5.3	17.5	7.7			8.2	15.0	0.4	n.s.
20141217_E2_m2	5.5	10.0	7.9			9.0	8.8	1.1	n.s.
20141217_E3_m3	3.4	10.0	5.0			5.1	12.5	0.1	n.s.
20150304_E1_m7	4.2	18.8	6.0			6.8	20.0	0.7	n.s.
20150304_E1_m13	3.9	10.0	5.6			5.7	11.3	0.1	n.s.
20141217_E1_m3	8.5	18.8	12.4			12.9	16.3	0.5	n.s.
20141217_E2_m4	8.2	10.0	11.8			11.2	7.5	0.6	n.s.
20141217_E3_m2	6.8	10.0	9.8			9.8	12.5	0.0	n.s.
20150304_E1_m6	6.8	17.5	9.9			10.6	20.0	0.7	n.s.
							Average	0.5	-
							Min	0.0	-
							Max	1.1	-

n.s. = not significant displacement

ii. Marker in the coagulated region, i.e. rC < r < rN

Table 3.3.3 Model applied to the markers in the coagulated region.

exp	r [mm]	ℓ [mm]	R [mm]	L [mm]	R_{meas} [mm]	L_{meas} [mm]	errR [mm]	errL [mm]
20141217_E1_m2	18.7	20.0	23.5		22.1	16.3	1.4	L < ℓ
20141217_E3_m1	14.5	10.0	18.6		18.2	12.5	0.4	n.s.
20150225_E2_m1	11.4	17.5	14.5		14.7	20.0	0.2	n.s.
20150304_E1_m2	12.2	18.8	15.6		15.4	21.3	0.2	n.s.
20150304_E1_m5	15.8	16.3	19.7	18.5	20.2	20.0	0.5	1.5
20150304_E1_m11	16.3	10.0	20.3		21.1	11.3	0.8	n.s.
20150304_E1_m12	8.5	10.0	11.3		11.7	11.3	0.4	n.s.
20150304_E1_m14	13.1	8.8	16.6		14.9	11.3	1.8	n.s.
20150304_E4_m5	16.1	17.5	19.5	19.9	20.0	21.3	0.5	1.4
20150304_E4_m8	6.8	18.8	8.9		8.7	20.0	0.2	n.s.
20150304_E4_m9	11.8	17.5	14.6		13.9	17.5	0.7	n.s.
20150304_E4_m14	17.2	8.8	20.8		19.5	11.3	1.4	n.s.
20150304_E4_m16	8.7	8.8	11.1		10.2	10.0	0.9	n.s.
20150304_E4_m17	8.2	8.8	10.6		9.7	8.8	0.9	n.s.
20150304_E4_m19	9.5	8.8	12.1	9.9	11.3	6.3	0.8	L < ℓ
					Average		0.7	1.4
					Min		0.1	1.4
					Max		1.8	1.5

n.s. = not significant displacement; L< ℓ = expansion

iii. Marker in the untreated region, i.e. r > rN

Table 3.3.4 Model applied to the markers in the untreated region.

exp	r [mm]	ℓ [mm]	R [mm]	L= [mm]	R_{meas} [mm]	L_{meas} [mm]	errR [mm]	errL [mm]
20141217_E3_m4	29.9	10.0	34.7		31.9	11.3	2.8	n.s.
20150225_E2_m5	29.4	16.3	33.6		33.0	18.8	0.6	n.s.
20150225_E2_m6	21.3	16.3	25.5		23.0	18.8	2.5	n.s.
20150225_E2_m18	28.0	6.3	32.1		33.1	7.5	1.0	n.s.
20150304_E1_m3	19.5	18.8	23.7		21.9	21.3	1.8	n.s.
20150304_E1_m4	26.7	17.5	30.9		30.8	20.0	0.1	n.s.
20150304_E1_m10	23.8	8.8	28.0		29.3	11.3	1.3	n.s.
20150304_E4_m4	23.3	18.8	27.5	21.3	29.2	23.8	1.7	2.4
20150304_E4_m13	28.7	8.8	33.0		31.0	11.3	2.0	n.s.
					Average		1.5	2.4
					Min		0.1	-
					Max		2.8	-

n.s. = not significant displacement; L< ℓ = expansion

iv. Marker initially placed around the antenna tip, i.e. |L| < 2.5

Table 3.3.5 Model applied to the markers surrounding the antenna tip.

exp	r [mm]	ℓ [mm]	R [mm]	L= [mm]	R_{meas} [mm]	L_{meas} [mm]	errR [mm]	errL [mm]
20150225_E2_m19	7.5	3.8	8.5	4.3	10.4	1.3	1.9	L < ℓ
20150225_E2_m22	26.0	-1.3	29.5	-1.4	31.5	-1.3	2.0	n.s.
20150304_E1_m19	27.1	0.0	30.8	0.0	31.0	2.5	0.2	n.s.
20150304_E1_m20	8.6	1.3	9.7	1.4	11.2	2.5	1.5	n.s.
20150304_E1_m21	6.1	1.3	6.9	1.4	7.7	2.5	0.8	n.s.
20150304_E1_m25	16.5	-1.3	18.8	-1.4	20.2	0.0	1.4	n.s.
20150304_E4_m22	15.4	1.3	17.5	1.4	18.0	1.3	0.5	n.s.
20150304_E4_m23	8.2	1.3	9.3	1.4	10.3	1.3	1.0	n.s.
20150304_E4_m24	26.0	0.0	29.5	0.0	28.4	0.0	1.1	n.s.
					Average		1.2	-
					Min		0.2	-
					Max		2.0	-

n.s. = not significant displacement; L< ℓ = expansion

Considering that out of the carbonized region the model uses two experimental data (and their difference) collected with rulers with an accuracy of 1 mm, it is possible to state that the model is

validated up to an error of 3 mm. In the tables above, an error lower than 3 mm is pointed out and the model results able to predict the initial position of the markers in 100% of the considered cases. Accordingly, the results of the analysis confirm the ability of the model to predict the radial amount of shrinkage occurring at different distances from the radiating source. In the longitudinal direction, the observed displacements resulted smaller than the minimum significant value considered due to the spatial resolution of the CT protocol adopted (i.e. L- $\ell > 2.5$ mm) in the 88% of the considered cases, thus it was not possible longitudinally validate the model.

3.3.3 Temperature variation analysis

The temperature increase of the tissue treated with MTA was monitored exploiting the fiber-optic temperature sensors placed into the target at different radial distances from the antenna feed: at 10, 20 and 30 mm for all the experiments, with the exception of the first experiment conducted (20141217_E1) where a forth sensor was placed at 5 mm radially to the radiating source. The temperature data were collected every 10 s and stored; whereas, thanks to a dedicated MATLAB script, the exact position of the sensors was identified in post-processing on the CT images collected during the ablation procedure and during the consecutive 5 minutes. Possible variations in the sensors' positioning during the heating procedure were investigated: since they were within the accuracy of the collected data, the sensors' position evaluated at t = 0 s was considered constant all along the procedure. It is worth noting that for the three experiments of 17.12.2014 (20141217_E1, 20141217_E2, 20141217_E3), the sensors' positions were not accurately evaluable from the images elaboration due to the high scattering introduced from the lead markers placed close to them. Therefore, from these trials only the data linked to the 5 mm radial position will be taken into account, since at a visual inspection the sensor was identified inside the carbonized region at the end of the MTA procedure.

For the data analysis, the temperature data were pooled based on their relative position into the tissue with respect to the tissue status at the end of the procedure. Five groups were identified corresponding to five different regions:

i. sensors into the carbonized region (C);
ii. sensors into the coagulated region (A), positioned in a range of 1-7 mm from the end of the carbonized tissue (A – closer to C);

iii. sensors into the coagulated region, positioned in a range of 7-15 mm from the end of the carbonized tissue, i.e. at 2-7 mm from the edge of the thermally ablated area with the untreated (U) tissue (A – closer to U);

iv. sensors at the edge of the thermally ablated area, i.e. characterized with a radial distance from the antenna axis equal (± 2 mm) to the radial dimension of the ablated region (A edge);

v. sensors out of the ablated region positioned into the untreated tissue (U), up to 10 mm far from the edge of the thermally ablated area.

In Figure 3.3.8, average values are graphed as a function of time with their standard deviation with the only exception of the data related to the carbonized region (group i – black dots) accounting only one sensor (20141217_E1). Further analysis into the charred tissue were not performed because of the risk of damaging the sensor. The graph points out the different thermal trends observable over time at different radial distances from the radiating source. In particular, it is possible to notice that, once the direct heating stops (600 s on the x-axis), the temperature decreases steeply inside the thermally ablated area (maroon and orange dots), and smoothly at the edge of the ablated area (yellow dots); whereas outside, in the untreated tissue (green dots), the temperature keeps on increasing. Indeed, the heat deposited in the tissue closer to the antenna feed moves to the zones at lower temperature by thermal conduction. Out of the thermally ablated area ("U" data of Figure 3.3.8), a temperature increase up to 5 °C is observable up to 10 mm from the thermally ablated area edge, during the minutes following the power switch off.

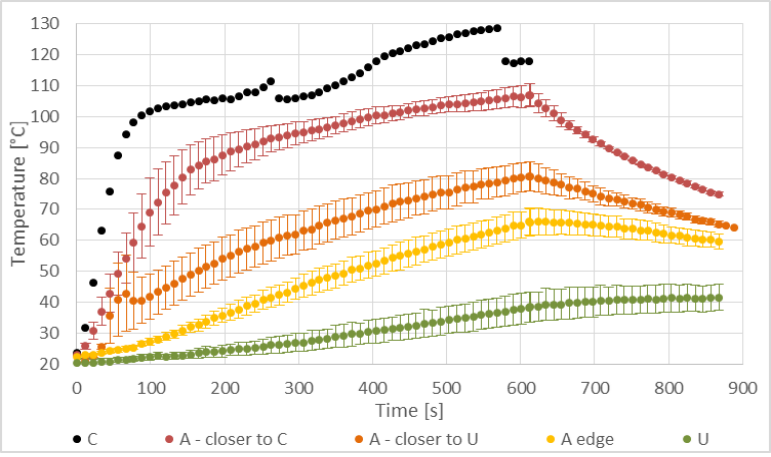

Figure 3.3.8 Tissue temperature as a function of the time of ablation.

Figure 3.3.9 illustrates the tissue temperature as a function of the radial distance of the temperature sensors from the antenna axis for different time instants: the sensors' radial position is normalized to the dimension of the thermally ablated area obtained in order to pool the fiber optic data considering their relative position into the different regions of the target tissue. Therefore, on the x-axis the value 1 represent the edge of the coagulated area, while at 0.26 the edge of the carbonized tissue is highlighted, since the ratio between the carbonized radius and the ablated radius was calculated to be 0.26 ± 0.03 over 6 experimental induced lesions; values higher than 1 refer to the untreated tissue. Average values are reported with their standard deviation. Two different graphs are proposed, one illustrating the temperature variation during the heating process (Figure 3.3.9 left), the other focusing on the temperature trends after the power was switched off (Figure 3.3.9 right). Into the carbonized region, temperatures up to 128 °C are observed, and the carbonized tissue corresponds to tissue temperatures above 110 °C; it is possible to note indeed that where the sensors measured 100 °C the tissue did not carbonized yet even if that temperature was kept for up to 3 minutes (pink dot – 7 min – to the black one – 10 min). Into the coagulated region, surrounding the charred ones, it is possible to observe a linear decreasing trend (e.g., $y = -76 x + 122$, $R2 > 0.99$ at 5 min) from the value corresponding to the charred tissue to that measured in the untreated tissue. It is worth recalling here that spatially analyzing the shrinkage data obtained with the cubes-experiments (par. *3.2.5*) a linear decrease was observed for the shrinkage ($y = -91.1 x + 84.6$, $R^2 > 0.87$) as a function of the increasing distance from the antenna axis. At the edge of the coagulated area, the maximum temperature measured is 65 °C: thus, it is possible to say that once this temperature value is reached the tissue coagulation occurs, whereas 60 °C does not guarantee the presence of tissue coagulation. Out of the thermally ablated area, in the untreated tissue, it is possible to observe temperature values up to 50 °C closer to the coagulated tissue and up to 40 °C farer. During the cooling, i.e. in absence of the direct heating, while the temperature drops into the coagulated tissue, a moderate temperature increase is still appreciable in the untreated one. Thus, 50 °C results not enough to induce tissue modifications perceptible to a visual inspection.

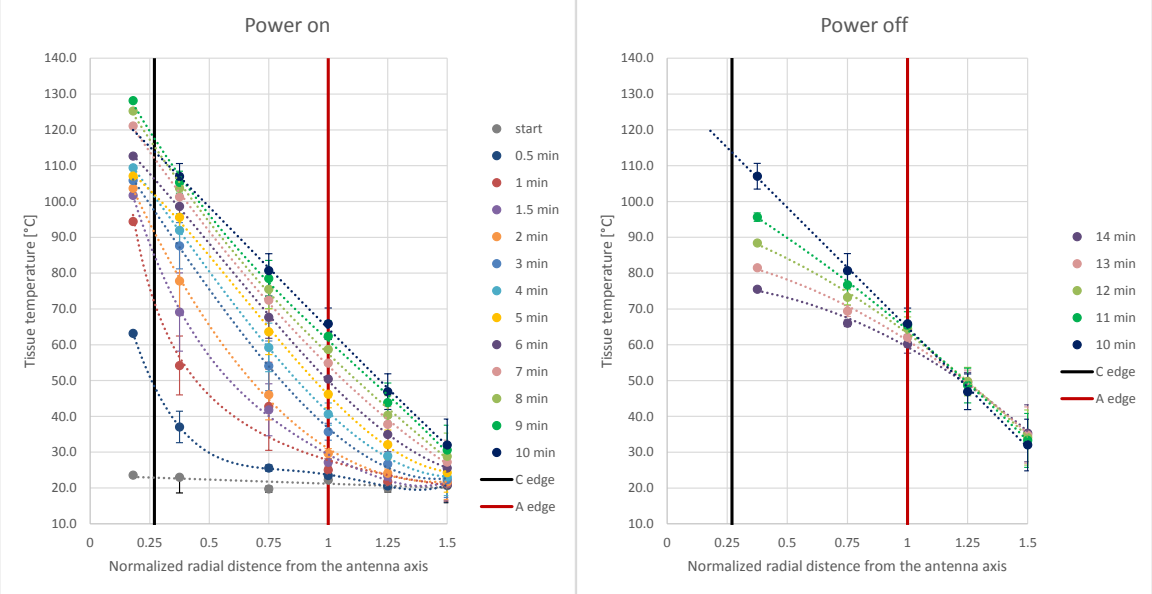

Figure 3.3.9 Tissue temperature as a function of the distance from the antenna axis, normalized to the average dimension of the thermally ablated area at the end of the procedure.

3.3.4 Tissue density analysis

The CT-experiments allowed collecting data linked to the tissue density variation occurring in the tissue in real time, also. The CT images are indeed characterized of matrix of values (pixels) representative of the absorption coefficient of the tissue normalized to the water absorption coefficient, i.e. of the attenuation to which the x-rays were subject in their path through the tissue. These values are better known as Hounsfield Unit (HU) values, i.e. a measure of the tissue's density of the various scanned structures. Thanks to an ad hoc developed program, the collected images were analyzed and the pixel information extracted: experiments conducted with markers were excluded from this analysis since the fiducials introduce to high scattering not allowing a correct evaluation of the tissue density modifications. To correlate the tissue density with the physical status of the tissue, pixels' regions corresponding to the post-ablation regions of carbonized, coagulated and untreated tissue were considered: the corresponding average value with the minimum and maximum values calculated are reported in Table 3.3.6, Table 3.3.7 and Table 3.3.8. The obtained results are illustrated separately for the different experiments reporting

the values linked to two different time instants: the end of the ablation (t = 600 s) and the end of the experiment (t = 900 s). As a general rule, HU values lower than 800 have been excluded to avoid air gaps such as vessels; similarly HU higher than 1200 have been excluded from the analysis to eliminate the scattering induced by the highly reflective antenna. As a reference, the values observed into the tissue at the beginning of the ablation procedure are reported also. It is possible to observe no substantial variations in the range of values observed.

In the region corresponding to the carbonized tissue, a lower average values is observed at the end of the ablation procedure pointing out an expected variation in the tissue density. Indeed, the density variation observed results consistent with density measurements experimentally conducted on cubes of bovine liver completely charred as well as untreated. The volume and weight of the 20 mm side cubes' used in the experiments of par. *3.1.3* (a total of 10) were measured and the tissue density derived as 875 ± 75 kg/ m^3 for the charred tissue and as 1045 ± 130 kg/ m^3 for the untreated tissue, with a statistically significant difference between the two groups of data (p = 0.01). On the other hand, the data in the tables show that, in the same region where a density variation is observed, five minutes after the end of the ablation no substantial changes are reported with respect to the baseline value, especially looking at the range of the measured values. These results suggest that the values collected from the CT scans could be useful to evaluate variations into the tissue density and to identify the thermally ablated area, although they should be carefully considered and analyzed since the shown transitory reduction in the average value is probably highly influenced by the gas dissipated during the procedure.

Table 3.3.6 Pixels values evaluated in the untreated tissue at the beginning of the heating procedure (0 s), at its end (600 s) and after 5 minutes (900 s).

	Untreated – t = 0 s			**Untreated - t = 600 s**			**Untreated - t = 900 s**		
Trial	**Average**	**Min**	**Max**	**Average**	**Min**	**Max**	**Average**	**Min**	**Max**
20150218_E1	1113.6	809	1196	1083.0	810	1154	1086.0	810	1150
20150218_E4	1114.1	838	1199	1119.3	1078	1187	1115.1	1034	1175
20150218_E6	1116.2	834	1195	1083.4	805	1177	1090.1	846	1147
20150225_E3	1115.1	818	1193	1117.8	1034	1168	1113.1	956	1165
20150304_E2	1115.8	882	1179	1107.8	911	1179	1107.3	911	1162
20150304_E3	1109.3	836	1174	1092.5	812	1171	1104.8	810	1151
	1114.0	809	1199	1100.6	805	1187	1102.7	810	1175

Table 3.3.7 Pixels values evaluated in the coagulated region of the thermally ablated area at the beginning of the heating procedure (0 s), at its end (600 s) and after 5 minutes (900 s).

	Coagulated - t = 600 s			Coagulated - t = 900 s		
Trial	**Average**	**Min**	**Max**	**Average**	**Min**	**Max**
20150218_E1	972.3	814	1085	1031.2	832	1142
20150218_E4	926.4	805	1079	1056.5	841	1125
20150218_E6	1032.3	813	1115	1035.5	821	1133
20150225_E3	1000.6	811	1118	1065.3	909	1142
20150304_E2	1035.0	801	1088	1082.4	916	1146
20150304_E3	1063.3	833	1152	1093.5	1037	1193
	1005.0	801	1152	1060.7	821	1193

Table 3.3.8 Pixels values evaluated in the carbonized region of the thermally ablated area at the beginning of the heating procedure (0 s), at its end (600 s) and after 5 minutes (900 s).

	Carbonized - t = 600 s			Carbonized - t = 900 s		
Trial	**Average**	**Min**	**Max**	**Average**	**Min**	**Max**
20150218_E1	936.6	812	1107	1025.7	805	1173
20150218_E4	927.1	800	1109	1038.8	809	1172
20150218_E6	978.6	803	1147	1061.4	820	1194
20150225_E3	889.7	802	1015	1003.4	805	1164
20150304_E2	953.2	803	1082	1029.2	810	1175
20150304_E3	961.9	801	1188	1057.3	817	1178
	941.2	800	1188	1036.0	805	1194

3.4 Tissue's size and shape influence

3.4.1 Experimental analysis on thin samples of tissue

MTA ablations were conducted with the Amica device (HS Hospital Service SpA) on thin samples of *ex vivo* porcine liver tissue (t_i = 20 ± 5 mm height) with and without capsule radiating 60 W for 10 min (for a total of N = 12 experiments). The experimental study was proposed to investigate the influence of the tissue dimensions, in presence or absence of the capsule, on the shape and dimension of the thermally ablated area: the dimensions of the coagulated and carbonized regions were measured after each trial. The samples were cut along two orthogonal planes passing through the antenna axis: the sagittal plane, orthogonal to the work bench that

identify the less thick specimen's section (Figure 3.4.1 top), and the coronal plan, parallel to the work bench that identify the thicker specimen's section (Figure 4.3.1 center). The schematic representation used is that already presented in Figure 3.3.1, and here reported in Figure 3.4.1 (bottom) for easiness. In this study, the inflection of the carbonized area (I), the protrusion of the thermally ablated area (A) as well as the extension of the only coagulated tissue (P) beyond the antenna tip are investigated.

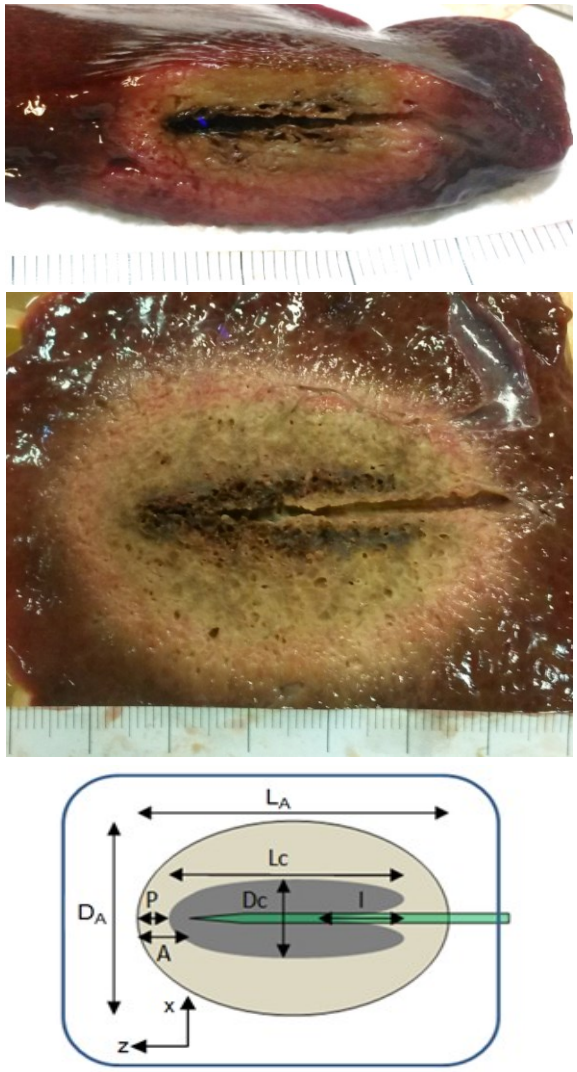

Figure 3.4.1 Appearance of the thermally ablated area induced in thin samples of ex vivo porcine liver tissue with capsule: section along the thin dimension (top left); section along the thicker dimension (top right); and schematic representation of the zone of ablation (bottom). The carbonized (darker color), coagulated (lighter color) and untreated tissue regions are evidenced, along with their characteristic geometrical dimensions.

As it is possible to note from Figure 3.4.1, the reduced thickness of the samples on the sagittal plane limits the extension of the ablated region. To evaluate the possible influence of this limitation, a statistical analysis (t-test) was conducted comparing the dimensions measured on the coronal plane in the thin samples without (Table 3.4.1) and with capsule (Table 3.4.2) with those measured in the experiments conducted on unrestricted samples of ex vivo bovine liver with the Amica device for 10 min at 60 W. The comparison was performed also between the thin samples with and without capsule (Table 3.4.3).

Table 3.4.1 Comparison between the dimensions of the thermally ablated area induced in unrestricted samples of tissue (bulk) and in thin samples without capsule radiating 60 W for 10 min with the Amica MTA system. Average values (Avg ± st. dev.) and statistical difference evaluated between the two groups of date (p-value) are reported.

	L_A		D_A		L_C		D_C		I		P		A	
	bulk	**thin**	**bulk**	**thin**	**bulk**	**thin**	**bulk**	**thin**	**bulk**	**thin**	**bulk**	**thin**	**bulk**	**thin**
Avg	57.6	55.0	39.3	36.5	34.5	36.2	11.0	9.5	12.2	15.5	6.9	5.8	8.2	8.3
St. dev	3.6	1.9	3.5	3.4	4.7	1.5	2.1	1.0	3.0	2.8	2.5	1.8	2.3	1.7
p-value	0.12		0.13		0.43		0.12		0.04		0.38		0.96	

Table 3.4.2 Comparison between the dimensions of the thermally ablated area induced in unrestricted samples of tissue (bulk) and in thin samples with capsule radiating 60 W for 10 min with the Amica MTA system. Average values (Avg ± st. dev.) and statistical difference evaluated between the two groups of date (p-value) are reported.

	L_A		D_A		L_C		D_C		I		P		A	
	bulk	**thin**	**bulk**	**thin**	**bulk**	**thin**	**bulk**	**thin**	**bulk**	**thin**	**bulk**	**thin**	**bulk**	**thin**
Avg	57.6	56.7	39.3	39.3	34.5	40.0	11.0	9.7	12.2	18.5	6.9	6.0	8.2	8.7
St. dev	3.6	1.0	3.5	2.5	4.7	2.3	2.1	0.8	3.0	2.8	2.5	2.3	2.3	2.4
p-value	0.53		0.97		0.02		0.16		0.00		0.47		0.69	

Table 3.4.3 Comparison between the dimensions of the thermally ablated area induced in thin samples with (yes) and without (no) capsule radiating 60 W for 10 min with the Amica MTA system. Average values (Avg ± st. dev.) and statistical difference evaluated between the two groups of date (p-value) are reported.

	L_A		D_A		L_C		D_C		I		P		A	
	yes	**no**	**yes**	**no**	**yes**	**no**	**yes**	**no**	**yes**	**no**	**yes**	**no**	**yes**	**no**
Avg	56.7	55.0	39.3	36.5	40.0	36.2	9.7	9.5	18.5	15.5	6.0	5.8	8.7	8.3
St. dev	1.0	1.9	2.5	3.4	2.3	1.5	0.8	1.0	2.8	2.8	2.3	1.8	2.4	1.7
p-value	0.09		0.13		0.01		0.77		0.09		0.88		0.77	

Form the values reported in Table 3.4.1 it is possible to note that the reduced thickness of the tissue along the sagittal plane does not influence (p-value > 0.05) the dimension of the thermally ablated region along the coronal plane. While in Table 3.4.2 and in Table 3.4.3 it is evidenced that the presence of the capsule induce a statistically significant increment of the extension of the carbonized tissue along the antenna axis (p-value < 0.05), although without altering the dimension of the whole ablated area. Concerning the inflection, it resulted statistically greater for the thin samples (p-value < 0.05) with respect to the unrestricted case, in presence of the liver's capsule as well as in its absence.

3.4.2 Numerical analysis of the antenna performances

3D electromagnetic simulations were performed with the commercial software CST Microwave Studio simulating the 14G Amica antenna produced from the HS Hospital Service company and evaluating its performances in different samples of liver tissue. Aiming to investigate the influence of the size and shape of the heated tissue, the antenna return loss and the energy deployed were evaluated for the different considered cases.

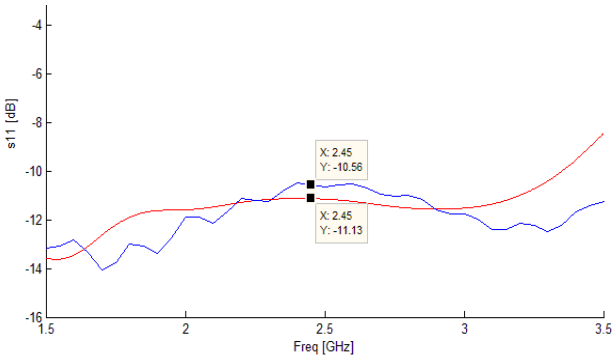

Figure 3.4.2 S11measured @ 2.45 GHz: commercial software (red) vs iin-house software (blu).

Firstly, the reliability of the proposed CST model was assessed comparing the results obtained with the commercial software with the results obtained through an experimentally validated antenna model simulated with an in-house developed numerical code (Cavagnaro *et al*., 2015a). In Figure 3.4.2, the s11 parameters, representative of the amount of power reflected from the antenna, obtained from the two simulations are illustrated comparing the results in a range of

frequencies centered on 2.45 GHz. In the neighborhood of the working frequency, both analyses show a return loss lower than -10 dB. Once validated the cylindrical symmetry of the induced 3D SAR, the values obtained through CST were compared with those obtained with the in-house elaboration. The resulting SAR, normalized to the maximum value obtained at about 3 mm from the antenna surface, are reported in Figure 3.4.3: the trends of the obtained SAR as a function of the radial distance from the antenna surface were compared in correspondence to the antenna tip, feed and choke. The illustrated curves show a perfect compliance of the SAR profiles evaluated with the two software, validating the reliability of the CST outcomes. Therefore, the profiles observed, as well as the map of SAR reported in Figure 3.4.4, can be taken as reference for the following analyses on restricted samples of biological tissue.

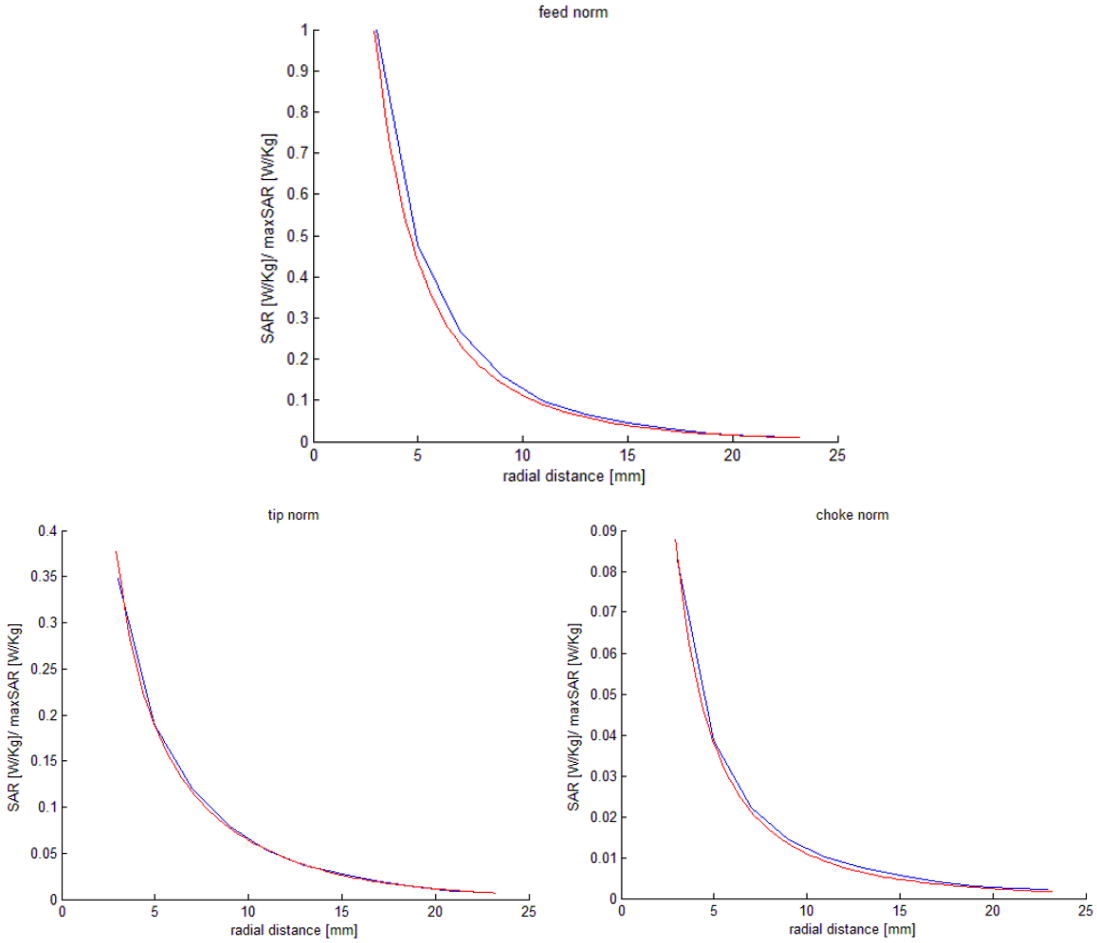

Figure 3.4.3 Comparison between the SAR values evaluated by CST (red) and by the in-house software (blue) as function of the radial distances from the antenna surface (in the 3-23 mm range), in correspondence with the antenna feed (top), tip (bottom left), and choke (bottom right).

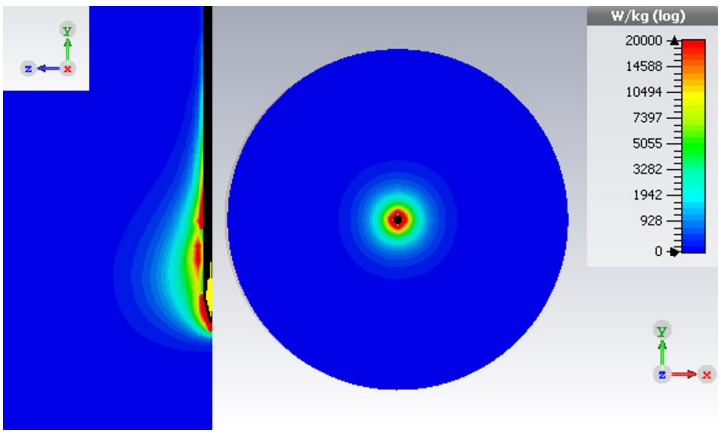

Figure 3.4.4 SAR map into the unrestricted tissue surrounding the MTA antenna: section along the antenna axis at the antenna feed (left: yz-plane) and sectrion transverse to the antenna axis (right: xy-plane).

3.4.2.1 Thin samples of tissue

The dimensions of the tissue surrounding the antenna were then reduced to simulate the electromagnetic changes occurring in samples of tissue of restricted dimensions and evaluate possible correlations with the results obtained experimentally in par. *3.4.1*. The antenna was placed in a brick of tissue with one of the dimensions orthogonal to the antenna axis reduced to a thickness of 20 mm (Figure 3.4.5). No substantial differences are observed at the frequency of interest (2.45 GHz) in terms of antenna return loss (s11) as shown in Figure 3.4.6.

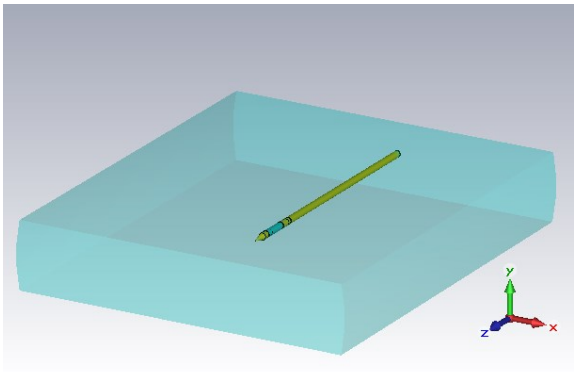

Figure 3.4.5 Antenna (yellow) in thin tissue design (light blue brick), with Cartesian coordinates (CST software).

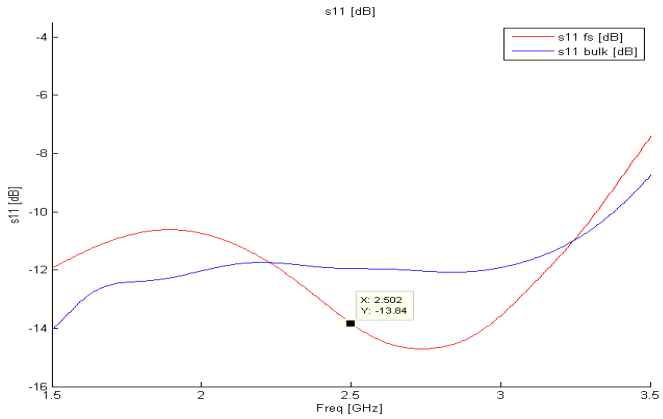

Figure 3.4.6 S11 measured @ 2.45 GHz: in unrestricted (blue) vs in 20 mm thin (red) samples of bovine liver.

In Figure 3.4.7, the SAR chosen as reference (unrestricted case – SAR bulk) is compared with the SAR obtained in the 20 mm thin liver sample, reporting the profile observed in the not restricted radial direction (SAR large) as well as in the limited one (SAR thin). In close proximity of the antenna axis, i.e. in the first 5 mm interested from the charred area, similar trends are shown confirming the absence of differences observed between the unrestricted and thin cases in the experimental outcomes of par 3.4.1 (no capsule). At the antenna feed and tip, in the not limited direction of the thin sample (blue curve), the SAR further decreases with respect to the reference case (black curve), reaching a minimum at about 15 mm from the antenna axis, and successively increases pointing out a hot spot at a distance between 20 and 30 mm from the antenna axis. Considering that the maximum radius of the thermally ablated area is of about 20 mm at the feed, it is possible to point out that the differences observed in the SAR profile do not substantially influence the formation of the thermally ablated area (measures of Table 3.4.1). At the antenna feed, as well at the choke and tip, in the limited direction (red curve), it is possible to note the alteration of the SAR profile induced from the tissue-air discontinuity, with a consequent increase of the amount of deposited energy at the end of the tissue sample. The hot spots suggested from the profiles of Figure 3.4.7 are clearly visible in the SAR distribution reported in Figure 3.4.8 concerning the thin brick of liver.

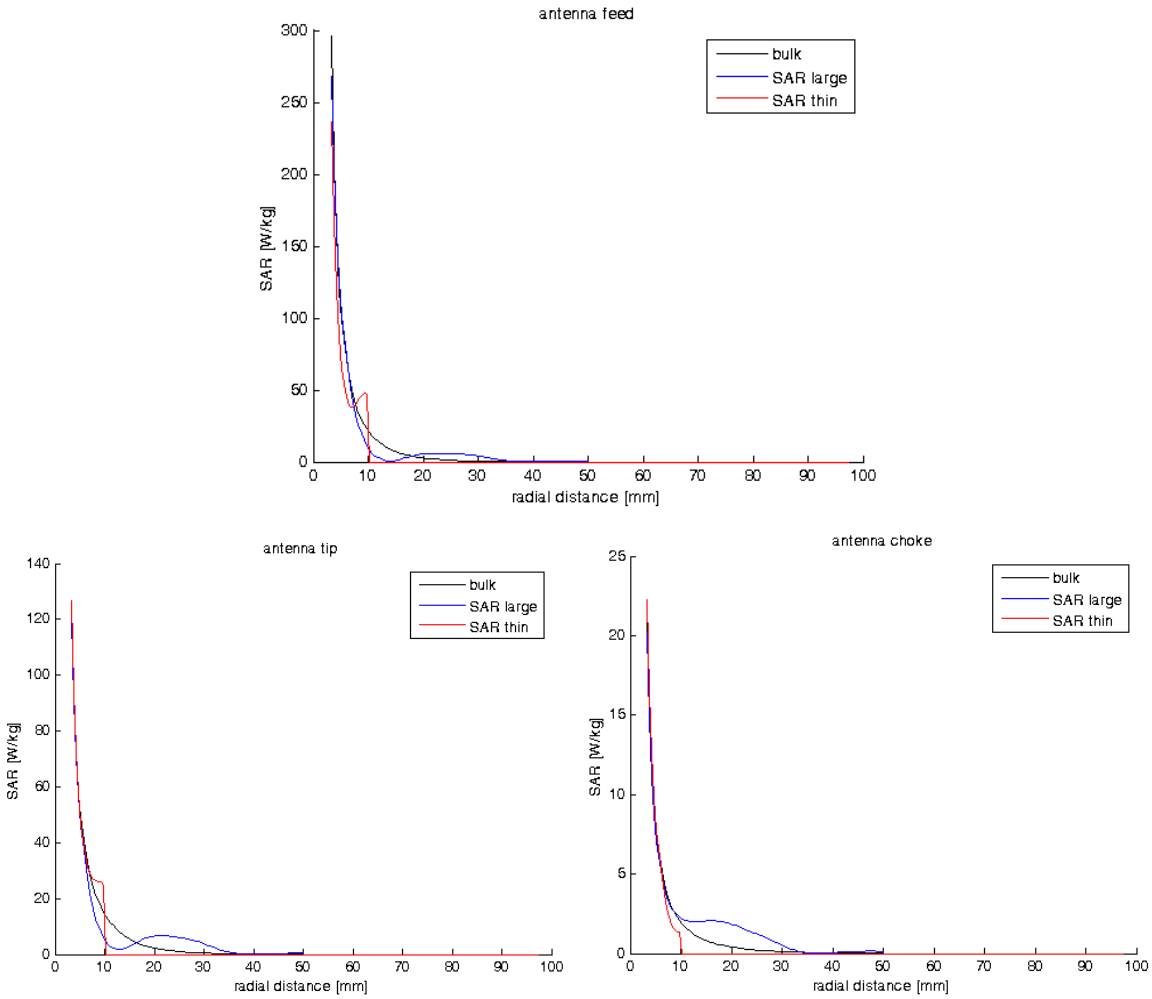

Figure 3.4.7 SAR evaluated in liver tissue as function of the radial distances from the antenna surface, in correspondence with the antenna feed (top), tip (bottom left), and choke (bottom right); comparison of the profile obtained in the unrestricted case (black) and in a 20 mm thin sample in the two direction orthogonal to the antenna axis (red: limited at 20 mm, blue: not limited).

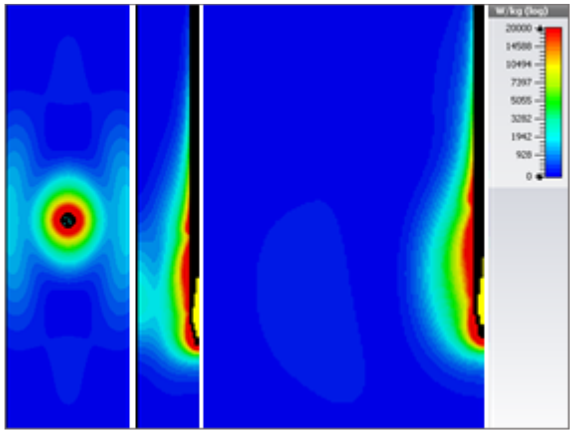

Figure 3.4.8 SAR map into the tissue surrounding the MTA antenna: 20 mm thin sample. From left to right: the section ortogonal to the antenna axis at the antenna feed (xy-plane), the half-plane hosting the unrestricted radial direction (xz-plane, x-direction), the half plane hosting the radial limited direction (yz-plane, y-direction).

The numerical analysis was then deepened evaluating variable thicknesses of the biological tissue: 10 mm and 40 mm, illustrated in Figure 3.4.9, left and right panel respectively. It is possible to observe that the 40 mm thin sample still guarantee an unvaried SAR profile with respect to the unrestricted case, in both the transverse directions, although pointing out a slight asymmetry due to the tissue-air discontinuity. Whereas, in the 10 mm thin sample, the limitation introduced in the y-direction induces a noticeable increment of the electromagnetic field absorbed in the unrestricted direction.

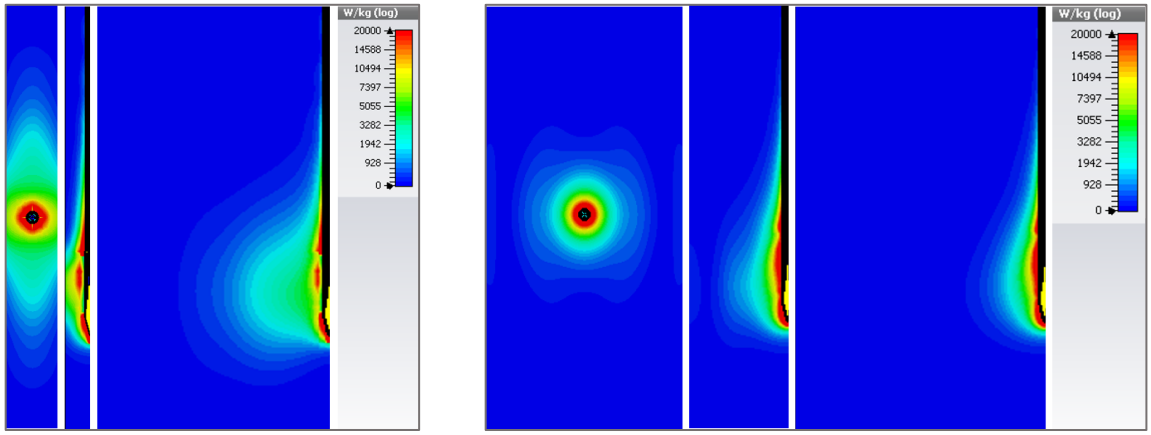

Figure 3.4.9 SAR map into the tissue surrounding the MTA antenna: left panel 10 mm thin sample; right panel: 40 mm thin sample. In each panel, from left to right: the section ortogonal to the antenna axis at the antenna feed (xy-plane), the half-plane hosting the unrestricted radial direction (xz-plane, x-direction), the half plane hosting the radial limited direction (yz-plane, y-direction).

3.4.2.2 Cubic samples of tissue

The experimental setup proposed to thermally ablate cubic samples of liver tissue of sizes of 10, 20, 30 and 40 mm was modeled through the 3D full wave software and numerical analysis were conducted to evaluate eventual SAR modifications introduced from the restricted tissue dimensions. The numerical design accounted also the presence of the Agar phantom, as depicted in Figure 3.4.10. In all the simulated cases, the return loss did not show substantial variation at the frequency of interest (2.45 GHz), resulting in s11 values between -11 dB and – 12 dB, compliant with that observed in Figure 3.4.2 for the reference case (i.e. unrestricted block of liver tissue).

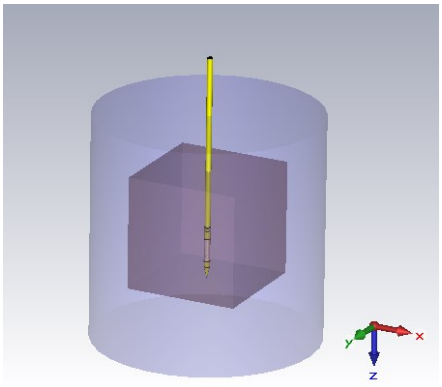

Figure 3.4.10 Design of a MTA antenna (yellow) in a cube of liver tissue (light purple brick) embedded in an Agar phantom (light blu cylinder), with Cartesian coordinates (CST software).

Form Figure 3.4.11 and Figure 3.4.12, it is possible to observe an increase of the deposited energy in proximity of the antenna feed with the decreasing size of the tissue cube; nevertheless, the presence of the agar phantom guarantees a uniform distribution of the electromagnetic field, not changed with respect to the unrestricted case. Moreover, no hot spots are appreciable into the tissue thanks to the presence of the agar phantom, with the exception of the 10 mm cube: in Figure 3.4.12, it is possible to observe a further increase of the deposited energy at the discontinuity between the tissue and the phantom in correspondence of the antenna feed.

Thus, the proposed agar phantom allow reducing the influence of the discontinuity introduced by the reduced dimensions of the tissue samples adopted.

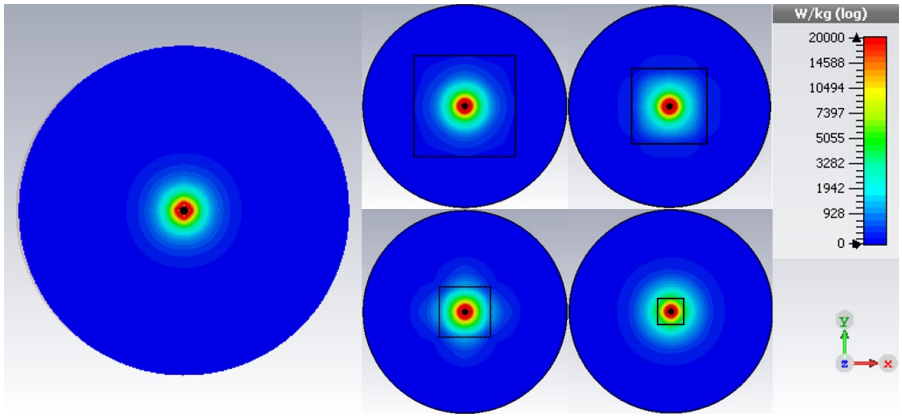

Figure 3.4.11 SAR map into the tissue surrounding the MTA antenna; xy-plane orthogonal to the antenna axis in correspondence to the antenna feed; unrestricted liver tissue (left) and cubes of liver tissue of different sizes (black wire boxes from top left to bottom right: 40 mm, 30 mm, 20 mm, and 10 mm side) embedded in agar phantom.

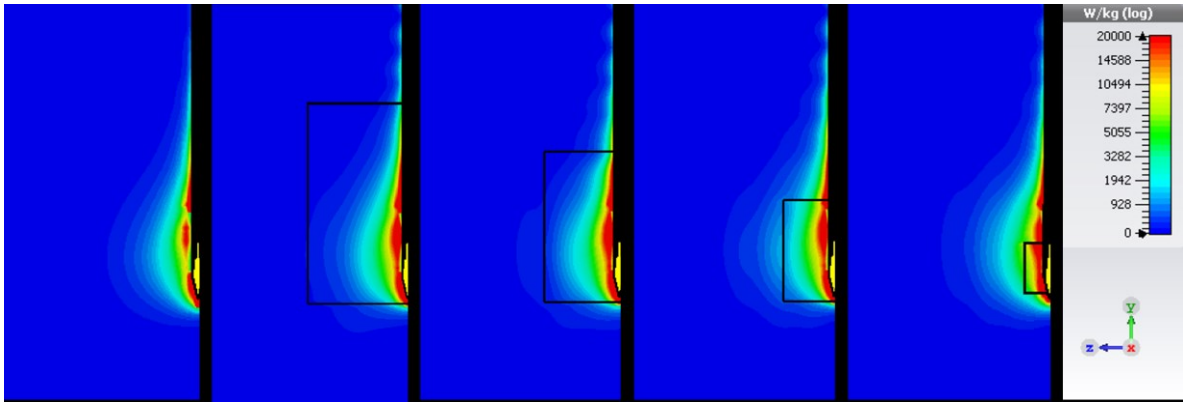

Figure 3.4.12 SAR map into the tissue surrounding the MTA antenna; yz-plane paralel to the antenna axis; unrestricted liver tissue (left) and cubes of liver tissue of different sizes (black wire boxes from left to right: 40 mm, 30 mm, 20 mm, and 10 mm side) embedded in agar phantom.

3.5 In vivo dielectric spectroscopy

3.5.1 Setup optimization

Measurements of complex dielectric permittivity were conducted on liquids and *ex vivo* bovine liver with the "golden standard setup" as well as with the portable setup; the outcomes of the tests were compared.

Table 3.5.1 reports measured data at two reference frequencies within the two considered frequency band (i.e., 1 GHz belonging to the lower band, 500 – 1500 MHz, and 2.45 GHz belonging to the higher one, 1500 MHz – 3000 MHz). In the Table 3.5.2, the two calibration liquids are measured (distilled water and methanol), as well as two different standard liquids (acetone and propanol). A percent error within 7% is achieved, with the exception of the measurements performed in acetone where an error greater than 40% is observed in the conductivity (σ) at 2.45 GHz. It is possible to ascribe this error, consisting in an absolute difference of about 0.03 S/m, to the very low conductivity value at high frequencies. When measurements were carried out over a single broad frequency band, i.e. between 500 and 3000 MHz, the measurement accuracy remained comparable to that achieved performing measurements over the two narrower bands. Measurements carried out on *ex vivo* biological samples report promising results. Table 3.5.2

shows the results of repeated measurements, in terms of mean values and range of variation, carried out on *ex vivo* liver tissue at two reference frequencies (1 GHz and 2.45 GHz respectively). A good agreement between the results achieved with the golden standard and the portable setup is observed: an error lower than 1% is reported, which is within the measurement uncertainty of the golden standard setup (5%). Therefore, the proposed setup results suitable to perform reliable and accurate dielectric measurements, ensuring at the same time the portability for on-site experimental activities. However, it is interesting to note here that the measured values are not so close to literature data (e.g. ε = 46.4, σ = 0.90 S/m at 1.00 GHz, http://niremf.ifac.cnr.it/tissprop/htmlclie/htmlclie.php), pointing to the variability of tissue characteristics as listed above.

Table 3.5.1 Measurements of the dielectric properties of standard liquids @ 1 GHz and @ 2.45 GHz.

	1.00 GHz						**2.45 GHz**					
	Golden Standard		**Portable Setup**		**Percent Difference**		**Golden Standard**		**Portable Setup**		**Percent Difference**	
	ε	σ [S/m]	ε	σ [S/m]	$\Delta\varepsilon$	$\Delta\sigma$	ε	σ [S/m]	ε	σ [S/m]	$\Delta\varepsilon$	$\Delta\sigma$
Acetone	19.93	0.02	21.09	0.02	5.8 %	0.0 %	20.78	0.07	21.07	0.10	1.4%	42.9%
Distilled water	77.85	0.20	78.16	0.21	0.4 %	5.0 %	77.04	1.21	77.19	1.25	0.2%	3.3%
Methanol	29.28	0.42	30.52	0.45	4.2 %	7.1 %	22.78	1.77	22.71	1.78	0.3%	0.6%
Propanol	5.94	0.33	6.32	0.34	6.4 %	3.0 %	4.05	0.40	4.06	0.41	0.2%	2.5%

Table 3.5.2Measurements of the dielectric properties of ex vivo bovine liver @ 1 GHz and @ 2.45 GHz.

1.00 GHz	**Golden Standard**		**Portable Setup**		**Percent Difference**		**2.45 GHz**	**Golden Standard**		**Portable Setup**		**Percent Difference**	
	ε	σ [S/m]	ε	σ [S/m]	$\Delta\varepsilon$	$\Delta\sigma$		ε	σ [S/m]	ε	σ [S/m]	$\Delta\varepsilon$	$\Delta\sigma$
average	54.7	1.08	54.5	1.08	0.4%	0.0 %	average	50.8	1.99	51.3	2.00	1.0 %	0.5 %
min	52.2	1.01	53.5	1.05			min	48.4	1.88	50.1	1.94		
max	56.7	1.14	56.6	1.13			max	53.4	2.11	53.1	2.08		

3.5.2 Healthy breast model characterization

Measurement of the *in vivo* dielectric properties of healthy breast models (Prague pseudo-breast – PB) developed in rats, developed at the Academy of Sciences of the Czech Republic by Prof. Luca Vannucci, were conducted with the portable setup proposed in par. 2.4.1 and validated in par. 3.5.1. The portability of the setup allowed performing the experiments directly in the laboratories of the Czech Academy of Science where the experimental animals were treated and prepared, avoiding their transportation.

Table 3.5.3 Measurements of the in vivo dielectric properties of the Prague pseudo-breast model @ 1.5 GHz and @ 2.45 GHz.

In vivo	Pseudo-breast		1500 MHz		2450 MHz	
Rat	**Size**	**Temperature**	**ε**	**σ**	**ε**	**σ**
	[cm]	[°C]		[S/m]		[S/m]
#2	1.8 x 1.5 x 1.0	28.6	14.46 ± 0.92	0.34 ± 0.01	14.98 ± 0.23	0.48 ± 0.00
			14.59 ± 0.21	0.33 ± 0.00	14.09 ± 0.22	0.46 ± 0.00
#3	2.2 x 2.2 x 1.4		15.98 ± 2.58	0.37 ± 0.06	16.12 ± 1.91	0.51 ± 0.08
			16.77 ± 1.25	0.37 ± 0.03	16.09 ± 1.19	0.51 ± 0.04
			10.15 ± 0.06	0.18 ± 0.00	9.86 ± 0.05	0.24 ± 0.01
			13.73 ± 0.08	0.33 ± 0.00	13.26 ± 0.08	0.45 ± 0.00
			13.50 ± 0.28	0.21 ± 0.00	13.05 ± 0.30	0.31 ± 0.01
			10.02 ± 0.08	0.24 ± 0.01	9.62 ± 0.08	0.33 ± 0.01
#4	2.5 x 2.0 x 1.5	31.5	14.35 ± 2.26	0.35 ± 0.05	14.26 ± 2.16	0.53 ± 0.08
#5	2.2 x 2.0 x 1.0	32.7	7.24 ± 1.30	0.14 ± 0.04	7.12 ± 1.16	0.24 ± 0.05
			7.01 ± 0.45	0.13 ± 0.01	6.71 ± 0.43	0.20 ± 0.02
			8.31 ± 1.97	0.15 ± 0.05	7.97 ± 1.64	0.23 ± 0.07
#6	3.0 x 2.2 x 1.2	29.0	14.44 ± 2.05	0.33 ± 0.06	12.63 ± 4.13	0.49 ± 0.16
			7.31 ± 0.37	0.17 ± 0.01	7.30 ± 0.52	0.26 ± 0.01
			6.66 ± 0.14	0.14 ± 0.00	6.38 ± 0.13	0.21 ± 0.00
#8	1.7 x 1.8 x 1.0	29.5	8.45 ± 1.48	0.19 ± 0.04	7.77 ± 1.33	0.26 ± 0.05
			7.82 ± 0.29	0.20 ± 0.01	7.22 ± 0.49	0.26 ± 0.02

In Table 3.5.3, *in vivo* results on PB are shown: for each measurement point, average and standard deviation values are reported. Following, the *ex vivo* results on PB are shown in Table 3.5.4 (1 h and 24 h from sacrifice). From the tables a great variability of both permittivity and conductivity is evidenced. Lower permittivity values are measured in rat #5 and rat #8 with respect to the other PBs: in these cases, the PB were prepared only two weeks in advance and probably

they had less time to develop fibrous, lymphatic and vascular components typical of the ones realized some weeks before. On the contrary, the typical dis-homogeneity in the PBs of rat #2, #3, #4, and #6 could be the reason of the higher measured permittivity and conductivity values. However, the dis-homogeneity can usefully mimic the practical condition of a real breast evaluation. No significant differences are evidenced between *in vivo* and *ex vivo* ranges of measurements, thus these preliminary observations seem to indicate that the biophysical phenomena occurring in PBs after the excision from the host do not infer the dielectric properties behavior. Finally, the permittivity and conductivity values, however characterized by a great variability, result compliant with those proposed from Zastrow et al. (accessible at: https://uwcem.ece.wisc.edu/MRIdatabase/InstructionManual.pdf).

Table 3.5.4 Measurements of the ex vivo dielectric properties of the Prague pseudo-breast model @ 1.5 GHz and @ 2.45 GHz.

Ex vivo 1 h	Pseudo-breast		1500 MHz		2450 MHz	
Rat	**Size**	**Temperature**	**ε**	**σ**	**ε**	**σ**
	[cm]	[°C]		[S/m]		[S/m]
#2	1.8 x 1.5 x 1.0		12.67 ± 0.12	0.26 ± 0.00	12.25 ± 0.11	0.37 ± 0.00
#3	2.2 x 2.2 x 1.4	22.3	11.96 ± 0.16	0.24 ± 0.00	11.57 ± 0.16	0.35 ± 0.01
#4	2.5 x 2.0 x 1.5	20.6	11.36 ± 0.89	0.25 ± 0.02	10.98 ± 0.86	0.36 ± 0.04
#5	2.2 x 2.0 x 1.0	20.0	9.84 ± 0.50	0.21 ± 0.01	9.46 ± 0.48	0.33 ± 0.02
#6	3.0 x 2.2 x 1.2	28.5	9.26 ± 1.62	0.19 ± 0.03	9.17 ± 1.05	0.30 ± 0.05
#8	1.7 x 1.8 x 1.0	27.6	6.23 ± 0.62	0.17 ± 0.02	5.94 ± 0.60	0.23 ± 0.03

Ex vivo 24 h	Pseudo-breast		1500 MHz		2450 MHz	
Rat	**Size**	**Temperature**	**ε**	**σ**	**ε**	**σ**
	[cm]	[°C]		[S/m]		[S/m]
#2	1.8 x 1.5 x 1.0		9.62 ± 0.22	0.19 ± 0.00	9.02 ± 0.20	0.29 ± 0.01
#3	2.2 x 2.2 x 1.4		14.83 ± 0.43	0.36 ± 0.01	14.26 ± 0.43	0.48 ± 0.02
#4	2.5 x 2.0 x 1.5	20.3	8.63 ± 0.26	0.22 ± 0.00	8.32 ± 0.24	0.31 ± 0.01
#5	2.2 x 2.0 x 1.0	21.2	7.16 ± 1.08	0.19 ± 0.03	6.83 ± 0.75	0.27 ± 0.04
			4.85 ± 0.27	0.13 ± 0.01	4.62 ± 0.26	0.18 ± 0.01
#6	3.0 x 2.2 x 1.2	22.0	6.11 ± 0.76	0.15 ± 0.02	6.18 ± 0.69	0.23 ± 0.03
			4.77 ± 0.19	0.13 ± 0.01	4.58 ± 0.19	0.17 ± 0.01

3 Conclusions

Aim of the work conducted in these three years was to fully characterize the shrinkage phenomenon occurring in the biological tissue treated with a microwave thermal ablation procedure, and to develop, if possible, a simple model in order both to help physicians conducting clinical trials in as safe as possible conditions, and to increase the technique applicability.

In the present thesis, the experimental results obtained investigating the tissue shrinkage are motivated, illustrated, and commented.

A substantial tissue shrinkage, dependent on the radiated power and time of exposure, and significantly higher close to the antenna axis, was demonstrated. Moreover, the extent of shrinkage was correlated to the tissue status, independently from the nature of the radiating source. Carbonization, the culmination and final, maximal point of the shrinkage process, involving totally desiccated and dehydrated tissue, plays a crucial role in the evolution of tissue shrinkage in microwave thermal ablation. In the tissue belonging to the thermally coagulated zone, but not carbonized, the shrinkage appears as a progressive process linearly increasing with tissue temperature. Congruent with these findings, influence of the device design on the shrinkage was found: in particular, internal cooling demonstrated to prevent formation of carbonization for short ablation times and resulted in a different shrinkage profile in the tissue, although not altering the total shrinkage observed at the boundary of the ablated area.

Analyzing the tissue in real-time during the procedure, the local tissue movement resulted in a complex rotatory movement accounting a first phase of expansion, in some cases, followed by contraction.

With reference to temperature data, carbonization resulted linked to temperatures above 110 °C and up to 128 °C; above 65 °C coagulation was found. In the tissue closer to the radiating source a direct heating was assessed, whereas out of the coagulated tissue a heating phenomenon linked to the heat conduction was observed.

Following the previous considerations an analytical model of the tissue's shrinkage, based on the contraction measured in the tissue, has been developed, proposed and successfully validated. Such a model would allow to control and predict tissue shrinkage, increasing the safety and efficacy of microwave-based thermal treatments and supporting the physicians in the clinical assessment. Furthermore, it would be potentially suitable for implementation in computer-assisted simulations of clinical treatments.

Further studies should be conducted to fully characterize the shrinkage occurring longitudinally to the antenna axis, since some gaps of knowledge are still left. Additional researches could be conducted to completely assess the temperatures induced into the treated tissue, investigating the thermal profiles linked to different antenna cooling system design, and the eventual correlation between the tissue status and its appearance under CT.

Finally, a portable setup for *in vivo* characterization of the biological tissue dielectric properties was developed and optimized with satisfactory results. Further studies should be conducted to measure *in vivo* dielectric properties of healthy and pathological tissue to support future developments in theranostic techniques.

References

Acculis™ MTA system AngioDynamics: brochures and products' specifications. Available at: http://www.angiodynamics.com/products/Acculis

Ahmed M, Brace CL, Lee FT Jr, Goldberg SN. (2011). Principles of and advances in percutaneous ablation. Radiology 258(2):351-369

Ahmed M, et al. (2014). Image-guided tumor ablation: Standardization of terminology and reporting criteria – A 10-year update. Radiology 273(1):241-260

Agilent E4418B Power Meter Agilent Technologies, Inc. User's guide, Eighth Edition, April 5, 2013

Amabile C, Farina L, Lopresto V, Pinto R, Cassarino S, Tosoratti N, Goldberg SN, Cavagnaro M. (2016). Tissue shrinkage in microwave ablation of liver: an ex-vivo predictive model. Int J Hyperthermia [Epub ahead of print]

AMICA™ system HS Hospital Service SpA: apparatus for microwave ablation. Technical Presentation. Available at: http://www.hshospitalservice.com/index.php.

Andreuccetti D, Fossi R, Petrucci C. An Internet resource for the calculation of the dielectric properties of body tissues in the frequency range 10 Hz–100 GHz. Available at: http://niremf.ifac.cnr.it/tissprop/

Brace CL, Hinshaw JL, Laeseke PF, Sampson LA, Lee FT Jr. (2009). Pulmonary thermal ablation: Comparison of radiofrequency and microwave devices by using gross pathologic and CT findings in a swine model. Radiology 251(3)

Brace CL, Diaz TA, Hinshaw JL, Lee FT Jr. (2010). Tissue contraction caused by radiofrequency and microwave ablation: A laboratory study in liver and lung. J Vasc Interv Radiol 21:1280–1286

Brace CL, Gagnon D, Borden Z, Roen C. (2011). Ablation-induced tissue contraction measured by CT: Correlation with dehydration. *World Conference on Interventional Oncology*; New York, NY

Cavagnaro M, Amabile C, Bernardi P, Pisa S, Tosoratti N. (2011). A minimally invasive antenna for microwave ablation therapies: Design, performances, and experimental assessment. IEEE Trans Biomed Eng 58:949-59

Cavagnaro M, Pinto R, Lopresto V. (2015a). Numerical models to evaluate the temperature increase induced by ex vivo microwave thermal ablation. Phys Med Biol 60:3287–3311

Cavagnaro M, Amabile C, Cassarino S, Tosoratti N, Pinto R, Lopresto V. (2015b). Influence of the target tissue size on the shape of ex vivo microwave ablation zones. Int J Hyperthermia 31:48–57

Choi J, Morrissey M, Bischof JC. (2013). Thermal processing of biological tissue at high temperatures: impact of protein denaturation and water loss on the thermal properties of human and porcine liver in the range 25–80 °C. J Heat Transfer 135(6):061302.

Diaz TA, Sampson LA, Hinshaw JL, Lee FT Jr, Brace CL. (2008). Ablation-induced tissue shrinking: Ablation zone measurements do no accurately reflect pre-ablation volumes in liver and lung tissues. *World Congress on Interventional Oncology*, Jun 22-25, 2008, Los Angeles, CA

DICOM – Digital Imaging and Communications in Medicine. Information available at: dicom.nema.org/

Emprint™ system Covidien: brochures and products' specifications. Available at: http://www.medtronic.com/covidien/products/ablation-systems/emprint-ablation-system

Farina L, Weiss N, Nissenbaum Y, Cavagnaro M, Lopresto V, Pinto R, Tosoratti N, Amabile C, Cassarino S, Goldberg SN. (2014a). Characterization of tissue shrinkage during microwave thermal ablation. Int J Hyperthermia 30(7):419-428

Farina L, Weiss N, Nissenbaum Y, Cavagnaro M, Lopresto V, Pinto R, Tosoratti N, Amabile C, Cassarino S, Goldberg SN. (2014b). Dynamic CT tracking of tissue shrinkage during microwave thermal ablation. *Abstract collection 29th Annual Meeting of the European Society for Hyperthermic Oncology (ESHO)*, June 11-14, 2014, Torino, Italy. Panminerva Medica 56(2):40

Farina L, Weiss N, Nissenbaum Y, Cavagnaro M, Lopresto V, Pinto R, Tosoratti N, Amabile C, Cassarino S, Goldberg SN. (2014c). Monitoring of tissue shrinkage during a microwave thermal ablation procedure. *Proceedings of XX Riunione Nazionale di Elettromagnetismo (RiNEm)*, September 15 – 18, 2014, Padova, Italy

Farina L, Lopresto V, Pinto R, Cavagnaro M (2014d). Dielectric and thermal properties of tissues undergoing microwave thermal ablation procedures. *Proceedings of III Convegno Nazionale Interazione tra Campi Elettromagnetici e Biosistemi (ICEmB)*, July 2 – 4, 2014, Napoli, Italy

Farina L, Amabile C, Nissenbaum Y, Cavagnaro M, Lopresto V, Pinto R, Tosoratti N, Cassarino S, Weiss N, Goldberg SN. (2015a). Ex vivo tissue shrinking in microwave thermal ablation. *Proceeding of 9th European Conference on Antennas and Propagation (EuCAP)*, April 12 – 17, 2015, Lisbon, Portugal

Farina L, Lopresto V, Pinto R, D'Alessio D, Minosse S, Strigari L, Cavagnaro M. (2015b). The use of CT to improve the knowledge of the physical phenomena associated with microwave thermal ablation procedures. *Proceedings of 2015 International Conference on Electromagnetics in Advanced Applications (ICEAA)*, Sep 7–11, 2015, Torino, Italy

Farina L, Amabile C, Lopresto V, Pinto R, Cavagnaro M, Cassarino S, Tosoratti N, Goldberg SN. (2016a). An ex vivo study on the shrinkage occurring in bovine liver during microwave thermal ablation: Carbonized vs coagulated tissue. *Proceedings of Annual Meeting of BEMS and EBEA (BioEM),* June 5 – 10, 2016, Ghent, Belgium

Farina L, Lopresto V, Pinto R, D'Alessio D, Minosse S, Strigari L, Cavagnaro M. (2016b). CT study of the tissue shrinkage occurring during a microwave thermal ablation procedure. *Proceedings of V Gruppo Nazionale di Bioingegneria (Italian National Bioengineering Group – GNB)*, June 20 – 22, 2016 Napoli, Italy

Farina L, Nissenbaum Y, Cavagnaro M, Goldberg SN. (2016c) Tissue shrinkage in Microwave Thermal Ablation: Comparison of three commercial devices. Int. J Hyperthermia [Submitted]

Farina L & Cavagnaro M. (2016). Tissue shrinkage in microwave thermal ablation. *Proceedings of XXI Riunione Nazionale di Elettromagnetismo (RiNEm)*, September 12 – 14, 2016, Parma, Italy

Foster KR, Shepps JL. (1981). Dielectric properties of tumor and normal tissues at radio through microwave frequencies. J Microw Power 16:107–19

Gabriel C, Gabriel S, Corthout E. (1996a). The dielectric properties of biological tissues: I. Literature survey. Phys Med Biol 41:2231–2249

Gabriel S, Lau RW, Gabriel C. (1996b). The dielectric properties of biological tissues: II. Measurements in the frequency range 10 Hz to 20 GHz. Phys Med Biol 41:2251–2269

Gabriel C. (1996c) Compilation of the dielectric properties of body tissues at RF and microwave frequencies. Brooks Air Force Technical Report AL/OE-TR-1996-0037. Available at: http://www.fcc.gov/oet/rfsafety/dielectric.html

Ganguli S, Brennan DD, Faintuch S, Rayan ME, Goldberg SN. (2008). Immediate renal tumor involution after radiofrequeny thermal ablation," J. Vasc. Interv. Radiol. 19, 412-418 (2008)

Goldberg SN, Gazelle GS, Solbiati L, Livraghi T, Tanabe KK, Hahn PF, Mueller PR. (1998). Ablation of liver tumors using percutaneous RF therapy", Am J Roentgenol 170:1023-1028

Goldberg SN, Gazelle GS, Mueller PR. (2000). Thermal ablation therapy for focal malignancy: A unified approach to underlying principles, techniques, and diagnostic imaging guidance. Am J Roentgenol 174:323–331

Goldberg SN, et al. (2005). Image-guided tumor ablation: Standardization of terminology and reporting criteria. Radiology 235(3):728–739

Habash RWY, Bansal R, Krewski D, & Hafid AT. (2007). Thermal therapy, part III: Ablation. Crit Rev Biomed Eng 35:37-121

Halter RJ, et al. (2009). The correlation of in vivo and ex vivo tissue dielectric properties to validate electromagnetic breast imaging: Initial clinical experience. Physiol Meas 30(6):s121-136

Hines-Peralta AU, Pirani N, Clegg P, Cronin N, Ryan TP, Liu Z, Goldberg SN. (2006). Microwave ablation: results with a 2.45-GHz applicator in ex vivo bovine and in vivo porcine liver. Radiology 239:94–102

Hinshaw JL, et al. (2014). Percutaneous tumor ablation tools: microwave, radiofrequency, or cryoablation – what should you use and why? Radiographics 34:1344–62.

Hoffmann R, Rempp H, Erhard L, Blumenstock G, Perelra PL, Claussen CD, Clasen S. (2013). Comparison of four microwave ablation devices: An experimental study in ex vivo bovine liver. Radiology 268:89–97

Ierardi AM, Mangano A, Floridi C, Dionigi G, Biondi A, Duka E, Luccchina N, Lianos GD, Carrafiello G. (2015). A new system of microwave ablation at 2450 MHz: preliminary experience. Updates Surg 67:39–45

Ji Z & Brace CL. (2011). Expanded modeling of temperature-dependent dielectric properties for microwave thermal ablation. Physics in Medicine and Biology 56: 5249– 5264

Liang P, Dong B, Yu X, Yu D, Wang Y, Feng L, Xiao Q. (2005). Prognostic factors for survival in patients with hepatocellular carcinoma after percutaneous microwave ablation. Radiology 235(1)

Liang P, Yu X, Yu J, editors. (2015). Microwave ablation treatment of solid tumors. Dordrecht: Springer

Lin Y, Liang P, Yu XL, Yu J, Cheng ZG, Han ZY, Liu PY. (2014). Percutaneous microwave ablation of renal cell carcinoma is safe in patients with a solitary kidney. Urology 83(2):357–363

Liu D & Brace CL. (2013). Imaging during microwave ablation: Analysis of spatial and temporal tissue contraction. *Interventional Oncology Sans Frontières*, May 29-June 1, 2013, Villa Erba, Cernobbio, Italy

Liu D & Brace CL. (2014). CT imaging during microwave ablation: analysis of spatial and temporal tissue contraction. Med Phys 41:113303-1–9.

Lopresto V, Pinto R, Lovisolo GA, Cavagnaro M. (2012). Changes in the dielectric properties of ex vivo bovine liver during microwave thermal ablation at 2.45 GHz. Phys Med Biol 57:2309–27

Lopresto V, Pinto R, Cavagnaro M. (2014). Experimental characterisation of the thermal lesion induced by microwave ablation. Int J Hyperthermia 30(2):110-118

Lopresto V, Pinto R, D'Alessio D, Minosse S, Strigari L, Farina L, Cavagnaro M. (2015). CT-based characterization of ex vivo liver tissue undergoing microwave thermal ablation. *Proceeding of 30th Annual Meeting of the European Society for Hyperthermic Oncology (ESHO)*, June 24 – 27, 2015, Zurich, Switzerland

Lopresto V, Pinto R, Farina L, Cavagnaro M. (2016a). Treatment planning in Microwave Thermal Ablation: clinical gaps and recent research advances. Int J Hyperthermia [Epub ahead of print]

Lopresto V, Pinto R, Farina L, Cavagnaro M. (2016b). Microwave thermal ablation: effects of tissue properties variations in predictive models for treatment planning. *Advances in Magnetics Conference (AIM)*, March 14 – 16, 2016, Bormio, Italy

Marsland TP & Evans S. (1987). Dielectric measurements with an open-ended coaxial probe. Micreowave Antennas and Propagation 134:341-349

Minosse S, D'Alessio D, Lopresto V, Pinto R, Farina L, Cavagnaro M, Strigari L. (2016) CT-based monitoring of microwave thermal ablation. *Proceeding of the 9° National Congress of the Italian Association of Medical Physics (AIFM)*, February 25 – 28, 2016, Perugia, Italy

Mitsuzaki K, Yamashita Y, Nishiharu T, Sumi S, Matsukawa T, Takahashi M, Beppu T, Ogawa M. (1998). CT appearance of hepatic tumors after microwave coagulation therapy. Am J Roentgenol 171(5):1397-1403

National Institute for Health and Care Excellence. (2012). New generation cardiac CT scanners (Aquilion ONE, Brilliance iCT, Discovery CT750 HD and Somatom Definition Flash) for cardiac imaging in people with suspected or known coronary artery disease in whom imaging is difficult with earlier generation CT scanners. NICE diagnostics guidance. Available at: www.nice.org.uk/dg3

O'Rourke AP, Lazebnik M, Bertram JM, Converse MC, Hagness SC, Webster JG, Mahvi DM. (2007). Dielectric properties of human normal, malignant and cirrhotic liver tissue: in vivo and ex vivo measurements from 0.5 to 20 GHz using a precision open-ended coaxial probe. Phys Med Biol 52:4707–4719.

Peyman A, Kos B, Djokić M, Trotovšek B, Limbaeck-Stokin C, Serša G, Miklavčič D. (2015). Variation in dielectric properties due to pathological changes in human liver. Bioelectromagnetics 36(8): 603-612

Planché O, Teriitehau C, Boudabous S, Robinsion JM, Rao P, Deschamps F, Farouil G, De Baere T. (2013). In Vivo Evaluation of Lung Microwave Ablation in a Porcine Tumor Mimic Model. Cardiovasc Intervent Radiol 36:221-228

Raman SS, Lu DSK, Vodopich DJ, Sayre J, Lassman C. (2000). Creation of radiofrequency lesions in a porcine model: Correlation with sonography, CT, and histopathology. Am J Roentgenol 175(5):1253-1258

Rossmann C, Garrett-Mayer E, Rattay F, Haemmerich D. (2014). Dynamics of tissue shrinkage during ablative temperature exposures. Physiol Meas 35:55-67

Ruvio G, Solimene R, Cuccaro A, Gaetano D, Browne JE, Ammann MJ. (2014). Breast cancer detection using interferometric MUSIC: experimental and numerical assessment. Med Phys 41(10):103101/1-11

Ryan TP, Turner PF, Hamilton B. (2010). Interstitial microwave transition from hyperthermia to ablation: Historical perspectives and current trends in thermal therapy. Int J Hyperthermia 26:415–33

Smalcerz A & Prylucki R. (2013). Impact of electromagnetic field upon temperature measurement of induction heated charges. Int J Thermophys 34(4): 667-679

Smith SL, Jennings PE. (2015). Lung radiofrequency and microwave ablation: a review of indications, techniques and post-procedural imaging appearances. Br J Radiol 88(1046):20140598

Sommer CM et al. (2013). Quantification of tissue shrinkage and dehydration caused by microwave ablation: experimental study in kidneys for the estimation of effective coagulation volume. J Vasc Interv Radiol 24(8):1241- 1248

Swan RZ, Sindram D, Martinie JB, Iannitti DA (2013). Operative microwave ablation for hepatocellular carcinoma: complications, recurrence, and long-term outcomes. J Gastrointest Surg. 17(4):719-729

Vannucci L, et al. (2016). Nanoconstructs for targeting the tumor microenvironment. *Proceedings of the 21st World Congress on Advances in Oncology (WCAO)*, Oct 6-8, 2016, Athens, Greece

Vogl TJ, Naguib NNN, Gruber-Rouh T, Koitka K, Lehnert T, Nour-Eldin NA. (2011). Microwave ablation therapy: Clinical utility in treatment of pulmonary metastases. Radiology 261

Yang D, Converse MC, Mahvi DM, Webster JG. (2007). Measurement and analysis of tissue temperature during microwave liver ablation. IEEE Trans Biomed Eng 54:1382–8

Yu J, Liang P, Yu X, Cheng Z, Han Z, Mu M, Wang X. (2012). Us-guided percutaneous microwave ablation of renal cell carcinoma: Intermediate-term results. Radiology 263(3)

Weiss N, Goldberg SN, Nissenbaum Y, Sosna J, Azhari H. (2015). Planar strain analysis of liver undergoing microwave thermal ablation using X-ray CT. Med Phys 42:372–380

Zastrow E, Davis SK, Lazebnik M, Kelcz F, Van Veen DB, Hagness SC. Database of 3D Grid-Based Numerical Breast Phantoms for use in Computational Electromagnetics Simulations, UWCEM Numerical Breast Phantom Repository. Available at: https://uwcem.ece.wisc.edu/MRIdatabase/InstructionManual.pdf

List of figures

tissue of different sizes (black wire boxes from top left to bottom right: 40 mm, 30 mm, 20 mm, and 10 mm side) embedded in agar phantom.

Figure 3.4.12 SAR map into the tissue surrounding the MTA antenna; yz-plane paralel to the antenna axis; unrestricted liver tissue (left) and cubes of liver tissue of different sizes (black wire boxes from left to right: 40 mm, 30 mm, 20 mm, and 10 mm side) embedded in agar phantom.

List of tables

List of publications

Papers on international journals

1. Farina L, Weiss N, Nissenbaum Y, Cavagnaro M, Lopresto V, Pinto R, Tosoratti N, Amabile C, Cassarino S, Goldberg SN. (2014). Characterization of tissue shrinkage during microwave thermal ablation. Int J Hyperthermia 30(7):419-428. DOI: 10.3109/02656736.2014.957250

2. Lopresto V, Pinto R, Farina L, Cavagnaro M. (2017). Treatment planning in Microwave Thermal Ablation: clinical gaps and recent research advances. Int J Hyperthermia 33(1):83-100. DOI: 10.1080/02656736.2016.1214883.

3. Amabile C, Farina L, Lopresto V, Pinto R, Cassarino S, Tosoratti N, Goldberg SN, Cavagnaro M. (2017). Tissue shrinkage in microwave ablation of liver: an ex-vivo predictive model. Int J Hyperthermia 33(1):101-109. DOI: 10.1080/02656736.2016.1208292.

4. Farina L, Nissenbaum Y, Cavagnaro M, Goldberg SN. (2017) Tissue shrinkage in Microwave Thermal Ablation: Comparison of three commercial devices. Int. J Hyperthermia [Submitted]

5. Lopresto V, Pinto R, Farina L, Cavagnaro M. (2017). Microwave thermal ablation: effects of tissue properties variations on predictive models for treatment planning. Med Eng Phys [Submitted]

Conferences proceedings

6. Farina L, Weiss N, Nissenbaum Y, Cavagnaro M, Lopresto V, Pinto R, Tosoratti N, Amabile C, Cassarino S, Goldberg SN. (2014). Dynamic CT tracking of tissue shrinkage during microwave thermal ablation. *Abstract collection 29th Annual Meeting of the European Society for Hyperthermic Oncology (ESHO)*, June 11-14, 2014, Torino, Italy. Panminerva Medica 56(2):40.

7. Farina L, Weiss N, Nissenbaum Y, Cavagnaro M, Lopresto V, Pinto R, Tosoratti N, Amabile C, Cassarino S, Goldberg SN. (2014). Monitoring of tissue shrinkage during a microwave thermal ablation procedure. *Proceedings of XX Riunione Nazionale di Elettromagnetismo (RiNEm)*, September 15 – 18, 2014, Padova, Italy.

8. Farina L, Lopresto V, Pinto R, Cavagnaro M (2014). Dielectric and thermal properties of tissues undergoing microwave thermal ablation procedures. *Proceedings of III Convegno Nazionale Interazione tra Campi Elettromagnetici e Biosistemi (ICEmB)*, July 2 – 4, 2014, Napoli, Italy.

9. Farina L, Amabile C, Nissenbaum Y, Cavagnaro M, Lopresto V, Pinto R, Tosoratti N, Cassarino S, Weiss N, Goldberg SN. (2015). Ex vivo tissue shrinking in microwave thermal ablation. *Proceeding of 9th European Conference on Antennas and Propagation (EuCAP)*, April 12 – 17, 2015, Lisbon, Portugal.

10. Farina L, Lopresto V, Pinto R, D'Alessio D, Minosse S, Strigari L, Cavagnaro M. (2015). The use of CT to improve the knowledge of the physical phenomena associated with microwave thermal ablation

procedures. *Proceedings of 2015 International Conference on Electromagnetics in Advanced Applications (ICEAA)*, Sep 7–11, 2015, Torino, Italy.

11. Farina L, Amabile C, Lopresto V, Pinto R, Cavagnaro M, Cassarino S, Tosoratti N, Goldberg SN. (2016). An ex vivo study on the shrinkage occurring in bovine liver during microwave thermal ablation: Carbonized vs coagulated tissue. *Proceedings of Annual Meeting of BEMS and EBEA (BioEM),* June 5 – 10, 2016, Ghent, Belgium.

12. Farina L, Lopresto V, Pinto R, D'Alessio D, Minosse S, Strigari L, Cavagnaro M. (2016). CT study of the tissue shrinkage occurring during a microwave thermal ablation procedure. *Proceedings of V Gruppo Nazionale di Bioingegneria (Italian National Bioengineering Group – GNB)*, June 20 – 22, 2016 Napoli, Italy.

13. Farina L & Cavagnaro M. (2016). Tissue shrinkage in microwave thermal ablation. *Proceedings of XXI Riunione Nazionale di Elettromagnetismo (RiNEm)*, September 12 – 14, 2016, Parma, Italy.

14. Lopresto V, Pinto R, D'Alessio D, Minosse S, Strigari L, Farina L, Cavagnaro M. (2015). CT-based characterization of ex vivo liver tissue undergoing microwave thermal ablation. *Proceeding of 30th Annual Meeting of the European Society for Hyperthermic Oncology (ESHO)*, June 24 – 27, 2015, Zurich, Switzerland.

15. Lopresto V, Pinto R, Farina L, Cavagnaro M. (2016). Microwave thermal ablation: effects of tissue properties variations in predictive models for treatment planning. *Advances in Magnetics Conference (AIM)*, March 14 – 16, 2016, Bormio, Italy.

16. Minosse S, D'Alessio D, Lopresto V, Pinto R, Farina L, Cavagnaro M, Strigari L. (2016) CT-based monitoring of microwave thermal ablation. *Proceeding of the 9° National Congress of the Italian Association of Medical Physics (AIFM)*, February 25 – 28, 2016, Perugia, Italy.

17. Vannucci L, Rajsiglová I, Stakeheev D, Ceci P, Falvo E, Babic M, Kostiv U, Caja F, Krizan J, Vrba J, Vrba J Jr, Vrba D, Farina L, Lopresto V, Ruvio G. (2016). Nanoconstructs for targeting the tumor microenvironment. *Proceedings of the 21st World Congress on Advances in Oncology (WCAO)*, Oct 6-8, 2016, Athens, Greece.

Other topics

18. Pittella E, Nardecchia M, Farina L. (2016). Design of Microelectromagnets for Magnetic Particles Manipulation. IEEE Trans on Magnetics 52(11):4003106. DOI: 10.1109/TMAG.2016.2586026.